

NuSTAR Observations of 52 Compton-thick Active Galactic Nuclei Selected by the Swift/BAT All-sky Hard X-Ray Survey

ATSUSHI TANIMOTO ¹, YOSHIHIRO UEDA ², HIROKAZU ODAKA ^{1,3,4}, SATOSHI YAMADA ² AND CLAUDIO RICCI ^{5,6}

¹*Department of Physics, The University of Tokyo, Tokyo 113-0033, Japan*

²*Department of Astronomy, Kyoto University, Kyoto 606-8502, Japan*

³*Research Center for the Early Universe, The University of Tokyo, Tokyo 113-0033, Japan*

⁴*Kavli IPMU (WPI), UTIAS, The University of Tokyo, Chiba 277-8583, Japan*

⁵*Núcleo de Astronomía de la Facultad de Ingeniería, Universidad Diego Portales, Av. Ejército Libertador 441, Santiago, Chile*

⁶*Kavli Institute for Astronomy and Astrophysics, Peking University, Beijing 100871, China*

ABSTRACT

We present the systematic broadband X-ray spectral analysis of 52 Compton-thick ($24 \leq \log N_{\text{H}}^{\text{LOS}}/\text{cm}^{-2}$) active galactic nucleus (CTAGN) candidates selected by the Swift/BAT all-sky hard X-ray survey observed with Chandra, XMM-Newton, Swift/XRT, Suzaku, and NuSTAR. The XMM-Newton data of 10 objects and the NuSTAR data of 15 objects are published for the first time. We use an X-ray spectral model from a clumpy torus (XClumpy) to determine the torus properties. As a result, the hydrogen column density along the line of sight $N_{\text{H}}^{\text{LOS}}$ obtained from the XClumpy model indicate that 24 objects are Compton-thin AGNs and 28 objects are Compton-thick AGNs in the 90% confidence interval. The main reason is the difference in the torus model applied. The hydrogen column density along the equatorial direction $N_{\text{H}}^{\text{Equ}}$ of CTAGNs inferred from the XClumpy model is larger than that of less obscured AGNs. The Compton-thin torus covering factor C_{22} obtained from the XClumpy model is consistent with that of Ricci et al. (2017a) in the low Eddington ratio ($\log R_{\text{Edd}} \leq -1.0$), whereas C_{22} inferred from the XClumpy model is larger than that of Ricci et al. (2017a) in the high Eddington ratio ($-1.0 \leq \log R_{\text{Edd}}$). The average value of the Compton-thick torus covering factor C_{24} obtained from the XClumpy model is $36^{+4}_{-4}\%$. This value is larger than that of Ricci et al. (2015) ($C_{24} \simeq 27^{+4}_{-4}\%$) based on the assumption that all AGNs have intrinsically the same torus structure. These results suggest that the structure of CTAGN may be intrinsically different from that of less obscured AGN.

Keywords: Active galactic nuclei (16), Astrophysical black holes (98), High energy astrophysics (739), Seyfert galaxies (1447), Supermassive black holes (1663), X-ray active galactic nuclei (2035)

1. INTRODUCTION

Elucidating the nature of Compton-thick ($24 \leq \log N_{\text{H}}^{\text{LOS}}/\text{cm}^{-2}$) active galactic nuclei (CTAGN) is essential for understanding the coevolution between supermassive black holes (SMBH) and their host galaxies (e.g., Kormendy & Ho 2013). CTAGNs are also important to explain the origin of the cosmic X-ray background (e.g., Ueda et al. 1998, 1999, 2003; Gilli et al. 2007; Ueda et al. 2014; Harrison et al. 2016; Ananna et al. 2019, 2020). Recent studies suggested that CTAGNs appear to be at the stage of intense star formation and rapid mass accretion due to major mergers (e.g., Hopkins et al. 2006; Ricci et al. 2017b, 2021; Yamada et al. 2021). Hence CTAGNs may be at a different evolutionary stage compared to less obscured AGNs, rather than simply having a higher hydrogen column density along the line of sight. However, it is still unclear whether CTAGNs are intrinsically different from other objects. The reason is that it is difficult to observe CTAGNs due to their heavy obscuration.

Hard X-ray observations above 10 keV are one of the best ways to detect CTAGNs due to their high penetration power against obscuration. Recently, the Neil Gehrels Swift Observatory (Gehrels et al. 2004) has performed an all-sky hard X-ray survey and produced local AGN catalogs (e.g., Markwardt et al. 2005; Tueller et al. 2008, 2010; Baumgartner et al. 2013; Oh et al. 2018). Using the Swift/Burst Alert Telescope (BAT) 70-month catalog (Baumgartner et al. 2013), Ricci et al. (2017c) systematically

analyzed broadband X-ray spectra of 838 AGNs mainly observed with Swift/X-Ray Telescope (XRT) and Swift/BAT. As a result, Ricci et al. (2015) identified 55 CTAGN candidates. To accurately determine the properties of CTAGNs, however, more sensitive hard X-ray observation data are required.

The Nuclear Spectroscopic Telescope Array (NuSTAR; Harrison et al. 2013) is the first orbiting telescopes to focus hard X-rays. The NuSTAR consists of two co-aligned grazing incidence telescopes with two Focal Plane Modules (FPM: 3–79 keV). It provides a combination of sensitivity, spatial resolution, and spectral resolution factors of 10 to 100 improved over previous X-ray satellites in the hard X-ray band (Harrison et al. 2013). Recently, NuSTAR observed a lot of local CTAGNs (e.g., Arévalo et al. 2014; Baloković et al. 2014; Puccetti et al. 2014; Bauer et al. 2015; Rivers et al. 2015; Guainazzi et al. 2016; Koss et al. 2016; Puccetti et al. 2016; Oda et al. 2017; Baloković et al. 2018; Marchesi et al. 2019b,a; Zhao et al. 2019a,b, 2020).

To estimate the properties of CTAGNs, we have to assume an X-ray spectral model from an AGN torus. The X-ray spectrum of the AGN mainly consists of three components. (1) The direct power-law component from the center due to inverse Compton scattering by a hot corona. (2) The reflection component from the accretion disk and the torus. (3) The fluorescence Fe $K\alpha$ line at 6.4 keV from the accretion disk and the torus. Especially in the case of CTAGNs, the modeling of the AGN torus is important. This is because the direct component is strongly absorbed by the torus and the reflection component is dominant (e.g., Tanimoto et al. 2018).

Many studies indicated that the AGN torus consists of dusty clumps (clumpy torus: Krolik & Begelman 1988; Laor & Draine 1993; Hönig et al. 2006; Hönig & Beckert 2007; Nenkova et al. 2008a,b). Nevertheless, few X-ray spectral models from the clumpy torus have been constructed. Extending the earlier works (Liu & Li 2014; Furui et al. 2016), Tanimoto et al. (2019) generated a new X-ray spectral model from the clumpy torus (XClumpy) utilizing the Monte Carlo simulation for astrophysics and cosmology (MONACO: Odaka et al. 2011, 2016). In the XClumpy model, we assumed the power-law distribution of clumps in the radial direction and the Gaussian distribution in the elevation direction¹. This XClumpy model has been used to analyze the X-ray spectra of AGNs (e.g., Miyaji et al. 2019; Ogawa et al. 2019; Tanimoto et al. 2019, 2020; Toba et al. 2020; Yamada et al. 2020; Ogawa et al. 2021; Uematsu et al. 2021; Yamada et al. 2021). Recently, Buchner et al. (2019) also constructed an X-ray spectral model from the clumpy torus called UXCLUMPY.

This paper presents the results of applications of the XClumpy model to the broadband X-ray spectra of 52 CTAGN candidates detected by the Swift/BAT and observed with Chandra, XMM–Newton, Swift/XRT, Suzaku, and NuSTAR. The structure of this paper is the following. Section 2 describes the sample selection. In Section 3, we present the data analysis. Section 4 describes the X-ray spectral analysis with the XClumpy model. In Section 5, we examine the fraction of CTAGN and validate the radiation-regulated AGN unification model. We assume the solar abundances by Anders & Grevesse (1989). To estimate the luminosity, we adopt the cosmological parameters ($H_0 = 70.0 \text{ km s}^{-1} \text{ Mpc}^{-1}$, $\Omega_m = 0.30$, $\Omega_\lambda = 0.70$).

2. SAMPLE SELECTION

We select 52 CTAGN candidates observed with Chandra, XMM–Newton, Swift, Suzaku, and NuSTAR from the sample of Ricci et al. (2015). Table 1 shows the information of the 52 CTAGN candidates in our sample. Here we exclude three objects (NGC 1068, Circinus Galaxy, and NGC 6921). The reasons are the following:

1. **NGC 1068.** There is a lot of contamination from the host galaxy and it is difficult to determine the parameters of the torus (Bauer et al. 2015).
2. **Circinus Galaxy.** Tanimoto et al. (2019) have already analyzed the broadband X-ray spectra of the Circinus Galaxy with the XClumpy model.
3. **NGC 6921.** Yamada et al. (2021) have already analyzed the broadband X-ray spectra of the NGC 6921 with the XClumpy model.

To determine the torus parameters, we need to analyze both soft X-ray data (Chandra, XMM–Newton, Swift/XRT, and Suzaku) and hard X-ray data (Swift/BAT and NuSTAR). Table 2 summarizes details of the observations. In this study, we select the soft X-ray data in the following order of priority:

1. Simultaneous observational data with the XMM–Newton and NuSTAR.
2. Non-simultaneous observational data with the XMM–Newton or Suzaku and NuSTAR. Here we select the one with the longest observation time among the XMM–Newton and Suzaku data.

¹ The inner radius is 0.05 pc, the outer radius is 1.00 pc, and the radius of each clump is 0.002 pc. The absolute values of these three parameters are freely selected and only their ratios are important. This is because a self-similar geometry produces identical results.

3. Non-simultaneous observational data with the Chandra and NuSTAR.
4. Simultaneous observation data with the Swift/XRT and NuSTAR.

Here we prioritize non-simultaneous observations with Chandra, XMM–Newton, Suzaku and NuSTAR over simultaneous observations with the Swift/XRT and NuSTAR. In the case of CTAGN candidates, the X-ray flux in 2–10 keV is very small due to their strong absorption. To determine the hydrogen column density along the line of sight ($\log N_{\text{H}}^{\text{LOS}}/\text{cm}^{-2}$), we have to observe the X-ray spectral shape in 2–10 keV. Especially, XMM–Newton and Suzaku have an effective area about 10 times larger than Swift/XRT in 2–10 keV, and can determine $\log N_{\text{H}}^{\text{LOS}}/\text{cm}^{-2}$. In fact, we confirmed that the results did not change if we included the Swift/XRT data.

Table 1. Summary of Objects

Swift Name (1)	Counterpart (2)	RA (3)	Dec (4)	Redshift (5)	$N_{\text{H}}^{\text{Gal}}$ (6)	$\log M_{\text{BH}}/M_{\odot}$ (7)	Reference (8)
SWIFT J0030.0–5904	ESO 112–G006	00h30m43.83s	–59d00m25.9s	0.02885	0.01360
SWIFT J0105.5–4213	MCG –07–03–007	01h05m26.82s	–42d12m58.3s	0.02988	0.02660	8.56	(02)
SWIFT J0111.4–3808	NGC 0424	01h11m27.63s	–38d05m00.5s	0.01176	0.01630	7.78	(01)
SWIFT J0122.8+5003	MCG +08–03–018	01h22m34.43s	+50d03m18.0s	0.02040	0.21800	8.41	(02)
SWIFT J0128.9–6039	2MASX J01290761–6038423	01h29m07.63s	–60d38m42.1s	0.20300	0.02880
SWIFT J0130.0–4218	ESO 244–IG030	01h29m51.23s	–42d19m35.3s	0.02560	0.01820	7.39	(02)
SWIFT J0250.7+4142	NGC 1106	02h50m40.51s	+41d40m17.4s	0.01447	0.11800
SWIFT J0251.3+5441	2MFGC 02280	02h50m42.59s	+54d42m17.6s	0.01515	0.55000
SWIFT J0251.6–1639	NGC 1125	02h51m40.27s	–16d39m03.7s	0.01093	0.02850	7.34	(02)
SWIFT J0304.1–0108	NGC 1194	03h03m49.11s	–01d06m13.5s	0.01360	0.07970	8.12	(02)
SWIFT J0308.2–2258	NGC 1229	03h08m10.79s	–22d57m38.9s	0.03629	0.01830
SWIFT J0350.1–5019	ESO 201–IG004	03h50m22.96s	–50d18m09.4s	0.03591	0.01200
SWIFT J0357.5–6255	2MASX J03561995–6251391	03h56m19.97s	–62d51m38.7s	0.10756	0.03510
SWIFT J0427.6–1201	MCG –02–12–017	04h27m01.41s	–12d03m34.3s	0.03246	0.04100
SWIFT J0453.4+0404	CGCG 420–015	04h53m25.75s	+04d03m41.7s	0.02939	0.08360	8.31	(02)
SWIFT J0601.9–8636	ESO 005–G004	06h05m41.63s	–86d37m54.7s	0.00623	0.15300
SWIFT J0615.8+7101	Mrk 0003	06h15m36.36s	+71d02m15.1s	0.01351	0.15500	8.81	(03)
SWIFT J0656.4–4921	2MASX J06561197–4919499	06h56m11.96s	–49d19m50.0s	0.04100	0.04940	8.61	(02)
SWIFT J0714.2+3518	MCG +06–16–028	07h14m03.86s	+35d16m45.4s	0.01569	0.06700	7.34	(02)
SWIFT J0743.0+6513	Mrk 0078	07h42m41.73s	+65d10m37.5s	0.03715	0.03880	7.92	(03)
SWIFT J0807.9+3859	Mrk 0622	08h07m41.04s	+39d00m15.2s	0.02323	0.05940	7.51	(02)
SWIFT J0902.7–6816	NGC 2788A	09h02m39.44s	–68d13m36.6s	0.01335	0.06310	8.71	(02)
SWIFT J0919.2+5528	SBS 0915+556	09h19m13.19s	+55d27m55.0s	0.04940	0.03190	7.72	(02)
SWIFT J0924.2–3141	2MASX J09235371–3141305	09h23m53.73s	–31d41m30.7s	0.04237	0.19600
SWIFT J0934.7–2156	ESO 565–G019	09h34m43.56s	–21d55m40.1s	0.01629	0.04960
SWIFT J0935.9+6120	MCG +10–14–025	09h35m51.60s	+61d21m11.5s	0.03937	0.03330	8.35	(02)

Table 1 continued on next page

Table 1 (continued)

Swift Name	Counterpart	RA	Dec	Redshift	$N_{\text{H}}^{\text{Gal}}$	$\log M_{\text{BH}}/M_{\odot}$	Reference
(1)	(2)	(3)	(4)	(5)	(6)	(7)	(8)
SWIFT J1001.7+5543	NGC 3079	10h01m57.80s	+55d40m47.2s	0.00372	0.00906	8.27	(02)
SWIFT J1031.5–4205	ESO 317–G041	10h31m23.12s	–42d03m38.2s	0.01932	0.12500
SWIFT J1033.8+5257	SDSS J103315.71+525217.8	10h33m15.72s	+52d52m17.9s	0.14036	0.01370
SWIFT J1048.4–2511	NGC 3393	10h48m23.46s	–25d09m43.4s	0.01251	0.07950	7.52	(02)
SWIFT J1206.2+5243	NGC 4102	12h06m22.99s	+52d42m39.9s	0.00282	0.01780	8.75	(02)
SWIFT J1212.9+0702	NGC 4180	12h13m03.05s	+07d02m20.2s	0.00699	0.01460
SWIFT J1253.5–4137	ESO 323–G032	12h53m20.32s	–41d38m08.3s	0.01600	0.12000	7.56	(02)
SWIFT J1305.4–4928	NGC 4945	13h05m27.48s	–49d28m05.6s	0.00188	0.21700	6.14	(04)
SWIFT J1416.9–4640	IGR J14175–4641	14h17m03.66s	–46d41m41.2s	0.07661	0.11900	8.80	(02)
SWIFT J1432.8–4412	NGC 5643	14h32m40.74s	–44d10m27.9s	0.00400	0.12400	7.05	(04)
SWIFT J1442.5–1715	NGC 5728	14h42m23.90s	–17d15m11.1s	0.00935	0.10000	8.07	(02)
SWIFT J1445.6+2702	CGCG 164–019	14h45m36.84s	+27d02m05.2s	0.02990	0.02700	7.11	(02)
SWIFT J1635.0–5804	ESO 137–G034	16h35m14.11s	–58d04m48.1s	0.00914	0.36000
SWIFT J1643.2+7036	NGC 6232	16h43m20.24s	+70d37m57.1s	0.01480	0.06450	7.43	(02)
SWIFT J1652.0–5915	ESO 138–G001	16h51m20.13s	–59d14m05.2s	0.00914	0.19900
SWIFT J1652.9+0223	NGC 6240	16h52m58.87s	+02d24m03.3s	0.02448	0.06260	9.20	(02)
SWIFT J1800.3+6637	NGC 6552	18h00m07.23s	+66d36m54.3s	0.02649	0.04540
SWIFT J2015.2+2526	2MASX J20145928+2523010	20h14m59.27s	+25d23m01.0s	0.04530	0.47600
SWIFT J2102.6–2810	ESO 464–G016	21h02m23.76s	–28d10m29.5s	0.03635	0.10000
SWIFT J2148.3–3454	NGC 7130	21h48m19.52s	–34d57m04.5s	0.01615	0.02110	7.61	(02)
SWIFT J2207.3+1013	NGC 7212	22h07m01.98s	+10d14m00.3s	0.02667	0.06330	7.47	(02)
SWIFT J2242.4–3711	ESO 406–G004	22h42m33.49s	–37d11m07.9s	0.02897	0.01070
SWIFT J2304.9+1220	NGC 7479	23h04m56.65s	+12d19m22.4s	0.00794	0.07700	7.53	(02)
SWIFT J2307.9+2245	SWIFT J2307.9+2245	23h07m48.87s	+22d42m37.0s	0.03473	0.10900
SWIFT J2318.4–4223	NGC 7582	23h18m23.50s	–42d22m14.0s	0.00525	0.01390	7.74	(02)
SWIFT J2328.9+0328	NGC 7682	23h29m03.93s	+03d32m00.0s	0.01714	0.06250	7.56	(04)

NOTE—Column (1): Swift name. Column (2): counterpart name based on the BAT AGN Spectroscopic Survey (BASS: <https://www.bass-survey.com/>). Column (3)–(4): position taken from NASA/IPAC Extragalactic Database (NED: <https://ned.ipac.caltech.edu/>). Column (5): redshift taken from NED. Column (6): total Galactic HI and H₂ weighted values in units of 10²² cm^{–2} (<https://www.swift.ac.uk/analysis/nhtot/index.php>; Willingale et al. 2013). Column (7) black hole mass. Column (8): reference of the black hole mass.

References—(01) Bian & Gu (2007). (02) Koss et al. (2017). (03) Merloni et al. (2003). (04) van den Bosch (2016).

Table 2. Summary of Observations

Galaxy Name (1)	Observatory (2)	Observation ID (3)	Exposure (4)	Start Date (5)	End Date (6)	Binning (7)	Reference (8)
ESO 112-G006	XMM-Newton	0852180101	21	2019 Dec 06	2019 Dec 06	50	(21)
	NuSTAR	60561038002	56	2019 Dec 06	2019 Dec 07	50	(21)
MCG -07-03-007	XMM-Newton	0852180201	21	2019 Dec 28	2019 Dec 28	50	(21)
	NuSTAR	60561039002	54	2019 Dec 27	2019 Dec 29	50	(21)
NGC 0424	XMM-Newton	0550950101	99	2008 Dec 07	2008 Dec 09	50	(01)
	NuSTAR	60061007002	15	2013 Jan 26	2013 Jan 26	50	(01)
MCG +08-03-018	Swift	00080019001	7	2014 Jan 27	2014 Jan 27	10	(12)
	NuSTAR	60061010002	31	2014 Jan 27	2014 Jan 28	50	(12)
2MASX J01290761-6038423	XMM-Newton	0802450101	22	2017 Oct 31	2017 Nov 01	20	This work
	NuSTAR	60201035002	25	2016 Dec 03	2016 Dec 04	50	This work
ESO 244-IG030	XMM-Newton	0830500101	14	2018 May 23	2018 May 23	50	(11)
	NuSTAR	60468001002	28	2018 May 23	2018 May 23	50	(11)
NGC 1106	XMM-Newton	0821870301	14	2019 Mar 02	2019 Mar 02	50	This work
	NuSTAR	60469002002	19	2019 Feb 22	2019 Feb 23	50	This work
2MFGC 02280	Swift	00080255001	7	2013 Feb 16	2013 Feb 16	10	(10)
	NuSTAR	60061030002	16	2013 Feb 16	2013 Feb 16	50	(10)
NGC 1125	Chandra	21418	53	2018 Oct 24	2018 Oct 25	50	This work
	NuSTAR	60510001002	30	2019 Jun 10	2019 Jun 11	50	This work
NGC 1194	Suzaku	704046010	51	2009 Aug 01	2009 Aug 02	50	(19)
	NuSTAR	60061035002	30	2015 Feb 28	2015 Mar 01	50	(12)
NGC 1229	Swift	00080534001	6	2013 Jul 05	2013 Jul 05	10	(12)
	NuSTAR	60061325002	25	2013 Jul 05	2013 Jul 05	50	(12)
ESO 201-IG004	Suzaku	701017020	19	2006 Nov 23	2006 Nov 23	20	This work
	NuSTAR	60061331002	23	2014 Aug 09	2014 Aug 09	50	(12)
2MASX J03561995-6251391	XMM-Newton	0802450201	14	2017 Nov 20	2017 Nov 20	50	This work
	NuSTAR	60201034002	24	2016 May 06	2016 May 07	50	(12)

Table 2 continued on next page

Table 2 (*continued*)

Galaxy Name (1)	Observatory (2)	Observation ID (3)	Exposure (4)	Start Date (5)	End Date (6)	Binning (7)	Reference (8)
MCG -02-12-017	XMM-Newton	0762920601	20	2016 Mar 01	2016 Mar 01	50	This work
	NuSTAR	60101015002	19	2016 Mar 03	2016 Mar 03	50	This work
CGCG 420-015	Suzaku	704058010	109	2009 Sep 01	2009 Sep 04	50	(19)
	NuSTAR	60001158002	95	2014 Nov 10	2014 Nov 12	100	(12)
ESO 005-G004	Suzaku	701018010	20	2006 Apr 13	2006 Apr 14	50	(22)
	NuSTAR	60061063002	24	2015 Nov 10	2015 Nov 10	50	(12)
Mrk 0003	XMM-Newton	0741050401	6	2015 Apr 20	2015 Apr 20	50	(07)
	NuSTAR	60002049010	27	2015 Apr 20	2015 Apr 21	50	(07)
2MASX J06561197-4919499	XMM-Newton	0852180401	21	2020 Feb 23	2020 Feb 24	50	This work
	NuSTAR	60561041002	55	2020 Feb 23	2020 Feb 24	50	This work
MCG +06-16-028	Suzaku	709007010	79	2015 Apr 04	2015 Apr 06	50	(18)
	NuSTAR	60061072002	23	2013 Dec 03	2013 Dec 03	50	(12)
Mrk 0078	XMM-Newton	0307001501	4	2006 Mar 11	2006 Mar 11	20	(23)
	NuSTAR	60061336002	24	2018 Nov 19	2018 Nov 19	50	(23)
Mrk 0622	XMM-Newton	0852180501	6	2019 Sep 28	2019 Sep 29	50	(21)
	NuSTAR	60561042002	54	2019 Sep 28	2019 Sep 29	50	(21)
NGC 2788A	Suzaku	710007010	42	2015 May 15	2015 May 16	20	(18)
	NuSTAR	60469001002	24	2019 Jun 14	2019 Jun 15	20	This work
SBS 0915+556	Swift	00081867001	2	2017 Feb 16	2017 Feb 16	20	This work
	NuSTAR	60201036002	29	2017 Feb 16	2017 Feb 17	50	This work
2MASX J09235371-3141305	Swift	00080674001	7	2014 Apr 19	2014 Apr 19	10	(12)
	NuSTAR	60061339002	21	2014 Apr 19	2014 Apr 20	20	(12)
ESO 565-G019	XMM-Newton	0852180601	22	2019 Dec 18	2019 Dec 18	50	This work
	NuSTAR	60561043002	50	2019 Dec 17	2019 Dec 18	50	This work
MCG +10-14-025	Suzaku	701002010	49	2006 Mar 31	2006 Apr 01	20	(14)
	NuSTAR	60001068002	17	2014 Mar 21	2014 Mar 22	50	(14)

Table 2 *continued on next page*

Table 2 (*continued*)

Galaxy Name (1)	Observatory (2)	Observation ID (3)	Exposure (4)	Start Date (5)	End Date (6)	Binning (7)	Reference (8)
NGC 3079	Suzaku	803039020	102	2008 May 26	2008 May 29	50	(09)
	NuSTAR	60061097002	22	2013 Nov 12	2013 Nov 12	50	(12)
ESO 317–G041	XMM–Newton	0830500201	22	2018 May 27	2018 May 28	50	(11)
	NuSTAR	60468002002	31	2018 May 27	2018 May 28	50	(11)
SDSS J103315.71+525217.8	XMM–Newton	0830500301	24	2018 Jun 02	2018 Jun 03	50	(11)
	NuSTAR	60468003002	29	2018 Jun 02	2018 Jun 03	50	(11)
NGC 3393	Suzaku	702004010	55	2007 May 23	2007 May 25	50	(19)
	NuSTAR	60061205002	16	2013 Jan 28	2013 Jan 28	50	(10)
NGC 4102	Suzaku	704057010	106	2009 May 30	2009 Jun 01	50	(08)
	NuSTAR	60160472002	18	2015 Nov 19	2015 Nov 19	50	(12)
NGC 4180	Chandra	09438	2	2008 Nov 16	2008 Nov 16	10	This work
	NuSTAR	60201038002	29	2016 Jul 14	2016 Jul 15	50	This work
ESO 323–G032	XMM–Newton	0852181201	23	2020 Feb 12	2020 Feb 12	50	(21)
	NuSTAR	60561045004	50	2020 Feb 12	2020 Feb 13	50	(21)
NGC 4945	Suzaku	100008030	95	2006 Jan 15	2006 Jan 17	50	(19)
	NuSTAR	60002051004	54	2013 Jun 15	2013 Jun 16	100	(12)
IGR J14175–4641	XMM–Newton	0802450401	9	2018 Feb 09	2018 Feb 09	50	This work
	NuSTAR	60201033002	21	2016 May 25	2016 May 25	50	(12)
NGC 5643	XMM–Newton	0744050101	94	2014 Aug 27	2014 Aug 28	50	(05)
	NuSTAR	60061362002	22	2014 May 24	2014 May 25	50	(12)
NGC 5728	Suzaku	701079010	41	2006 Jul 19	2006 Jul 20	50	(20)
	NuSTAR	60061256002	24	2013 Jan 02	2013 Jan 02	50	(12)
CGCG 164–019	Swift	00080536003	6	2020 Mar 14	2020 Mar 14	20	This work
	NuSTAR	60061327004	36	2020 Mar 12	2020 Mar 12	20	This work
ESO 137–G034	Suzaku	403075010	92	2008 Oct 05	2008 Oct 07	50	(19)
	NuSTAR	60061272002	17	2016 Jun 07	2016 Jun 08	50	(04)

Table 2 *continued on next page*

Table 2 (*continued*)

Galaxy Name (1)	Observatory (2)	Observation ID (3)	Exposure (4)	Start Date (5)	End Date (6)	Binning (7)	Reference (8)
NGC 6232	Swift	00080537002	5	2013 Aug 18	2013 Aug 18	20	(12)
	NuSTAR	60061328002	18	2013 Aug 17	2013 Aug 18	20	(12)
ESO 138–G001	XMM–Newton	0690580101	123	2013 Feb 24	2013 Feb 25	50	(16)
	NuSTAR	60201040002	44	2016 May 22	2016 May 23	50	This work
NGC 6240	XMM–Newton	0147420201	10	2003 Mar 14	2003 Mar 15	50	(13)
	NuSTAR	60002040002	31	2014 Mar 30	2014 Mar 31	50	(12)
NGC 6552	XMM–Newton	0852180901	11	2019 Aug 20	2019 Aug 20	50	(21)
	NuSTAR	60561046002	48	2019 Aug 20	2019 Aug 21	50	(21)
2MASX J20145928+2523010	XMM–Newton	0802450501	30	2017 Nov 18	2017 Nov 19	50	This work
	NuSTAR	60201032002	23	2017 May 27	2017 May 28	50	This work
ESO 464–G016	XMM–Newton	0762920401	14	2016 Apr 11	2016 Apr 11	50	This work
	NuSTAR	60101013002	22	2016 Apr 13	2016 Apr 14	50	(12)
NGC 7130	Suzaku	703012010	44	2008 May 11	2008 May 12	20	(19)
	NuSTAR	60261006002	40	2016 Dec 15	2016 Dec 16	50	(12)
NGC 7212	XMM–Newton	0200430201	14	2004 May 20	2004 May 20	50	(06)
	NuSTAR	60061310002	24	2013 Sep 01	2013 Sep 02	50	(12)
ESO 406–G004	Swift	00081420001	3	2020 Jun 26	2020 Jun 26	10	This work
	NuSTAR	60161799002	24	2020 Jun 26	2020 Jun 26	20	This work
NGC 7479	XMM–Newton	0824450601	65	2018 May 30	2018 May 31	50	(12)
	NuSTAR	60201037002	17	2016 May 12	2016 May 12	50	(12)
SWIFT J2307.9+2245	XMM–Newton	0852181001	22	2019 Nov 30	2019 Nov 30	50	This work
	NuSTAR	60561047002	56	2019 Nov 29	2019 Nov 30	50	This work
NGC 7582	XMM–Newton	0782720301	76	2016 Apr 28	2016 Apr 29	100	(15)
	NuSTAR	60201003002	47	2016 Apr 28	2016 Apr 29	100	(02)
NGC 7682	XMM–Newton	0301150501	13	2005 May 27	2005 May 27	50	(17)
	NuSTAR	60368002002	22	2017 Oct 06	2017 Oct 06	50	This work

NOTE—Column (1): galaxy name. Column (2): satellite name (Chandra, XMM–Newton, Swift, Suzaku, and NuSTAR). Column (3): observation identification number. Column (4): exposure time (based on Chandra/ACIS, XMM–Newton/PN, Swift/XRT, Suzaku/XIS0, and NuSTAR/FPMA) in units of ks. Column (5): start date in units of ymd. Column (6): end date in units of ymd. Column (7): binning. Column (8): reference of the previous work.

References—(01) Baloković et al. (2014). (02) Baloković et al. (2018). (03) Bauer et al. (2015). (04) Georgantopoulos & Akylas (2019). (05) Guainazzi et al. (2004). (06) Guainazzi et al. (2005) (07) Guainazzi et al. (2016). (08) Kawamuro et al. (2016). (09) Konami et al. (2012). (10) Koss et al. (2016). (11) Marchesi et al. (2019a). (12) Marchesi et al. (2019b). (13) Netzer et al. (2005). (14) Oda et al. (2017). (15) Piconcelli et al. (2007). (16) Piconcelli et al. (2011). (17) Ricci et al. (2017c). (18) Tanimoto et al. (2016). (19) Tanimoto et al. (2018). (20) Tanimoto et al. (2020). (21) Torres-Albà et al. (2021). (22) Ueda et al. (2007). (23) Zhao et al. (2020).

3. DATA ANALYSIS

3.1. *Chandra*

Chandra (1999–: [Weisskopf et al. 2002](#)) is NASA’s X-ray astronomical satellite. It carries two Advanced CCD Imaging Spectrometers (ACIS: [Garmire et al. 2003](#)). We analyzed the ACIS data using the Chandra interactive analysis of observations 4.12.1 and the calibration database 4.9.2.1. We reprocessed the unfiltered ACIS data using `chandra_repro`. The source spectra were extracted from a circular region with a 30 arcsec radius centered on the flux peak and the background spectra were taken from a source-free circular region with the same radius using `specextract`. We generated the redistribution matrix files (RMF) and the ancillary response files (ARF) using `specextract`.

3.2. *XMM–Newton*

XMM–Newton (1999–: [Jansen et al. 2001](#)) is the second ESA’s X-ray astronomical satellite. It has three European photon imaging cameras: two MOS (MOS1 and MOS2: [Turner et al. 2001](#)) and one PN ([Strüder et al. 2001](#)). We analyzed the MOS and PN data using the science analysis system 18.00 and the current calibration file released on 2020 April 20. We reprocessed the unfiltered MOS and PN data using `emproc` and `epproc`, respectively. The source spectra were extracted from a circular region with a 30 arcsec radius centered on the flux peak and the background spectra were obtained from a source-free circular region with a 30 arcsec radius in the same CCD chip. We generated the RMF and the ARF using `rmfgen` and `arfgen`, respectively. We combined the source spectra, background spectra, RMF, and ARF of MOS1 and MOS2 using `addascaspec`.

3.3. *Swift*

The Neil Gehrels Swift Observatory (2004–: [Gehrels et al. 2004](#)) carries one X-Ray Telescope (XRT: [Burrows et al. 2005](#)) and one Burst Alert Telescope (BAT: [Barthelmy et al. 2005](#)). We analyzed the XRT data using the HEASoft 6.28 and the calibration database released on 2020 July 24. We reprocessed the unfiltered XRT data using `xrtpipeline`. The source spectra were extracted from a circular region with a 30 arcsec radius centered on the flux peak and the background spectra were obtained from a source-free circular region with the same radius using `xrtproducts`. We also utilized the time-averaged spectra obtained from the Swift/BAT 105-month catalog ([Oh et al. 2018](#))².

3.4. *Suzaku*

Suzaku (2005–2015: [Mitsuda et al. 2007](#)) was the fifth Japanese X-ray astronomical satellite. It had four X-ray Imaging Spectrometers (XIS0, XIS1, XIS2, and XIS3: [Koyama et al. 2007](#)). One CCD camera (XIS2) is the back-illuminated XIS (BIXIS: 0.20–12.0 keV) and three CCD cameras (XIS0, XIS1, and XIS3) are the front-illuminated XIS (FIXIS: 0.40–12.0 keV). We analyzed the XIS data using the HEASoft 6.28 and the calibration database released on 2018 October 10. We reprocessed the unfiltered XIS data using `aepipeline`. The source spectra were extracted from a circular region with a 60 arcsec radius centered on the flux peak and the background spectra were taken from a source-free circular region with the same radius. In the case of ESO 005–G004, the fluxes are very low and we need to determine the background more precisely ([Ueda et al. 2007](#)). We extracted the source spectra from a circular region with a 90 arcsec and the background spectra from a source-free circular region with a 180 arcsec for ESO 005–G004. We generated the RMF and the ARF using `xismfgen` and `xissimarfgen` ([Ishisaki et al. 2007](#)), respectively. We combined the source spectra, background spectra, RMF, and ARF of FIXIS using `addascaspec`.

3.5. *NuSTAR*

NuSTAR (2012–: [Harrison et al. 2013](#)) is the NASA’s X-ray astronomical satellite. It carries two co-aligned grazing incidence telescopes coupled with two Focal Plane Modules (FPM: 3–79 keV). We analyzed FPM data using the HEASoft 6.28 and the calibration database released on 2020 August 26. We reprocessed the unfiltered FPM data using `nupipeline`. The source spectra were extracted from a circular region with a 30 arcsec radius centered on the flux peak and the background spectra were obtained from a source-free circular region with a 30 arcsec radius using `nuproducts`. We combined the source spectra, background spectra, RMF, and ARF using `addascaspec`.

² <https://swift.gsfc.nasa.gov/results/bs105mon/>

4. SPECTRAL ANALYSIS

We performed simultaneous fitting to the Chandra/ACIS (0.5–8.0 keV), XMM–Newton/MOS (0.5–8.0 keV), XMM–Newton/PN (0.5–10.0 keV), Swift/XRT (0.5–6.0 keV), Swift/BAT (14.0–100.0 keV), Suzaku/BIXIS (0.5–8.0 keV), Suzaku/FIXIS (2.0–10.0 keV), NuSTAR/FPM (4.0–60.0 keV). Our X-ray spectral model is the following:

$$\begin{aligned} & \text{const1} \times \text{phabs} \\ & \times (\text{const2} \times \text{cabs} \times \text{zphabs} \times \text{zcutoffpl} \\ & + \text{const3} \times \text{zcutoffpl} + \text{atable}\{\text{xclumpy_v01_RC.fits}\} \\ & + \text{atable}\{\text{xclumpy_v01_RL.fits}\} + (\text{zgauss}) + (\text{apecc})). \end{aligned} \quad (1)$$

Our model consists of six components.

1. **const1** \times **phabs**. The **const1** term represents a cross calibration constant to compensate for differences in absolute flux among instruments. We assume that the cross calibration constant of NuSTAR/FPM to Swift/BAT (C_{FPM}) is unity as a reference. To reduce the number of free parameters, we fix other cross calibration constants ($C_{\text{ACIS}} = 1.10$, $C_{\text{MOS}} = 1.00$, $C_{\text{PN}} = 0.90$, $C_{\text{XRT}} = 1.05$, $C_{\text{BIXIS}} = 0.90$, $C_{\text{FIXIS}} = 0.95$) based on the results of Madsen et al. (2017), which presented the cross calibration campaigns among Chandra, XMM–Newton, Swift, Suzaku, and NuSTAR. The **phabs** term represents the Galactic absorption. We utilized the total Galactic HI and H_2 values provided by Willingale et al. (2013).
2. **const2** \times **cabs** \times **zphabs** \times **zcutoffpl**. This component represents the transmitted continuum through the torus. The **const2** term is a constant to consider the time variability among Chandra, XMM–Newton, Swift, Suzaku, and NuSTAR observations. We fix the time variability constant of Swift/BAT at unity as a reference and make the constant of Chandra, XMM–Newton, Swift/XRT, Suzaku ($T_{\text{Satellite1}}$), and NuSTAR ($T_{\text{Satellite2}}$) free parameters. In the case of simultaneous observations of XMM–Newton and NuSTAR or Swift and NuSTAR, we link $T_{\text{Satellite2}}$ to $T_{\text{Satellite1}}$. We limit $T_{\text{Satellite1}}$ and $T_{\text{Satellite2}}$ values within a range of 0.10–10.0 to avoid unrealistic results. If the time variability constant is not determined in the range of 0.10–10.0, we fix its value at 1.00. We multiply this constant to the transmitted component only. This is because the sizes of the scatterer and reflector are most likely parsec or larger scales and we can ignore the time variability of these components. The **zphabs** and **cabs** terms represent the photoelectric absorption and Compton scattering by the torus, respectively. We determine the hydrogen column density along the line of sight ($N_{\text{H}}^{\text{LOS}}$) according to Equation 3. The **zcutoffpl** represents the power-law with an exponential cutoff. Since it is difficult to determine the cutoff energy, we fix this value at a typical one ($E_{\text{cut}} = 370$ keV: Ricci et al. 2018)³. Since almost all of our targets have low Eddington ratios, we fix the cutoff energy of all the sources at 370 keV. We have confirmed that the obtained results are consistent within the 90% confidence interval even when we fix the cutoff energy at 160 keV for the sources with the high Eddington ratios.
3. **const3** \times **zcutoffpl**. This component represents the scattered component. The **const3** term is the scattering factor (f_{scat}). We link the photon index (Γ), the cutoff energy (E_{cut}), and the normalization (N_{Dir}) to those of the transmitted continuum.
4. **atable**{**xclumpy_v01_RC.fits**}. This component represents the reflection continuum from the torus based on the XClumpy model (Tanimoto et al. 2019)⁴. We assumed the power-law distribution in the radial direction and the Gaussian distribution in the elevation direction as the clump distribution. The clump number density function $d(r, \theta, \phi)$ in the spherical coordinate system (where r is radius, θ is inclination angle, and ϕ is azimuth) is the following.

$$d(r, \theta, \phi) \propto \left(\frac{r}{r_{\text{in}}}\right)^{-1/2} \exp\left(-\frac{(\theta - \pi/2)^2}{\sigma^2}\right). \quad (2)$$

Here r_{in} is the inner radius of the torus and σ is the torus angular width. In the XClumpy model, Tanimoto et al. (2019) assumed that the radius of the clump is 0.002 pc, the inner radius of the torus is 0.05 pc, and the outer radius of the torus is 1.00 pc. This model has five free parameters: (1) hydrogen column density along the equatorial plane ($\log N_{\text{H}}^{\text{Equ}}/\text{cm}^{-2}$:

³ Ricci et al. (2018) obtained $E_{\text{cut}} = 370_{-51}^{+51}$ keV for sources with the low Eddington ratios ($\log R_{\text{Edd}} \leq -1.0$), whereas they estimated $E_{\text{cut}} = 160_{-41}^{+41}$ keV for sources with the high Eddington ratios ($-1.0 \leq \log R_{\text{Edd}}$).

⁴ In this study, we updated the XClumpy model using the National Astronomical Observatory of Japan’s XC50 supercomputer. Please see the following link for details (<https://github.com/AtsushiTanimoto/XClumpy>).

23–25), (2) torus angular width (σ : 10° – 90°), (3) inclination angle (i : 20° – 87°), (4) photon index (Γ : 1.0–3.0), and (5) normalization (N_{Dir}). The hydrogen column density along the line of sight ($N_{\text{H}}^{\text{LOS}}$) is determined by the following equation.

$$N_{\text{H}}^{\text{LOS}} = N_{\text{H}}^{\text{Equ}} \exp\left(-\frac{(i - \pi/2)^2}{\sigma^2}\right). \quad (3)$$

We limit i value within a range of 60° – 87° . Especially, we fix its value at 87° for the eight objects (Mrk 0003, NGC 3079, NGC 3393, NGC 4945, NGC 5643, NGC 5728, NGC 6240, and NGC 7479) whose water maser has been detected (Panessa et al. 2020). This is because, if i is free parameter, the obtained torus covering factor is unphysically large, which is inconsistent with the existence of a narrow line region. We link Γ and N_{Dir} to those of the transmitted continuum. We note that we fix $E_{\text{cut}} = 370$ keV in the XClumpy model.

5. **atable{xclumpy_v01_RL.fits} + (zgauss)**. This component represents fluorescent lines from the torus based on the XClumpy model. We link all parameters to those of the reflection continuum. If the F-test shows an improvement at a significance level of 99% or higher, we add zgauss to the model. This is because recent studies implied the contribution from spatially extended fluorescent lines such as Fe $K\alpha$ (6.4 keV) (e.g., Arévalo et al. 2014; Bauer et al. 2015; Fabbiano et al. 2017; Kawamuro et al. 2019, 2020) and the XClumpy model does not include the ionized fluorescent lines such as He-like Fe $K\alpha$ (6.7 keV) and H-like Fe $K\alpha$ (7.0 keV). In fact, it is necessary to add Fe $K\alpha$ fluorescent lines to reproduce the observed X-ray spectra for some objects.
6. **apec**. This component represents emission from an optically thin thermal plasma in the host galaxy. If the F-test shows an improvement at a significance level of 99% or higher, we add apec to the model.

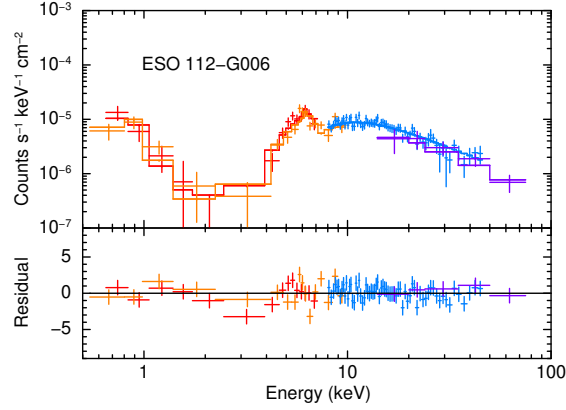


Figure 1. The folded X-ray spectra fitted with the XClumpy model. The pink crosses are Chandra/ACIS, the red crosses are XMM–Newton/MOS, the orange crosses are XMM–Newton/PN, the light green crosses are Swift/XRT, the green crosses are Suzaku/BIXIS, the light blue crosses are Suzaku/FIXIS, the blue crosses are NuSTAR/FPM, and the purple crosses are Swift/BAT. The solid curves represent best fitting model. The lower panel shows residuals. The complete figure set (52 images) is available in the online journal.

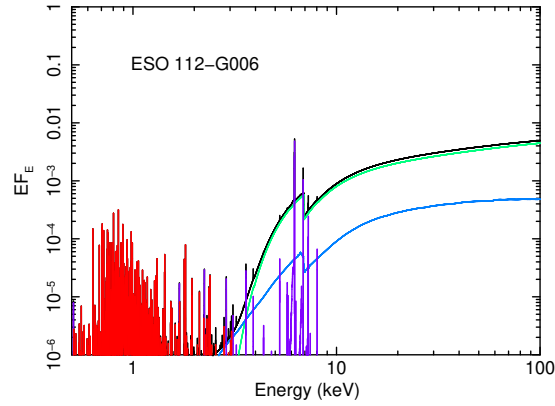


Figure 2. The best fitting model. The black line is total. the red line is thermal emission from optically thin plasma, the orange line is scattered component, the green line is direct component, the blue line is reflection continuum from the torus, and the purple line is emission lines from the torus. The complete figure set (52 images) is available in the online journal.

Fig. Set 52. The Folded X-Ray Spectra Fitted with the XClumpy Model

Fig. Set 52. The Best Fitting Model

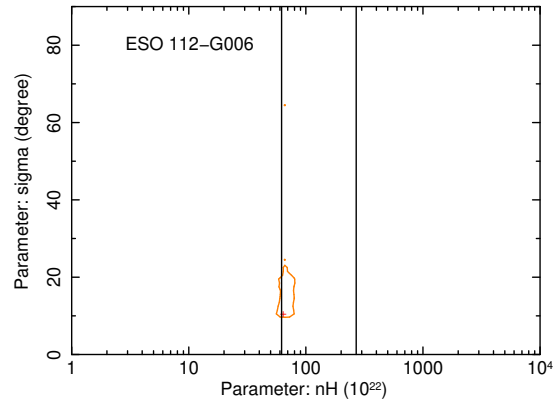


Figure 3. The two-dimensional $\Delta\chi^2$ contour between the hydrogen column density along the line of sight ($N_{\text{H}}^{\text{LOS}}$) and the torus angular width (σ). The orange line is the 90% confidence. The black line represents the 90% confidence interval of $N_{\text{H}}^{\text{LOS}}$ obtained from Ricci et al. (2015). The complete figure set (52 images) is available in the online journal.

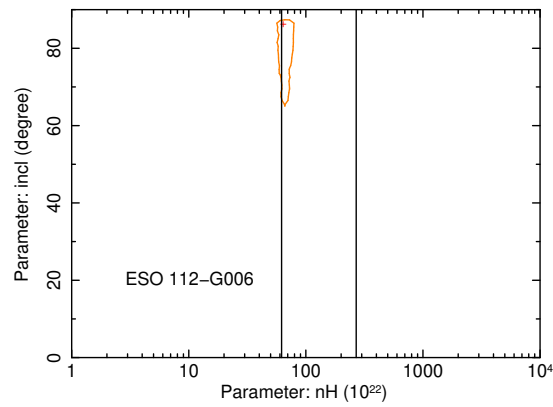


Figure 4. The two-dimensional $\Delta\chi^2$ contour between the hydrogen column density along the line of sight ($N_{\text{H}}^{\text{LOS}}$) and the inclination angle (i). The orange line is the 90% confidence. The black line represents the 90% confidence interval of $N_{\text{H}}^{\text{LOS}}$ obtained from Ricci et al. (2015). The complete figure set (44 images) is available in the online journal.

Fig. Set 52. The two-dimensional $\Delta\chi^2$ contour between the hydrogen column density along the line of sight and the torus angular width

Fig. Set 44. The two-dimensional $\Delta\chi^2$ contour between the hydrogen column density along the line of sight and the inclination angle

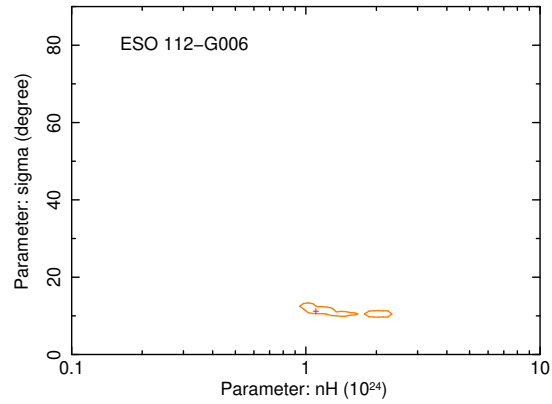


Figure 5. The two-dimensional $\Delta\chi^2$ contour between the hydrogen column density along the equatorial direction ($N_{\text{H}}^{\text{Equ}}$) and the torus angular width (σ). The orange line is the 90% confidence. The complete figure set (52 images) is available in the online journal.

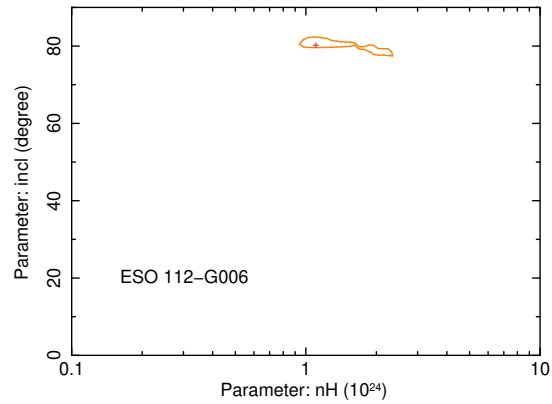


Figure 6. The two-dimensional $\Delta\chi^2$ contour between the hydrogen column density along the equatorial direction ($N_{\text{H}}^{\text{Equ}}$) and the inclination angle (i). The orange line is the 90% confidence. The complete figure set (44 images) is available in the online journal.

Fig. Set 52. The two-dimensional $\Delta\chi^2$ contour between the hydrogen column density along the equatorial direction and the torus angular width

Fig. Set 44. The two-dimensional $\Delta\chi^2$ contour between the hydrogen column density along the equatorial direction and the inclination angle

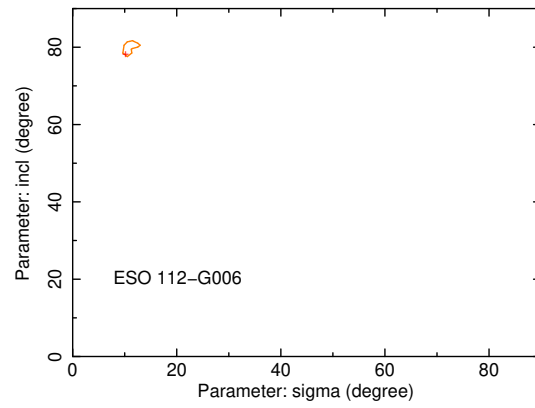


Figure 7. The two-dimensional $\Delta\chi^2$ contour between the torus angular width (σ) and the inclination angle (i). The orange line is the 90% confidence. The complete figure set (44 images) is available in the online journal.

Fig. Set 44. The two-dimensional $\Delta\chi^2$ contour between the torus angular width and the inclination angle.

Table 3. Best Fitting Parameters

Galaxy Name	$T_{\text{Satellite1}}$	$T_{\text{Satellite2}}$	Γ	N_{Dir}	f_{scat}	$N_{\text{H}}^{\text{LOS}}$	$N_{\text{H}}^{\text{Equ}}$
(01)	(02)	(03)	(04)	(05)	(06)	(07)	(08)
	σ	i	E_{line}	N_{line}	$k_{\text{B}}T$	$N_{k_{\text{B}}T}$	χ_{red}^2
	(09)	(10)	(11)	(12)	(13)	(14)	(15)
ESO 112-G006	$1.25^{+0.63}_{-0.15}$	1.25 (linked)	$1.47^{+0.17}_{-0.07}$	$0.07^{+0.02}_{-0.02}$	$0.00^{+0.08}$	$0.62^{+0.06}_{-0.04}$	$1.55^{+1.76}_{-0.60}$
	$10.1^{+9.53}$	$80.4^{+1.47}_{-6.01}$	$0.82^{+0.03}_{-0.09}$	$0.03^{+0.01}_{-0.01}$	1.21
MCG -07-03-007	$0.84^{+0.43}_{-0.10}$	0.84 (linked)	$1.61^{+0.05}_{-0.20}$	$0.13^{+0.01}_{-0.08}$	$0.45^{+0.54}_{-0.08}$	$0.90^{+0.11}_{-0.09}$	$1.49_{-0.69}$
	$38.9^{+46.2}_{-3.68}$	$62.3^{+24.1}$	$0.86^{+0.10}_{-0.19}$	$0.03^{+0.00}_{-0.01}$	1.24
NGC 0424	$0.50^{+0.29}_{-0.18}$	$0.44^{+0.13}_{-0.12}$	$1.70^{+0.07}_{-0.12}$	$0.25^{+0.05}_{-0.07}$	$3.10^{+0.83}_{-0.31}$	$0.84^{+0.31}_{-0.07}$	$1.54^{+0.23}_{-0.57}$
	$38.4^{+15.9}_{-7.00}$	$60.0^{+17.3}$	$6.47^{+0.03}_{-0.02}$	$0.04^{+0.01}_{-0.01}$	1.40
MCG +08-03-018	$0.55^{+0.34}_{-0.09}$	0.55 (linked)	$2.15^{+0.08}_{-0.21}$	$0.71^{+0.17}_{-0.36}$	$1.65^{+1.43}_{-0.52}$	$0.54^{+0.13}_{-0.10}$	$5.56^{+2.23}_{-3.94}$
	$18.4^{+6.07}_{-5.58}$	$61.9^{+7.91}$	1.04
2MASX J0129761-6038423	$0.44^{+0.29}_{-0.07}$	$0.53^{+0.43}_{-0.03}$	$1.86^{+0.22}_{-0.10}$	$0.37^{+0.26}_{-0.16}$	$0.10^{+0.03}_{-0.04}$	$0.95^{+0.09}_{-0.17}$	$1.28^{+0.38}_{-0.29}$
	$10.1^{+12.1}$	$84.4_{-5.10}$	$0.82^{+0.19}_{-0.30}$	$0.03^{+0.01}_{-0.01}$	1.14
ESO 244-IG030	$0.22^{+0.10}_{-0.07}$	0.22 (linked)	$1.74^{+0.17}_{-0.15}$	$0.09^{+0.08}_{-0.04}$	$1.54^{+0.63}_{-0.72}$	$0.06^{+0.01}_{-0.01}$	$0.13^{+0.01}$
	$10.0^{+1.11}$	$81.4^{+3.10}_{-0.84}$	$0.30^{+0.39}_{-0.17}$	$0.06^{+0.09}_{-0.03}$	0.94
NGC 1106	$3.27^{+1.07}_{-1.77}$	3.27 (linked)	$1.67^{+0.16}_{-0.30}$	$0.43^{+0.17}_{-0.35}$	$0.58^{+2.16}_{-0.10}$	$3.77^{+0.52}_{-0.32}$	$8.17^{+1.63}_{-1.51}$
	$17.1^{+14.3}_{-3.15}$	$74.9^{+1.85}_{-14.7}$	$6.67^{+0.05}_{-0.27}$	$0.04^{+0.03}_{-0.02}$	1.15
2MFGC 02280	$0.10^{+0.69}$	0.10 (linked)	$1.71^{+0.18}_{-0.39}$	$0.27^{+0.53}_{-0.21}$	$0.36^{+1.46}_{-0.29}$	$2.03^{+2.17}_{-0.20}$	$2.47^{+4.22}_{-0.78}$
	$66.6^{+20.2}_{-45.8}$	$60.4^{+24.8}$	0.96
NGC 1125	$0.54^{+0.03}_{-0.37}$	$0.43^{+0.05}_{-0.11}$	$1.82^{+0.11}_{-0.24}$	$0.32^{+0.19}_{-0.16}$	$0.54^{+0.42}_{-0.20}$	$1.16^{+0.92}_{-0.50}$	$5.71^{+3.00}_{-3.49}$
	$23.8^{+12.5}_{-7.87}$	$60.0^{+9.30}$	$0.83^{+0.35}_{-0.06}$	$0.07^{+0.01}_{-0.03}$	1.16
NGC 1194	$2.09^{+1.03}_{-0.37}$	$0.99^{+0.21}_{-0.07}$	$1.27^{+0.07}_{-0.07}$	$0.08^{+0.02}_{-0.01}$	$4.15^{+0.44}_{-0.93}$	$0.83^{+0.06}_{-0.13}$	$1.73^{+0.34}_{-0.59}$
	$34.8^{+1.62}_{-15.9}$	$60.2^{+20.8}$	$6.43^{+0.03}_{-0.03}$	$0.06^{+0.03}_{-0.01}$	1.20
NGC 1229	$0.99^{+1.09}_{-0.28}$	0.99 (linked)	$1.54^{+0.18}_{-0.45}$	$0.07^{+0.10}_{-0.06}$	$1.22^{+7.23}_{-0.89}$	$0.47^{+0.26}_{-0.09}$	$9.17_{-8.57}$
	$17.3^{+3.78}_{-1.44}$	$60.2^{+20.5}$	1.23
ESO 201-IG004	$0.84^{+0.45}_{-0.22}$	$0.43^{+0.19}_{-0.10}$	$1.33^{+0.07}_{-0.18}$	$0.04^{+0.01}_{-0.02}$	$7.26^{+1.46}_{-1.31}$	$0.25^{+0.31}_{-0.05}$	$5.61^{+3.94}_{-3.53}$
	$17.0^{+1.87}$	$60.0^{+10.3}$	1.31
2MASX J03561995-6251391	$1.00^{+0.49}_{-0.25}$	$1.69^{+0.78}_{-0.27}$	$1.50^{+0.03}_{-0.10}$	$0.10^{+0.02}_{-0.05}$	$1.08^{+0.80}_{-0.26}$	$0.63^{+0.08}_{-0.12}$	$1.26^{+0.71}_{-0.61}$
	$13.7^{+2.90}$	$78.7^{+6.67}_{-1.00}$	$0.92^{+0.09}_{-0.05}$	$0.06^{+0.03}_{-0.02}$	1.12

Table 3 continued on next page

Table 3 (continued)

Galaxy Name	$T_{\text{Satellite1}}$	$T_{\text{Satellite2}}$	Γ	N_{Dir}	f_{scat}	$N_{\text{H}}^{\text{LOS}}$	$N_{\text{H}}^{\text{Equ}}$
(01)	(02)	(03)	(04)	(05)	(06)	(07)	(08)
	σ	i	E_{line}	N_{line}	$k_{\text{B}}T$	$N_{k_{\text{B}}T}$	χ_{red}^2
	(09)	(10)	(11)	(12)	(13)	(14)	(15)
MCG -02-12-017	$0.68^{+0.40}_{-0.12}$ $15.6^{+1.34}$	0.68 (linked) $60.0^{+14.4}$	$1.79^{+0.09}_{-0.26}$...	$0.09^{+0.01}_{-0.05}$...	$0.17^{+0.20}_{-0.09}$...	$0.24^{+0.04}_{-0.03}$...	$9.59_{-8.43}$ 1.07
CGCG 420-015	$1.26^{+0.36}_{-0.21}$ $22.4^{+1.53}_{-3.15}$	$1.05^{+0.20}_{-0.15}$ $60.1^{+22.3}$	$1.87^{+0.07}_{-0.12}$...	$0.65^{+0.20}_{-0.17}$...	$0.83^{+0.19}_{-0.21}$ $0.85^{+0.08}_{-0.06}$	$0.81^{+0.06}_{-0.04}$ $0.45^{+0.07}_{-0.06}$	$4.83^{+2.48}_{-3.84}$ 1.22
ESO 005-G004	$0.88^{+0.45}_{-0.25}$ $21.1^{+3.11}_{-5.34}$	$0.22^{+0.15}_{-0.05}$ $60.2^{+6.58}$	$1.43^{+0.11}_{-0.08}$ $6.40^{+0.01}_{-0.02}$	$0.09^{+0.03}_{-0.03}$ $0.16^{+0.04}_{-0.02}$	$1.93^{+1.16}_{-0.59}$...	$0.51^{+0.04}_{-0.08}$...	$3.67^{+1.50}_{-1.97}$ 1.25
Mrk 0003	$1.58^{+0.11}_{-0.06}$ $49.8^{+37.4}_{-12.6}$	1.58 (linked) 87.0 (fixed)	$1.60^{+0.04}_{-0.04}$...	$1.03^{+0.19}_{-0.20}$...	$3.31^{+0.94}_{-0.49}$...	$0.84^{+0.02}_{-0.06}$...	$0.85^{+0.04}_{-0.05}$ 1.18
2MASX J06561197-4919499	$1.06^{+0.20}_{-0.28}$ $32.3^{+4.68}_{-13.5}$	1.06 (linked) $60.0^{+24.9}$	$1.58^{+0.04}_{-0.22}$...	$0.07^{+0.03}_{-0.03}$...	$1.17^{+0.66}_{-0.36}$ $0.71^{+0.11}_{-0.11}$	$0.97^{+0.17}_{-0.17}$ $0.05^{+0.02}_{-0.01}$	$2.31^{+0.57}_{-1.32}$ 1.06
MCG +06-16-028	$0.78^{+0.13}_{-0.15}$ $20.1^{+0.97}_{-1.90}$	$0.54^{+0.11}_{-0.11}$ $60.0^{+5.56}$	$1.69^{+0.07}_{-0.11}$...	$0.21^{+0.04}_{-0.05}$...	$0.74^{+0.31}_{-0.24}$ $0.79^{+0.07}_{-0.12}$	$0.69^{+0.19}_{-0.04}$ $0.22^{+0.05}_{-0.05}$	$6.34^{+1.99}_{-2.98}$ 1.30
Mrk 0078	$1.15^{+0.75}_{-0.51}$ $90.0_{-21.7}$	$2.76^{+0.31}_{-0.70}$ $60.5^{+24.2}$	$1.54^{+0.10}_{-0.05}$...	$0.06^{+0.03}_{-0.02}$...	$2.79^{+0.60}_{-1.10}$ $0.63^{+0.12}_{-0.23}$	$0.63^{+0.11}_{-0.04}$ $0.17^{+0.05}_{-0.03}$	$0.70^{+0.09}_{-0.08}$ 0.97
Mrk 0622	$0.40^{+0.09}_{-0.17}$ $16.0^{+3.75}_{-4.43}$	0.40 (linked) $60.2^{+9.44}$	$1.79^{+0.11}_{-0.11}$...	$0.13^{+0.06}_{-0.02}$...	$0.85^{+0.05}_{-0.38}$ $0.59^{+0.13}_{-0.05}$	$0.30^{+0.07}_{-0.02}$ $0.13^{+0.02}_{-0.03}$	$9.42_{-7.64}$ 0.84
NGC 2788A	$1.55^{+1.07}_{-1.17}$ $28.6^{+17.4}_{-9.14}$	$1.32^{+0.54}_{-0.47}$ $85.4_{-22.8}$	$1.67^{+0.11}_{-0.08}$...	$0.37^{+0.03}_{-0.13}$...	$0.17^{+0.10}_{-0.06}$...	$2.31^{+0.52}_{-0.76}$...	$2.37^{+2.20}_{-0.19}$ 1.03
SBS 0915+556	$0.50^{+0.52}$ $12.4^{+70.9}$	0.50 (linked) $85.0_{-24.7}$	$2.02^{+0.02}_{-0.02}$...	$0.29^{+0.20}_{-0.15}$...	$0.00^{+0.10}$...	$0.09^{+0.03}_{-0.02}$...	$0.10^{+0.66}$ 1.33
2MASX J09235371-3141305	$3.02^{+0.91}_{-0.79}$ $22.3^{+3.33}_{-11.3}$	3.02 (linked) $60.0^{+15.5}$	$1.47^{+0.20}_{-0.12}$...	$0.06^{+0.06}_{-0.02}$...	$2.78^{+6.33}_{-2.64}$...	$0.54^{+0.22}_{-0.04}$...	$3.30^{+4.27}_{-1.62}$ 1.05
ESO 565-G019	$0.87^{+0.20}_{-0.09}$ $64.3_{-42.9}$	0.87 (linked) $64.8_{-4.00}$	$1.09^{+0.03}_{-0.08}$ $6.41^{+0.02}_{-0.03}$	$0.01^{+0.01}_{-0.01}$ $0.12^{+0.01}_{-0.02}$	$17.3^{+7.68}_{-7.09}$...	$1.12^{+0.20}_{-0.05}$...	$1.31^{+0.11}_{-0.17}$ 1.20
MCG +10-14-025	$0.91^{+1.21}_{-0.62}$ $13.8^{+73.6}$	$1.36^{+2.84}$ $85.2_{-24.2}$	$1.58^{+0.27}_{-0.32}$...	$0.13^{+0.01}_{-0.10}$...	$1.24^{+4.33}$...	$1.53^{+0.53}_{-0.09}$...	$1.72^{+0.51}_{-0.66}$ 1.07

Table 3 continued on next page

Table 3 (continued)

Galaxy Name	$T_{\text{Satellite1}}$	$T_{\text{Satellite2}}$	Γ	N_{Dir}	f_{scat}	$N_{\text{H}}^{\text{LOS}}$	$N_{\text{H}}^{\text{Equ}}$
(01)	(02)	(03)	(04)	(05)	(06)	(07)	(08)
	σ	i	E_{line}	N_{line}	$k_{\text{B}}T$	$N_{k_{\text{B}}T}$	χ_{red}^2
	(09)	(10)	(11)	(12)	(13)	(14)	(15)
NGC 3079	$0.80^{+6.06}_{-0.55}$	$2.24^{+0.89}_{-0.45}$	$1.61^{+0.12}_{-0.10}$	$0.33^{+0.21}_{-0.11}$	$2.42^{+0.71}_{-0.66}$	$2.65^{+0.40}_{-0.13}$	$2.65^{+0.45}_{-0.17}$
	88.6 _{-24.7}	87.0 (fixed)	1.16
ESO 317-G041	$1.10^{+0.53}_{-0.23}$	1.10 (linked)	$1.40^{+0.26}_{-0.12}$	$0.06^{+0.05}_{-0.02}$	$1.17^{+0.30}_{-0.36}$	$0.85^{+0.16}_{-0.12}$	$2.05^{+1.38}_{-0.99}$
	$19.3^{+25.4}_{-5.84}$	$71.9^{+8.60}_{-10.8}$	1.32
SDSS J103315.71+525217.8	$0.56^{+0.71}_{-0.14}$	0.56 (linked)	$1.55^{+0.25}_{-0.18}$	$0.09^{+0.15}_{-0.07}$	$0.71^{+1.74}_{-0.44}$	$0.71^{+0.18}_{-0.15}$	$2.05^{+7.07}_{-0.75}$
	12.2 ^{+13.7}	$77.5^{+1.20}_{-15.8}$	1.15
NGC 3393	$1.32^{+0.66}_{-0.13}$	$3.76^{+2.40}_{-0.66}$	$1.76^{+0.18}_{-0.18}$	$0.31^{+0.25}_{-0.14}$	$1.14^{+0.57}_{-0.47}$	$2.05^{+0.30}_{-0.21}$	$2.05^{+0.43}_{-0.22}$
	90.0 _{-32.7}	87.0 (fixed)	$0.75^{+0.08}_{-0.08}$	$0.66^{+0.11}_{-0.09}$	1.14
NGC 4102	$0.10^{+0.06}$	$1.74^{+0.06}_{-0.07}$	$1.56^{+0.01}_{-0.07}$	$0.16^{+0.01}_{-0.02}$	$0.00^{+1.09}$	$0.67^{+0.02}_{-0.14}$	10.0 _{-2.85}
	$18.2^{+2.35}_{-4.83}$	$60.0^{+9.33}$	$2.27^{+0.02}_{-0.52}$	$2.46^{+0.21}_{-0.65}$	1.12
NGC 4180	$8.29^{+1.41}_{-7.87}$	$1.79^{+1.71}_{-0.64}$	$1.61^{+0.05}_{-0.17}$	$0.11^{+0.01}_{-0.06}$	$0.71^{+2.07}_{-0.35}$	$1.84^{+1.91}_{-1.16}$	4.10 _{-2.18}
	$33.4^{+24.4}_{-4.16}$	$60.1^{+25.9}$	0.80
ESO 323-G032	$0.11^{+0.01}$	0.11 (linked)	$1.89^{+0.12}_{-0.27}$	$0.42^{+0.20}_{-0.35}$	$0.42^{+1.79}$	$1.27^{+0.17}_{-0.45}$	$2.13^{+0.05}_{-1.36}$
	12.9 ^{+76.0}	$80.7^{+5.05}$	$0.25^{+0.01}_{-0.01}$	$0.16^{+0.05}_{-0.04}$	0.77
NGC 4945	$0.24^{+4.70}_{-0.01}$	$6.91^{+0.58}_{-0.31}$	$1.61^{+0.03}_{-0.02}$	$2.71^{+0.34}_{-0.19}$	$1.65^{+0.11}_{-0.13}$	$3.40^{+0.11}_{-0.08}$	$3.41^{+0.12}_{-0.08}$
	$58.0^{+4.42}_{-1.71}$	87.0 (fixed)	$6.66^{+0.02}_{-0.02}$	$0.09^{+0.01}_{-0.01}$	1.21
IGR J14175-4641	$1.61^{+0.88}_{-0.31}$	$0.53^{+0.21}_{-0.11}$	$1.51^{+0.11}_{-0.14}$	$0.17^{+0.06}_{-0.09}$	$0.36^{+0.40}_{-0.15}$	$0.77^{+0.08}_{-0.13}$	$0.98^{+0.61}_{-0.19}$
	$23.4^{+23.1}_{-6.00}$	$78.6^{+6.12}_{-17.0}$	1.22
NGC 5643	$1.27^{+0.57}_{-0.37}$	$1.28^{+0.33}_{-0.26}$	$1.25^{+0.06}_{-0.07}$	$0.02^{+0.01}_{-0.01}$	$14.7^{+2.52}_{-3.21}$	$0.63^{+0.05}_{-0.10}$	$0.63^{+0.10}_{-0.10}$
	$64.4^{+20.6}_{-30.1}$	87.0 (fixed)	$6.40^{+0.01}_{-0.01}$	$0.13^{+0.01}_{-0.01}$	1.35
NGC 5728	$0.65^{+0.37}_{-0.22}$	$1.27^{+0.16}_{-0.10}$	$1.55^{+0.07}_{-0.05}$	$0.60^{+0.17}_{-0.13}$	$0.69^{+0.18}_{-0.17}$	$1.36^{+0.08}_{-0.11}$	$1.37^{+0.12}_{-0.10}$
	$61.7^{+25.2}_{-15.5}$	87.0 (fixed)	$0.50^{+0.18}_{-0.18}$	$0.45^{+0.22}_{-0.14}$	0.99
CGCG 164-019	$0.34^{+0.20}_{-0.16}$	0.34 (linked)	$1.87^{+0.23}_{-0.23}$	$0.18^{+0.28}_{-0.08}$	$0.93^{+0.64}_{-0.63}$	$0.69^{+0.55}_{-0.06}$	$6.59^{+2.60}_{-4.70}$
	$20.0^{+5.11}_{-6.68}$	$60.0^{+15.4}$	1.29
ESO 137-G034	$8.14^{+0.57}_{-2.44}$	$2.83^{+0.63}_{-0.49}$	$1.85^{+0.09}_{-0.11}$	$0.88^{+0.17}_{-0.31}$	$0.64^{+0.30}_{-0.15}$	$2.87^{+0.20}_{-0.20}$	$2.95^{+0.45}_{-0.20}$
	$29.3^{+10.7}_{-6.70}$	85.2 _{-12.2}	$0.63^{+0.09}_{-0.03}$	$0.92^{+0.07}_{-0.11}$	1.13

Table 3 continued on next page

Table 3 (continued)

Galaxy Name	$T_{\text{Satellite1}}$	$T_{\text{Satellite2}}$	Γ	N_{Dir}	f_{scat}	$N_{\text{H}}^{\text{LOS}}$	$N_{\text{H}}^{\text{Equ}}$
(01)	(02)	(03)	(04)	(05)	(06)	(07)	(08)
	σ	i	E_{line}	N_{line}	$k_{\text{B}}T$	$N_{k_{\text{B}}T}$	χ_{red}^2
	(09)	(10)	(11)	(12)	(13)	(14)	(15)
NGC 6232	$0.14^{+1.33}_{-0.03}$	0.14 (linked)	$1.31^{+0.57}_{-0.14}$	$0.04^{+0.15}_{-0.02}$	$4.86^{+0.08}_{-2.48}$	$1.10^{+1.43}_{-0.59}$	$1.89^{+6.70}_{-0.98}$
	$12.5^{+31.4}$	$80.8_{-18.7}$	1.13
ESO 138-G001	$2.21^{+0.70}_{-0.20}$	$1.90^{+0.73}_{-0.21}$	$1.45^{+0.06}_{-0.03}$	$0.07^{+0.01}_{-0.01}$	$20.2^{+4.47}_{-2.16}$	$0.45^{+0.05}_{-0.03}$	$5.34^{+1.53}_{-3.66}$
	$10.2^{+2.73}$	$73.9^{+2.40}_{-1.61}$	$6.55^{+0.01}_{-0.01}$	$0.26^{+0.01}_{-0.03}$	1.39
NGC 6240	$0.52^{+0.33}_{-0.38}$	$1.16^{+0.14}_{-0.07}$	$1.71^{+0.06}_{-0.09}$	$1.48^{+0.40}_{-0.55}$	$1.49^{+0.65}_{-0.27}$	$1.45^{+0.15}_{-0.05}$	$1.55^{+0.10}_{-0.15}$
	$11.1^{+7.87}$	87.0 (fixed)	$6.73^{+0.04}_{-0.13}$	$0.12^{+0.05}_{-0.04}$	1.07
NGC 6552	$0.24^{+0.09}_{-0.07}$	0.24 (linked)	$2.25^{+0.07}_{-0.10}$	$1.28^{+0.37}_{-0.35}$	$0.08^{+0.06}_{-0.04}$	$0.96^{+0.55}_{-0.05}$	$4.52^{+3.06}_{-1.67}$
	$24.0^{+2.94}_{-4.30}$	$60.1^{+5.70}$	$0.78^{+0.12}_{-0.08}$	$0.11^{+0.02}_{-0.03}$	1.29
2MASX J20145928+2523010	$1.02^{+0.36}_{-0.14}$	$1.08^{+0.35}_{-0.17}$	$1.42^{+0.03}_{-0.09}$	$0.04^{+0.01}_{-0.01}$	$4.79^{+0.75}_{-2.02}$	$0.02^{+0.01}_{-0.01}$	$1.01^{+0.89}_{-0.67}$
	$14.8^{+1.14}$	$60.2^{+7.72}$	1.18
ESO 464-G016	$0.76^{+0.47}_{-0.23}$	0.76 (linked)	$1.54^{+0.13}_{-0.15}$	$0.11^{+0.03}_{-0.04}$	$0.22^{+0.24}_{-0.12}$	$0.82^{+0.19}_{-0.10}$	$0.99^{+0.50}_{-0.16}$
	$51.6^{+33.0}_{-16.8}$	$67.1^{+10.0}$	$0.61^{+0.18}_{-0.25}$	$0.06^{+0.03}_{-0.01}$	0.97
NGC 7130	$4.18^{+5.09}_{-2.34}$	$0.10^{+0.24}$	$1.59^{+0.09}_{-0.24}$	$0.15^{+0.13}_{-0.09}$	$0.00^{+0.03}$	$2.32^{+1.95}_{-0.24}$	$4.06^{+0.69}_{-1.99}$
	$35.9^{+50.8}_{-11.2}$	$63.2^{+23.2}$	1.03
NGC 7212	$1.19^{+0.13}_{-0.51}$	$0.67^{+0.08}_{-0.24}$	$2.12^{+0.02}_{-0.29}$	$0.73_{-0.44}$	$1.01^{+0.98}$	$1.27^{+0.54}_{-0.69}$	$2.43_{-1.21}$
	$27.2^{+44.0}$	$68.1^{+7.70}$	1.38
ESO 406-G004	$0.10^{+0.28}$	0.10 (linked)	$1.10^{+0.28}$	$0.01^{+0.01}_{-0.00}$	$1.18^{+3.96}_{-1.10}$	$0.52^{+5.82}_{-0.14}$	$0.64^{+0.55}_{-0.23}$
	$58.7^{+25.9}_{-35.2}$	$63.2^{+22.5}$	1.33
NGC 7479	$10.0_{-4.56}$	$9.37^{+0.44}_{-6.60}$	$1.85^{+0.12}_{-0.16}$	$1.88^{+0.35}_{-0.65}$	$0.02^{+0.03}_{-0.01}$	$6.07^{+3.61}_{-0.80}$	$6.30^{+3.15}_{-0.93}$
	$15.3^{+13.5}_{-3.25}$	87.0 (fixed)	1.21
SWIFT J2307.9+2245	$0.18^{+0.25}$	0.18 (linked)	$1.86^{+0.03}_{-0.35}$	$0.29^{+0.06}_{-0.22}$	$0.16^{+0.71}_{-0.01}$	$1.62^{+1.26}_{-0.74}$	$4.19_{-2.93}$
	$30.6^{+53.4}_{-4.57}$	$60.1^{+25.5}$	0.98
NGC 7582	$1.73^{+0.20}_{-0.06}$	1.73 (linked)	$1.44^{+0.04}_{-0.01}$	$0.31^{+0.01}_{-0.02}$	$2.66^{+0.60}_{-0.42}$	$0.32^{+0.01}_{-0.02}$	$0.48^{+0.99}_{-0.11}$
	$29.9^{+0.45}_{-11.2}$	$70.8^{+10.6}$	$6.44^{+0.01}_{-0.03}$	$0.10^{+0.01}_{-0.04}$	1.33
NGC 7682	$0.10^{+0.08}$	$0.13^{+0.13}_{-0.01}$	$1.27^{+0.25}_{-0.07}$	$0.03^{+0.04}_{-0.01}$	$3.34^{+0.92}_{-1.87}$	$0.25^{+0.20}_{-0.02}$	$0.56^{+0.35}_{-0.21}$
	$33.5^{+4.65}_{-14.1}$	$60.1^{+25.5}$	$0.23^{+0.14}_{-0.05}$	$0.12^{+0.05}_{-0.05}$	0.98

NOTE—Column (01): galaxy name. Column (02): time variability constant of the soft X-ray observations (Chandra, XMM–Newton, Swift/XRT, and Suzaku) relative to the Swift/BAT observation. Column (03): time variability constant of the hard X-ray observations (NuSTAR) relative to the Swift/BAT observation. Column (04): photon index. Column (05): normalization of the direct component in units of 10^{-2} photons $\text{keV}^{-1} \text{cm}^{-2} \text{s}^{-1}$. Column (06): scattering fraction in units of percent. Column (07): hydrogen column density along the line of sight in units of 10^{24}cm^{-2} . Column (08): hydrogen column density along the equatorial direction in units of 10^{24}cm^{-2} . Column (09): torus angular width in units of degree. Column (10): inclination angle in units of degree. Column (11): energy of the zgauss model in units of keV. Column (12): normalization of the zgauss in units of. Column (13): temperature of the apec model in units of keV. Column (14): normalization of the apec model in units of $10^{-19}/4\pi[D_{\text{A}}(1+z)]^2 \int n_e n_{\text{H}} dV$, where D_{A} is the angular diameter distance to the source in units of cm, n_e and n_{H} are the electron and hydrogen densities in units of cm^{-3} . Column (15): reduced χ^2 . Note that the error on a spectral parameter corresponds to the 90% confidence interval. We estimated the error by using the Markov Chain Monte Carlo chain with a length of 100,000.

Table 4. Fluxes, Luminosities and Covering Factors

Galaxy Name (1)	$\log F_{2-10}$ (2)	$\log F_{10-50}$ (3)	$\log L_{2-10}$ (4)	$\log L_{10-50}$ (5)	C_{22} (6)	C_{24} (7)	EW (8)	$\log R_{\text{Edd}}$ (9)
ESO 112-G006	-12.3	-11.2	42.9	43.2	$0.39^{+0.35}_{-0.39}$	$0.00^{+0.01}$	0.07	...
MCG -07-03-007	-12.3	-11.2	43.1	43.3	$1.00_{-0.01}$	$0.42^{+0.58}_{-0.23}$	0.65	-2.26
NGC 0424	-12.0	-11.1	42.5	42.7	$1.00_{-0.02}$	$0.43^{+0.18}_{-0.19}$	0.62	-2.08
MCG +08-03-018	-11.9	-11.2	43.2	43.0	$0.72^{+0.19}_{-0.17}$	$0.41^{+0.13}_{-0.14}$	0.24	-2.01
2MASX J01290761-6038423	-12.5	-11.5	45.0	45.0	$0.38^{+0.43}_{-0.38}$	$0.09^{+0.12}_{-0.09}$	0.26	...
ESO 244-IG030	-12.3	-11.9	42.7	42.7	$0.28^{+0.03}_{-0.28}$	$0.00^{+0.01}$	0.01	-1.49
NGC 1106	-12.5	-11.1	42.9	43.1	$0.70^{+0.30}_{-0.10}$	$0.42^{+0.33}_{-0.07}$	1.86	...
2MFGC 02280	-12.6	-11.2	42.7	42.9	$1.00_{-0.01}$	$0.89^{+0.11}_{-0.35}$	0.51	...
NGC 1125	-12.3	-11.2	42.4	42.5	$0.87^{+0.13}_{-0.18}$	$0.52^{+0.26}_{-0.18}$	0.66	-1.74
NGC 1194	-11.9	-10.8	42.4	42.9	$0.98_{-0.12}$	$0.43^{+0.08}_{-0.22}$	0.37	-2.54
NGC 1229	-12.1	-11.2	43.0	43.3	$0.71^{+0.12}_{-0.06}$	$0.43^{+0.09}_{-0.09}$	0.33	-1.77
ESO 201-IG004	-12.1	-11.3	43.0	43.4	$0.68^{+0.07}_{-0.68}$	$0.38^{+0.08}_{-0.38}$	0.40	...
2MASX J03561995-6251391	-12.2	-11.0	43.0	43.3	$0.50^{+0.10}_{-0.50}$	$0.11^{+0.14}_{-0.11}$	0.09	...
MCG -02-12-017	-12.2	-11.5	43.0	43.1	$0.65^{+0.35}_{-0.65}$	$0.40^{+0.60}_{-0.40}$	0.06	...
CGCG 420-015	-11.7	-10.7	43.6	43.7	$0.83^{+0.04}_{-0.08}$	$0.47^{+0.08}_{-0.13}$	0.26	-1.51
ESO 005-G004	-12.0	-11.2	41.7	42.0	$0.78^{+0.08}_{-0.14}$	$0.41^{+0.08}_{-0.13}$	1.07	...
Mrk 0003	-11.1	-10.1	43.3	43.5	$1.00_{-0.01}$	$0.00^{+0.01}$	0.29	-2.31
2MASX J06561197-4919499	-12.5	-11.3	43.1	43.4	$0.97^{+0.03}_{-0.14}$	$0.49^{+0.09}_{-0.24}$	0.42	-2.31
MCG +06-16-028	-12.1	-11.1	42.7	42.8	$0.78^{+0.03}_{-0.06}$	$0.46^{+0.04}_{-0.07}$	0.28	-1.44
Mrk 0078	-12.3	-11.0	43.0	43.3	$1.00_{-0.01}$	$0.00^{+0.01}$	0.29	-1.72
Mrk 0622	-12.3	-11.5	42.7	42.8	$0.67^{+0.33}_{-0.15}$	$0.41^{+0.34}_{-0.13}$	0.18	-1.61
NGC 2788A	-12.5	-11.0	42.8	43.0	$0.92^{+0.08}_{-0.15}$	$0.45^{+0.34}_{-0.13}$	0.78	-2.71
SBS 0915+556	-11.7	-11.6	43.6	43.5	$0.32^{+0.68}_{-0.32}$	$0.00^{+0.01}$	0.07	-0.92
2MASX J09235371-3141305	-11.8	-10.8	43.1	43.5	$0.81^{+0.10}_{-0.28}$	$0.41^{+0.22}_{-0.21}$	0.05	...
ESO 565-G019	-12.3	-11.3	42.0	42.6	$1.00_{-0.01}$	$0.55^{+0.45}_{-0.35}$	1.76	...
MCG +10-14-025	-12.7	-11.3	43.3	43.6	$0.52^{+0.48}_{-0.52}$	$0.18^{+0.82}_{-0.18}$	0.33	-1.85

Table 4 continued on next page

Table 4 (continued)

Galaxy Name	$\log F_{2-10}$	$\log F_{10-50}$	$\log L_{2-10}$	$\log L_{10-50}$	C_{22}	C_{24}	EW	$\log R_{\text{Edd}}$
(1)	(2)	(3)	(4)	(5)	(6)	(7)	(8)	(9)
NGC 3079	-12.3	-10.7	41.7	42.0	$1.00_{-0.01}$	$1.00_{-0.02}$	0.59	-3.37
ESO 317-G041	-12.5	-11.2	42.5	42.9	$0.70^{+0.30}_{-0.17}$	$0.28^{+0.38}_{-0.12}$	0.19	...
SDSS J103315.71+525217.8	-12.5	-11.5	44.3	44.6	$0.47^{+0.51}_{-0.47}$	$0.18^{+0.47}_{-0.18}$	0.18	...
NGC 3393	-12.5	-10.8	42.6	42.7	$1.00_{-0.01}$	$0.97^{+0.03}_{-0.12}$	0.97	-1.72
NGC 4102	-12.4	-10.7	40.9	41.2	$0.74^{+0.26}_{-0.15}$	$0.46^{+0.54}_{-0.12}$	0.59	-4.65
NGC 4180	-12.4	-11.2	41.8	42.0	$0.99^{+0.01}_{-0.03}$	$0.64^{+0.36}_{-0.12}$	1.12	...
ESO 323-G032	-12.7	-11.7	42.8	42.9	$0.50^{+0.50}_{-0.50}$	$0.19^{+0.81}_{-0.19}$	0.84	-1.56
NGC 4945	-11.5	-9.80	41.3	41.5	$1.00_{-0.01}$	$0.90^{+0.04}_{-0.02}$	0.74	-1.64
IGR 14175-4641	-11.9	-11.2	44.1	44.4	$0.77^{+0.23}_{-0.14}$	$0.00^{+0.01}$	0.16	-1.50
NGC 5643	-12.1	-11.2	40.8	41.3	$1.00_{-0.01}$	$0.00^{+0.01}$	1.34	-3.05
NGC 5728	-11.8	-10.4	42.8	43.0	$1.00_{-0.01}$	$0.57^{+0.21}_{-0.14}$	0.77	-2.07
CGCG 164-019	-12.5	-11.5	43.0	43.1	$0.78^{+0.14}_{-0.19}$	$0.46^{+0.12}_{-0.16}$	0.58	-0.91
ESO 137-G034	-12.2	-10.8	42.7	42.8	$0.94^{+0.06}_{-0.10}$	$0.51^{+0.17}_{-0.11}$	0.96	...
NGC 6232	-12.6	-11.8	42.2	42.7	$0.48^{+0.52}_{-0.48}$	$0.17^{+0.64}_{-0.17}$	1.02	-2.03
ESO 138-G001	-11.6	-10.9	41.9	42.2	$0.43^{+0.11}_{-0.43}$	$0.23^{+0.06}_{-0.23}$	0.63	...
NGC 6240	-11.8	-10.5	43.9	44.1	$0.42^{+0.28}_{-0.42}$	$0.13^{+0.09}_{-0.13}$	0.38	-2.10
NGC 6552	-12.2	-11.3	43.5	43.3	$0.86^{+0.07}_{-0.10}$	$0.49^{+0.11}_{-0.10}$	0.94	...
2MASX J20145928+2523010	-11.7	-11.2	42.6	43.0	$0.53^{+0.06}_{-0.53}$	$0.03^{+0.01}_{-0.01}$	0.14	...
ESO 464-G016	-12.3	-11.2	43.2	43.5	$1.00_{-0.01}$	$0.00^{+0.01}$	0.45	...
NGC 7130	-12.6	-11.3	42.6	42.9	$1.00_{-0.02}$	$0.68^{+0.32}_{-0.20}$	0.98	-1.81
NGC 7212	-12.2	-11.3	43.4	43.3	$0.90^{+0.10}_{-0.90}$	$0.43^{+0.57}_{-0.43}$	0.62	-0.87
ESO 406-G004	-12.8	-11.8	42.4	43.0	$1.00_{-0.01}$	$0.00^{+0.01}$	0.77	...
NGC 7479	-12.6	-11.0	42.9	43.0	$0.63^{+0.37}_{-0.11}$	$0.35^{+0.30}_{-0.07}$	1.26	-1.43
SWIFT J2307.9+2245	-12.7	-11.4	43.4	43.5	$0.97^{+0.02}_{-0.05}$	$0.60^{+0.40}_{-0.15}$	1.10	...
NGC 7582	-11.1	-10.2	42.1	42.4	$0.86^{+0.14}_{-0.20}$	$0.00^{+0.01}$	0.12	-2.44
NGC 7682	-12.6	-11.7	42.2	42.7	$0.92^{+0.07}_{-0.19}$	$0.00^{+0.01}$	0.66	-2.16

NOTE—Column (1): galaxy name. Column (2): logarithmic observed flux in the 2–10 keV based on Chandra/ACIS, XMM–Newton/PN, Swift/XRT, Suzaku/FIXIS. Column (3): logarithmic observed flux in the 10–50 keV based on NuSTAR/FPM. Column (4): logarithmic intrinsic luminosity in the 2–10 keV. We estimate the X-ray luminosities by using the redshifts except for three very nearby ($D \leq 20$ Mpc) objects (NGC 3079, NGC 4102, and NGC 4945). In the case of these objects, we utilize the following distances: (NGC 3079: 16.5 Mpc, NGC 4102: 9.1 Mpc, and NGC 4945: 3.55 Mpc) (Tully et al. 2009). Column (5): logarithmic intrinsic luminosity in the 10–50 keV. Column (6): Compton-thin torus covering factor. Column (7): Compton-thick torus covering factor. Column (8): equivalent width of the Fe K α line in units of keV. Column (9): logarithmic Eddington ratio ($R_{\text{Edd}} = L_{\text{Bol}}/L_{\text{Edd}}$). Here we obtain the bolometric luminosity as $L_{\text{bol}} = 20L_{2-10}$ and define the Eddington luminosity as $L_{\text{Edd}} = 1.25 \times 10^{38} M_{\text{BH}}/M_{\odot}$.

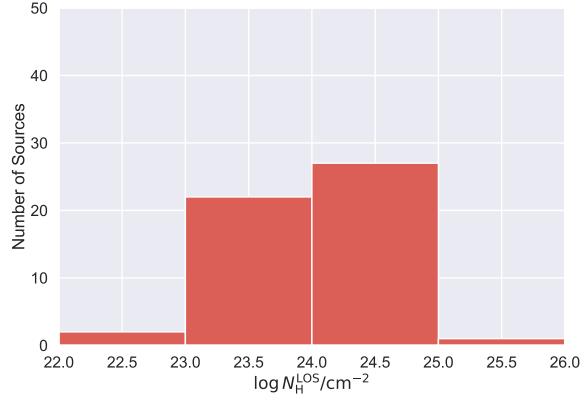


Figure 8. The distribution of the hydrogen column density along the line of sight ($\log N_{\text{H}}^{\text{LOS}}/\text{cm}^{-2}$). Here we plot the 90% confidence upper bound of $\log N_{\text{H}}^{\text{LOS}}/\text{cm}^{-2}$.

5. RESULTS

We applied the XClumpy model to the broadband X-ray spectra of 52 CTAGN candidates observed with Chandra, XMM–Newton, Swift, Suzaku, and NuSTAR. As a result, our model can reproduce the X-ray spectra of all objects. Figure 1 plots the folded X-ray spectra fitted with the XClumpy model and Figure 2 shows the best fitting model. Table 3 summarizes the best fitting parameters. Figure 3–7 plot the two-dimensional $\Delta\chi^2$ contours between the hydrogen column density along the line of sight ($\log N_{\text{H}}^{\text{LOS}}/\text{cm}^{-2}$) and the torus angular width (σ), between $\log N_{\text{H}}^{\text{LOS}}/\text{cm}^{-2}$ and the inclination angle (i), between the hydrogen column density along the equatorial direction ($\log N_{\text{H}}^{\text{Equ}}/\text{cm}^{-2}$) and σ , between $\log N_{\text{H}}^{\text{Equ}}/\text{cm}^{-2}$ and i , and between σ and i , respectively.

6. DISCUSSION

The structure of this Section is the following: Section 6.1 investigates the distribution of the hydrogen column density along the line of sight and estimates the fraction of the Compton-thick AGN. Section 6.2 introduces the torus covering factor and the radiation-regulated AGN unification model. Section 6.3 examines the distributions of best fitting parameters. Section 6.4 validates the radiation-regulated AGN unification model.

6.1. Distribution of Hydrogen Column Density and Compton-thick AGN Fraction

We investigate the fraction of the Compton-thick AGN. Figure 8 shows the distribution of the logarithmic hydrogen column density along the line of sight ($\log N_{\text{H}}^{\text{LOS}}/\text{cm}^{-2}$). Figure 8 indicates that 24 objects are Compton-thin AGNs and 28 objects are Compton-thick AGNs within the 90% confidence interval. Here we classify the object whose 90% confidence upper bound of $\log N_{\text{H}}^{\text{LOS}}/\text{cm}^{-2}$ is larger than 24 as Compton-thick AGN.

To clarify why $\log N_{\text{H}}^{\text{LOS}}/\text{cm}^{-2}$ of this study differ from those of Ricci et al. (2015), Figure 3 plots the two-dimensional $\Delta\chi^2$ contour between $\log N_{\text{H}}^{\text{LOS}}/\text{cm}^{-2}$ and the torus angular width (σ). Figure 3 also plots the 90% confidence interval of $\log N_{\text{H}}^{\text{LOS}}/\text{cm}^{-2}$ of Ricci et al. (2015). Figure 3 shows that $\log N_{\text{H}}^{\text{LOS}}/\text{cm}^{-2}$ of 34 objects obtained from this study are not consistent with those inferred from Ricci et al. (2015). The first reason is the difference in the torus model. In the torus model, we use the XClumpy model (Tanimoto et al. 2019), while Ricci et al. (2015) used the Torus model (Brightman & Nandra 2011). It is, however, known that the Torus model had some calculation errors (Liu & Li 2015, Figure 4). Liu & Li (2015) indicated that the Torus model overestimated the flux in the soft X-rays in the case of the high hydrogen column density in the torus and the edge-on view. Due to this effect, $\log N_{\text{H}}^{\text{LOS}}/\text{cm}^{-2}$ obtained from the XClumpy model are different from those inferred from the Torus model. The second reason is the difference in the observational data. In the observational data, Ricci et al. (2015) did not analyze the NuSTAR observational data, whereas we analyze the NuSTAR observational data. Appendix A discusses why $\log N_{\text{H}}^{\text{LOS}}/\text{cm}^{-2}$ of this study differ from those of Ricci et al. (2015) in detail.

We note that Figure 8(a) does not mean that Ricci et al. (2015) overestimated the CTAGN fraction. Our parent sample consists only of sources classified as CTAGN from the best-fitting $\log N_{\text{H}}^{\text{LOS}}/\text{cm}^{-2}$ obtained from Ricci et al. (2015). We find that $N_{\text{H}}^{\text{LOS}}$ varies depending on the observational data and the torus model. In other words, there is a possibility that an object that was

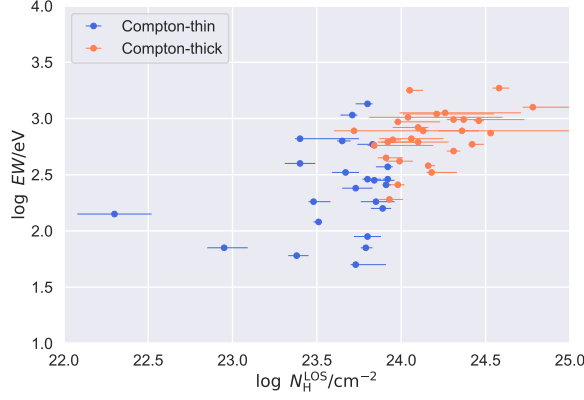


Figure 9. The scatter plot of the logarithmic hydrogen column density along the line of sight ($\log N_{\text{H}}^{\text{LOS}}/\text{cm}^{-2}$) and the logarithmic equivalent of the Fe K α line ($\log \text{EW}/\text{eV}$).

Compton-thin AGN in their analysis may become a Compton-thick AGN as a result of the application of the XClumpy model. In fact, the largest number of AGN detected by Swift/BAT are $23 \leq \log N_{\text{H}}^{\text{LOS}}/\text{cm}^{-2} \leq 24$, so even a few such sources can have a significant impact on the CTAGN fraction. To obtain the true CTAGN fraction, we need to analyze all object that were classified as a Compton-thin AGN by them with XClumpy model in the future.

We study the correlation between $\log N_{\text{H}}^{\text{LOS}}/\text{cm}^{-2}$ and the equivalent width of the Fe K α line ($\log \text{EW}/\text{eV}$). This is because $\log \text{EW}/\text{eV}$ have been commonly used for CTAGN diagnosis. For instance, [Murphy & Yaqoob \(2009\)](#) investigated the correlation between $\log N_{\text{H}}^{\text{Equ}}/\text{cm}^{-2}$ and $\log \text{EW}/\text{eV}$ by using the MYTorus model ([Murphy & Yaqoob 2009](#), Figure 8). They suggested that $\log \text{EW}/\text{eV}$ would be larger than 2.5 in the case of CTAGN. [Figure 9](#) plots that the correlation between $\log N_{\text{H}}^{\text{LOS}}/\text{cm}^{-2}$ and $\log \text{EW}/\text{eV}$. [Figure 9](#) shows that almost all the objects are Compton-thin AGNs in $\log \text{EW}/\text{eV} \leq 2.5$, and almost all the objects are Compton-thick AGNs in $3.0 \leq \log \text{EW}/\text{eV}$. However, in the case of $2.5 < \log \text{EW}/\text{eV} < 3.0$, it is difficult to classify whether the object is a Compton-thin AGN or a Compton-thick AGN. This result is slightly different from [Murphy & Yaqoob \(2009\)](#). This is because $\log \text{EW}/\text{eV}$ depends on the geometric structure of the torus. In the case of the XClumpy model, $\log \text{EW}/\text{eV}$ is larger than that of the MYTorus model since the Fe K α emission lines can pass through the clumpy torus ([Tanimoto et al. 2019](#), Figure 4).

6.2. Torus Covering Factor and Radiation-Regulated AGN Unification Model

The torus covering factor plays an important role in determining the ratio of type-1 and type-2 AGNs. Here we define the Compton-thin torus covering factor (C_{22}) as the percentage of the AGN that is covered by a material whose logarithmic hydrogen column density along the line of sight ($\log N_{\text{H}}^{\text{LOS}}/\text{cm}^{-2}$) is larger than 22.

There are two ways to determine C_{22} . The first way to determine C_{22} is to examine the $\log N_{\text{H}}^{\text{LOS}}/\text{cm}^{-2}$ distribution by investigating $\log N_{\text{H}}^{\text{LOS}}/\text{cm}^{-2}$ for each source. [Ricci et al. \(2017c\)](#) systematically analyzed X-ray spectra of 838 AGNs detected by the Swift/BAT 70-month catalog ([Baumgartner et al. 2013](#)) and estimated $\log N_{\text{H}}^{\text{LOS}}/\text{cm}^{-2}$ for all objects. They suggested that the Eddington ratio (R_{Edd}) is a key parameter to determine C_{22} . If R_{Edd} is larger than effective R_{Edd} of the dusty gas ($\log R_{\text{Edd}} \simeq -2.0$), the radiation pressure blows the dusty gas away. As a result, C_{22} is large in the case of low Eddington ratio ($\log R_{\text{Edd}} \leq -2.0$), whereas C_{22} becomes small in the case of high Eddington ratio ($-2.0 \leq \log R_{\text{Edd}}$) ([Ricci et al. 2017a](#), Figure 4). This model is called the radiation-regulated AGN unification model. In fact, [Ananna et al. \(2022\)](#) indicated the clear difference in the Eddington ratio distribution functions of type-1 and type-2 AGNs.

The second way to determine C_{22} is to analyze the X-ray spectrum by using a torus model that can change the geometric structure of the torus, such as the UXCLUMPY model ([Buchner et al. 2019](#)) and the XClumpy model ([Tanimoto et al. 2019](#)). In this method, we can examine “individual” C_{22} rather than “statistical” C_{22} that have been mainly examined so far. Here we use the XClumpy model. In the case of the XClumpy model, we can define C_{22} in the following way. We express Equation 3 using the elevation angle ($\theta = i - \pi/2$)

$$N_{\text{H}}^{\text{LOS}}(\theta) = N_{\text{H}}^{\text{Equ}} \exp\left(-\frac{\theta^2}{\sigma^2}\right). \quad (4)$$

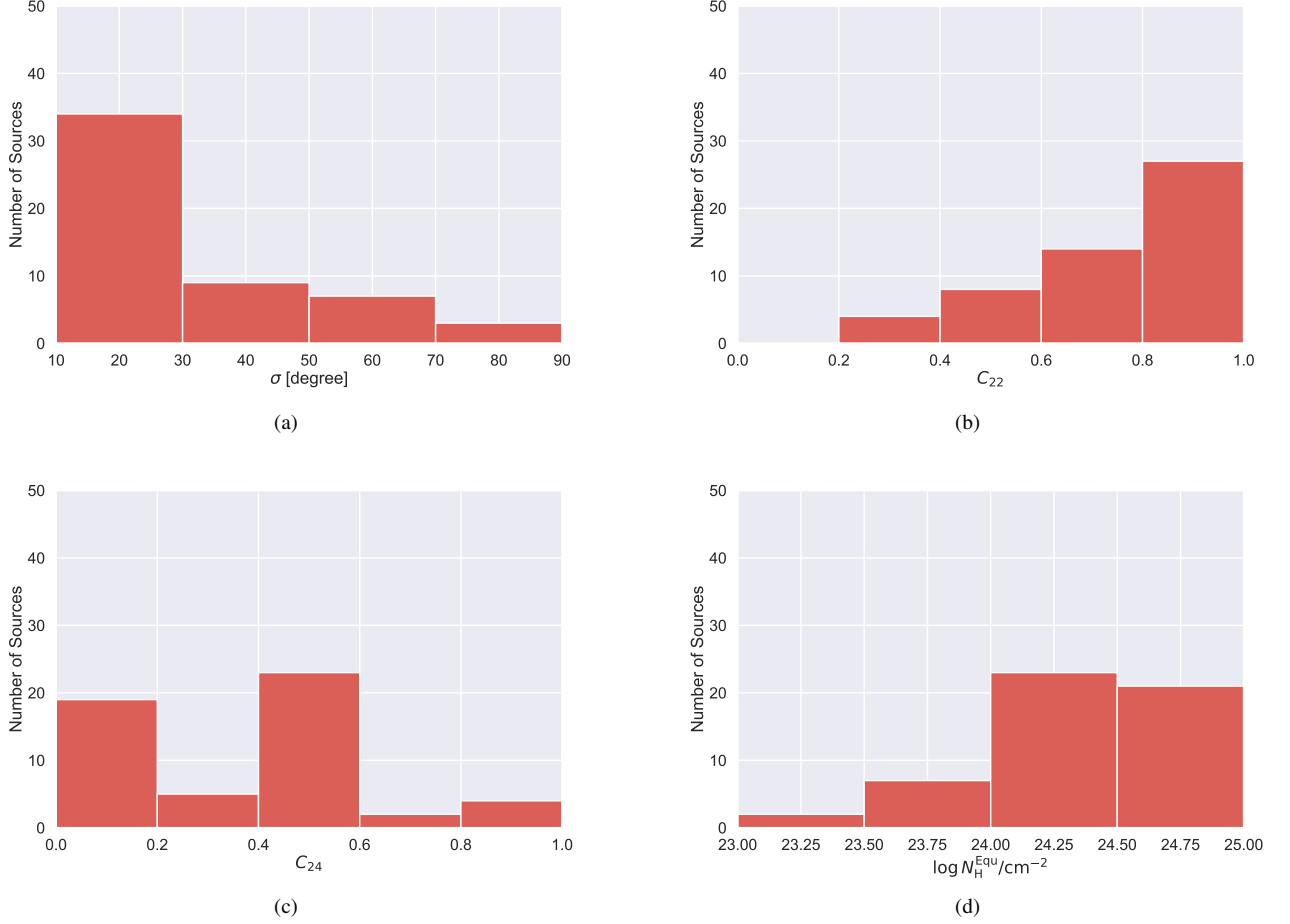


Figure 10. (a) The distribution of the torus angular width (σ). (b) The distribution of the Compton-thin torus covering factor (C_{22}). (c) The distribution of the Compton-thick torus covering factor (C_{24}). (d) The distribution of the logarithmic hydrogen column density along the equatorial direction ($\log N_{\text{H}}^{\text{Equ}}/\text{cm}^{-2}$)

Here we define θ_{22} corresponding to $\log N_{\text{H}}^{\text{LOS}}/\text{cm}^{-2} = 22$ as follows.

$$\theta_{22} = \sigma \left[\ln \left(\frac{N_{\text{H}}^{\text{Equ}}}{10^{22} \text{ cm}^{-2}} \right) \right]^{\frac{1}{2}}. \quad (5)$$

Using θ_{22} , we can obtain individual C_{22} based on the following equation:

$$\begin{aligned} C_{22} &= \frac{1}{4\pi} \int_{\frac{\pi}{2}-\theta_{22}}^{\frac{\pi}{2}+\theta_{22}} \int_0^{2\pi} \sin \theta d\theta d\phi. \\ &= \sin \left(\sigma \left[\ln \left(\frac{N_{\text{H}}^{\text{Equ}}}{10^{22} \text{ cm}^{-2}} \right) \right]^{\frac{1}{2}} \right). \end{aligned} \quad (6)$$

Similarly, we can define the Compton-thick torus covering factor (C_{24}) as follows.

$$C_{24} = \sin \left(\sigma \left[\ln \left(\frac{N_{\text{H}}^{\text{Equ}}}{10^{24} \text{ cm}^{-2}} \right) \right]^{\frac{1}{2}} \right). \quad (7)$$

Table 4 shows the logarithmic observed fluxes, the logarithmic intrinsic luminosities, the Compton-thin torus covering factor, the Compton-thick torus covering factor, and the Eddington ratio.

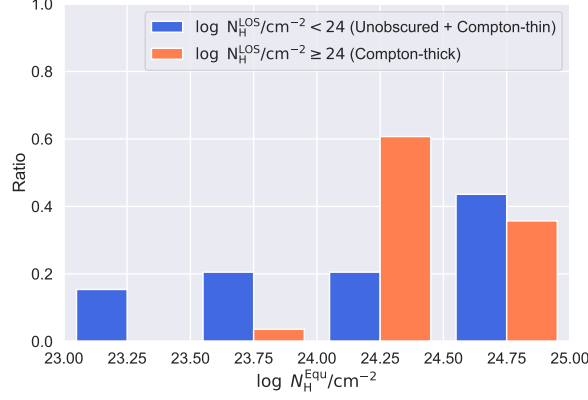


Figure 11. The normalized distribution of $\log N_{\text{H}}^{\text{Equ}}/\text{cm}^{-2}$. The blue histogram represents $\log N_{\text{H}}^{\text{Equ}}/\text{cm}^{-2}$ of unobscured AGNs and Compton-thin AGNs, and the orange histogram shows $\log N_{\text{H}}^{\text{Equ}}/\text{cm}^{-2}$ of Compton-thick AGNs. Here we consider 29 CTAGNs (28 objects in this work and the Circinus Galaxy) and 40 less obscured AGNs (24 objects in this work and 16 objects in Ogawa et al. (2021)). We note that Compton-thin AGNs represent the object whose logarithmic hydrogen column density along the line of sight ($\log N_{\text{H}}^{\text{LOS}}/\text{cm}^{-2}$) is smaller than 24 and unobscured AGNs mean the object whose $\log N_{\text{H}}^{\text{Equ}}/\text{cm}^{-2}$ is smaller than 22.

6.3. Distribution of Torus Covering Factor

We study the distribution of the torus covering factors. Here we add the Circinus Galaxy fitted with the XClumpy model (Tanimoto et al. 2019) to our sample. Hence our sample consists of 28 Compton-thin AGNs and 25 Compton-thick AGNs. Figure 10 plots the distributions of (a) the torus angular width (σ), (b) the Compton-thin torus covering factor (C_{22}), (c) the Compton-thick torus covering factor (C_{24}), and (d) the logarithmic hydrogen column density along the equatorial direction ($\log N_{\text{H}}^{\text{Equ}}/\text{cm}^{-2}$). Figure 10(a) shows that 34 objects have small torus angular width ($\sigma \leq 30^\circ$) and 19 objects have large torus angular width ($30^\circ \leq \sigma$). This could be because we limit the inclination angle within a range of 60° – 87° . In this case, we note that we may underestimate C_{22} and C_{24} . Nevertheless, Figure 10(b) suggests that about 40 objects show large Compton-thin torus covering factor ($0.6 \leq C_{22} \leq 1.0$). Figure 10(d) shows that nine objects have Compton-thin $\log N_{\text{H}}^{\text{Equ}}/\text{cm}^{-2}$ and 43 objects have Compton-thick $\log N_{\text{H}}^{\text{Equ}}/\text{cm}^{-2}$. Especially, 20 objects have very large $\log N_{\text{H}}^{\text{Equ}}/\text{cm}^{-2}$ ($24.5 \leq \log N_{\text{H}}^{\text{Equ}}/\text{cm}^{-2}$). In the radiative regulated AGN unification model (Ricci et al. 2017a), $\log N_{\text{H}}^{\text{Equ}}/\text{cm}^{-2}$ has been considered to be basically constant. Our results suggest, however, that $\log N_{\text{H}}^{\text{Equ}}/\text{cm}^{-2}$ may vary from object to object.

To study whether $\log N_{\text{H}}^{\text{Equ}}/\text{cm}^{-2}$ is different between CTAGNs and less obscured AGNs (unobscured AGNs and Compton-thin AGNs), we compare the $\log N_{\text{H}}^{\text{Equ}}/\text{cm}^{-2}$ of CTAGNs with $\log N_{\text{H}}^{\text{Equ}}/\text{cm}^{-2}$ of less obscured AGNs. Here unobscured AGNs mean the object whose logarithmic hydrogen column density along the line of sight ($\log N_{\text{H}}^{\text{LOS}}/\text{cm}^{-2}$) is smaller than 22 and Compton-thin AGNs represent the object whose $\log N_{\text{H}}^{\text{LOS}}/\text{cm}^{-2}$ is smaller than 24. Figure 11 compares normalized $\log N_{\text{H}}^{\text{Equ}}/\text{cm}^{-2}$ distribution of CTAGNs and that of less obscured AGNs. Here we consider 29 CTAGNs (28 objects in this work and the Circinus Galaxy) and 40 less obscured AGNs (24 objects in this work and 16 objects in previous work)⁵. Figure 11 suggests that some of less obscured AGNs have Compton-thin $\log N_{\text{H}}^{\text{Equ}}/\text{cm}^{-2}$. To investigate whether these distributions are essentially different, we perform the Kolmogorov–Smirnov test and obtain $p = 0.02$. Hence CTAGNs have a larger $\log N_{\text{H}}^{\text{Equ}}/\text{cm}^{-2}$ than that of less obscured AGNs, and may be at a different evolutionary stage from these populations.

⁵ Ogawa et al. (2021) applied the XClumpy model to the X-ray spectra of 16 less obscured AGNs.

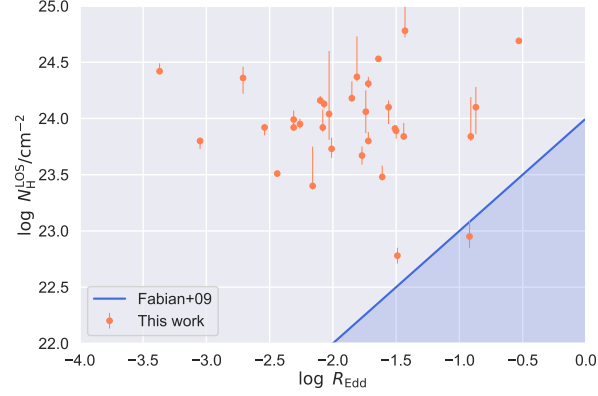


Figure 12. The scatter plot of the logarithmic Eddington ratio ($\log R_{\text{Edd}}$) and the logarithmic hydrogen column density along the line of sight ($\log N_{\text{H}}^{\text{LOS}}$). Blue region represents that the radiation pressure push away the obscuring material (forbidden region: Fabian et al. 2009).

6.4. Validation of Radiation-Regulated AGN Unification Model

To validate the radiation-regulated AGN unification model, we investigate the correlation between the logarithmic Eddington ratio ($\log R_{\text{Edd}}$) and the logarithmic hydrogen column density along the line of sight ($\log N_{\text{H}}^{\text{LOS}}/\text{cm}^{-2}$). Figure 12 plots the correlation between $\log R_{\text{Edd}}$ and $\log N_{\text{H}}^{\text{LOS}}/\text{cm}^{-2}$. The blue region represents the area where the radiation pressure blows away the obscuring material (forbidden region: Fabian et al. 2009). Figure 12 shows that 31 out of 32 objects have a higher $\log N_{\text{H}}^{\text{LOS}}/\text{cm}^{-2}$ than this forbidden region. Hence our sample is expected to have a large Compton-thin torus covering factor (C_{22}) because the radiation pressure cannot blow away the obscuring material.

Figure 13(a) plots the correlation between the logarithmic Eddington ratio ($\log R_{\text{Edd}}$) and the Compton-thin torus covering factor (C_{22}). Here we plot 28 objects whose black hole masses are known and whose C_{22} are determined. Figure 13(b) plots the correlation between $\log R_{\text{Edd}}$ and mean C_{22} in the four $\log R_{\text{Edd}}$ bins. Figure 13(b) indicates that C_{22} of this work is consistent with that of Ricci et al. (2017a) in the low Eddington ratio ($\log R_{\text{Edd}} \leq -1.0$), while C_{22} of this work is larger than that of Ricci et al. (2017a) in the high Eddington ratio ($-1.0 \leq \log R_{\text{Edd}}$). This is because our sample has a larger $\log N_{\text{H}}^{\text{LOS}}/\text{cm}^{-2}$ than that of forbidden region. In fact, Kawakatu et al. (2020) studied the obscuring structure of circumnuclear disks by considering supernova feedbacks and suggested that if $\log N_{\text{H}}^{\text{LOS}}/\text{cm}^{-2}$ is sufficiently large, the feedback is less effective and the torus covering factor is approximately equal to 0.80 (Kawakatu et al. 2020, Figure 2).

Figure 14(a) plots the correlation between the logarithmic Eddington ratio ($\log R_{\text{Edd}}$) and the Compton-thick torus covering factor (C_{24}). Here we plot 29 objects whose black hole masses are known and whose C_{24} are determined. Figure 14(b) plots the correlation between $\log R_{\text{Edd}}$ and mean C_{24} in the four $\log R_{\text{Edd}}$ bins. Figure 14(b) shows that the average value of C_{24} ($C_{24} = 36_{-4}^{+4}\%$). Here we apply the standard error as the error of C_{24} . The average C_{24} of this work is larger than that of Ricci et al. (2017a) ($C_{24} = 27_{-4}^{+4}\%$). In the case of Ricci et al. (2017a), they utilized AGNs detected by the Swift/BAT to calculate the statistical C_{24} . Here they assumed that if $\log R_{\text{Edd}}$ was the same, then $\log N_{\text{H}}^{\text{Equ}}/\text{cm}^{-2}$ would also be the same. As we mentioned in Section 6.3, however, $\log N_{\text{H}}^{\text{Equ}}/\text{cm}^{-2}$ of CTAGNs are larger than those of less obscured AGNs. In other words, C_{24} value will be larger than that of Ricci et al. (2017a). This implies that some CTAGNs cannot be detected by Swift/BAT all-sky hard X-ray survey even in the local Universe (e.g., Boorman et al. 2016, 2018; LaMassa et al. 2019; Zhao et al. 2019a,b, 2020).

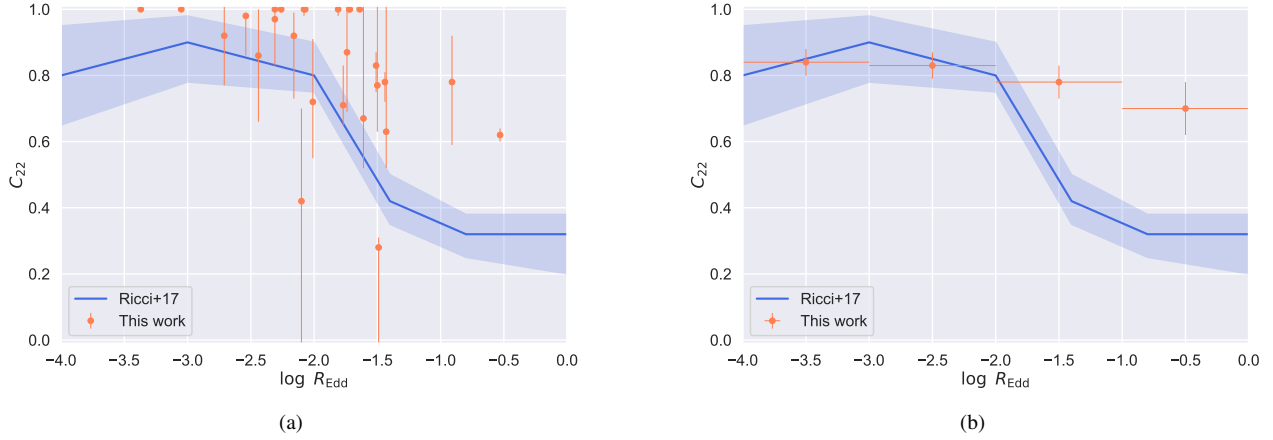


Figure 13. (a) Correlation between the logarithmic Eddington ratio ($\log R_{\text{Edd}}$) and the Compton-thin torus covering factor (C_{22}). Blue line represents the radiation regulated AGN unification model (Ricci et al. 2017b). (b) Correlation between $\log R_{\text{Edd}}$ and mean C_{22} in the four $\log R_{\text{Edd}}$ bins. Note that we apply the standard error as the error of C_{22} .

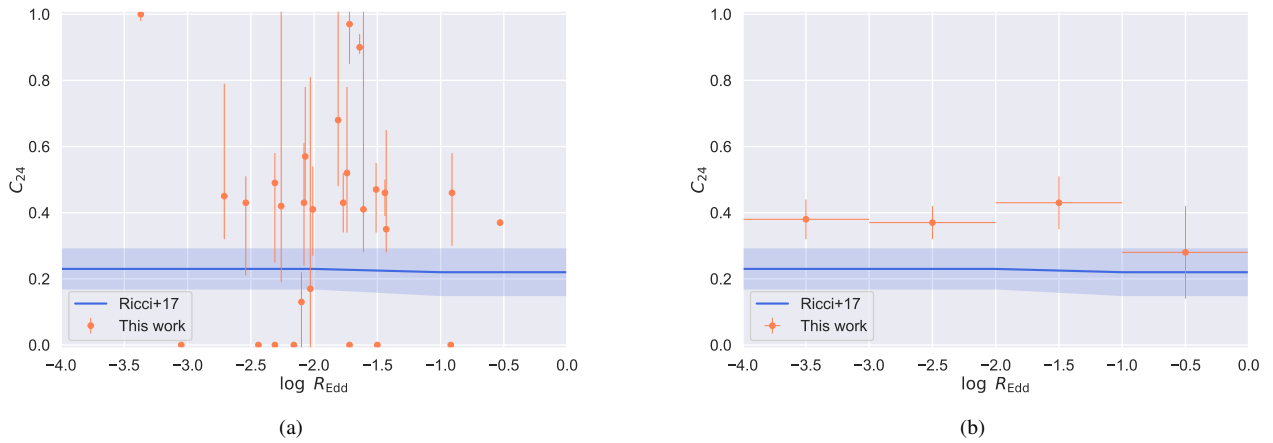


Figure 14. (a) Correlation between the logarithmic Eddington ratio ($\log R_{\text{Edd}}$) and the Compton-thick torus covering factor (C_{24}). Blue line represents the radiation regulated AGN unification model (Ricci et al. 2017b). (b) Correlation between $\log R_{\text{Edd}}$ and mean C_{24} in the four $\log R_{\text{Edd}}$ bins. Note that we apply the standard error as the error of C_{24} .

7. CONCLUSION

1. We apply the XClumpy model to the broadband X-ray spectra of 52 CTAGN candidates observed with Chandra, XMM–Newton, Swift, Suzaku, and NuSTAR. Our model can reproduce the X-ray spectra of all objects.
2. The hydrogen column density along the line of sight ($N_{\text{H}}^{\text{LOS}}$) obtained from this work indicates that 24 objects are Compton-thin AGNs and 28 objects are Compton-thick AGNs within the 90% confidence interval. The main reason is the difference in the torus model applied.
3. We compare the normalized histogram of the hydrogen column density along the equatorial direction ($N_{\text{H}}^{\text{Equ}}$) of CTAGNs and that of less obscured AGNs. $N_{\text{H}}^{\text{Equ}}$ of CTAGNs are larger than that of less obscured AGNs. This suggests that the structure of CTAGN may be intrinsically different from that of less obscured AGN.
4. We study the correlation between the logarithmic Eddington ratio ($\log R_{\text{Edd}}$) and the Compton-thin torus covering factor (C_{22}). C_{22} obtained from the XClumpy model is consistent with that inferred from Ricci et al. (2017c) in the low Eddington ratio ($\log R_{\text{Edd}} \leq -1.0$), whereas C_{22} obtained from the XClumpy model is larger than that inferred from Ricci et al. (2017c) in the high Eddington ratio ($-1.0 \leq \log R_{\text{Edd}}$). This suggests that if the hydrogen column density is sufficiently large, it is difficult to blow it away by radiation pressure. In other words, there are objects with large C_{22} even in the high Eddington ratio.
5. We examine the correlation between the logarithmic Eddington ratio ($\log R_{\text{Edd}}$) and the Compton-thick torus covering factor (C_{24}). The average value of C_{24} is equal to $36^{+4}_{-4}\%$. This value is larger than that of Ricci et al. (2015) ($C_{24} = 27^{+4}_{-4}\%$) based on the assumption that all AGNs have intrinsically the same torus structure.
6. The above results (3–5) suggest that the structure of CTAGN may be intrinsically different from that of less obscured AGN.

ACKNOWLEDGMENTS

We acknowledge the anonymous referee for the helpful suggestions that incorporated the Article. This work was supported by the Grant-in-Aid for JSPS Fellows 20J00119 (A.T.) and 19J22216 (S.Y.), and by the Grants-in-Aid for Scientific Research 20H01946 (Y.U.) and 19H01906 (H.O.). Numerical computations were carried out on Cray XC50 at Center for Computational Astrophysics, National Astronomical Observatory of Japan. This research has made use of data and/or software provided by the High Energy Astrophysics Science Archive Research Center (HEASARC), which is a service of the Astrophysics Science Division at NASA/GSFC and the High Energy Astrophysics Division of the Smithsonian Astrophysical Observatory. This research has also made use of the NASA/IPAC Extragalactic Database (NED), which is operated by the Jet Propulsion Laboratory, California Institute of Technology, under contract with the National Aeronautics and Space Administration.

Facilities: Chandra, NuSTAR, Suzaku, Swift, XMM–Newton.

Software: HEASoft 6.28 (HEASARC 2020), XSPEC (Arnaud 1996).

Table 5. Comparison of Hydrogen Column Density along the Line of Sight

Galaxy Name (1)	This work		Ricci et al. (2015)		Consistency (6)
	XClumpy (2)	Borus02 (3)	Torus (4)	Observatory (5)	
ESO 112-G006	23.79 ^{+0.04} _{-0.03}	23.81 ^{+0.04} _{-0.04}	24.03 ^{+0.40} _{-0.24}	Swift/XRT	Yes
MCG -07-03-007	23.95 ^{+0.05} _{-0.04}	23.85 ^{+0.05} _{-0.03}	24.18 ^{+0.12} _{-0.23}	Swift/XRT	Yes
NGC 0424	23.92 ^{+0.16} _{-0.04}	23.86 ^{+0.05} _{-0.05}	24.33 ^{+0.01} _{-0.01}	XMM-Newton	No
MCG +08-03-018	23.73 ^{+0.10} _{-0.08}	23.87 ^{+0.04} _{-0.15}	24.24 ^{+0.34} _{-0.15}	Swift/XRT	No
2MASX J01290761-6038423	23.98 ^{+0.04} _{-0.08}	23.81 ^{+0.07} _{-0.10}	24.13 ^{+0.19} _{-0.23}	Swift/XRT	Yes
ESO 244-IG030	22.78 ^{+0.07} _{-0.07}	22.81 ^{+0.08} _{-0.08}	24.20 ^{+0.35} _{-0.18}	Swift/XRT	No
NGC 1106	24.58 ^{+0.06} _{-0.04}	24.28 ^{+0.03} _{-0.09}	24.25 ^{+0.29} _{-0.17}	Swift/XRT	Yes
2MFGC 02280	24.31 ^{+0.04} _{-0.04}	24.39 ^{+0.02} _{-0.27}	24.06 ^{+0.12} _{-0.10}	Swift/XRT	No
NGC 1125	24.06 ^{+0.19} _{-0.19}	24.14 ^{+0.09} _{-0.10}	24.27 ^{+0.32} _{-0.24}	Swift/XRT	Yes
NGC 1194	23.92 ^{+0.03} _{-0.07}	23.88 ^{+0.05} _{-0.03}	24.33 ^{+0.06} _{-0.03}	XMM-Newton	No
NGC 1229	23.67 ^{+0.08} _{-0.08}	23.61 ^{+0.14} _{-0.02}	24.94 ^{+1.06} _{-0.45}	Swift/XRT	No
ESO 201-IG004	23.40 ^{+0.09} _{-0.09}	23.61 ^{+0.21} _{-0.20}	24.32 ^{+0.03} _{-0.07}	XMM-Newton	No
2MASX J03561995-6251391	23.80 ^{+0.08} _{-0.08}	23.86 ^{+0.01} _{-0.09}	24.17 ^{+0.04} _{-0.21}	Swift/XRT	No
MCG -02-12-017	23.38 ^{+0.07} _{-0.05}	23.34 ^{+0.10} _{-0.05}	24.25 ^{+1.01} _{-0.46}	Swift/XRT	No
CGCG 420-015	23.91 ^{+0.03} _{-0.02}	23.86 ^{+0.02} _{-0.03}	24.14 ^{+0.04} _{-0.21}	XMM-Newton	Yes
ESO 005-G004	23.71 ^{+0.03} _{-0.07}	23.78 ^{+0.07} _{-0.04}	24.34 ^{+0.10} _{-0.06}	Suzaku	No
Mrk 0003	23.92 ^{+0.01} _{-0.03}	23.90 ^{+0.02} _{-0.02}	24.07 ^{+0.06} _{-0.04}	XMM-Newton	No
2MASX J06561197-4919499	23.99 ^{+0.08} _{-0.08}	23.91 ^{+0.06} _{-0.03}	24.03 ^{+0.30} _{-0.10}	Swift/XRT	Yes
MCG +06-16-028	23.84 ^{+0.12} _{-0.03}	23.84 ^{+0.04} _{-0.06}	24.80 ^{+1.20} _{-0.75}	Swift/XRT	No
Mrk 0078	23.80 ^{+0.08} _{-0.03}	23.82 ^{+0.05} _{-0.10}	24.11 ^{+0.08} _{-0.12}	XMM-Newton	No
Mrk 0622	23.48 ^{+0.10} _{-0.03}	23.46 ^{+0.09} _{-0.09}	24.29 ^{+1.71} _{-0.30}	XMM-Newton	No
NGC 2788A	24.36 ^{+0.10} _{-0.14}	24.27 ^{+0.06} _{-0.21}	25.55 ^{+0.45} _{-1.41}	Swift/XRT	Yes
SBS 0915+556	22.95 ^{+0.14} _{-0.10}	23.00 ^{+0.13} _{-0.13}	24.01 ^{+0.14} _{-0.15}	Swift/XRT	No
2MASX J09235371-3141305	23.73 ^{+0.18} _{-0.03}	23.76 ^{+0.12} _{-0.03}	24.11 ^{+0.09} _{-0.08}	Swift/XRT	No
ESO 565-G019	24.05 ^{+0.08} _{-0.02}	23.98 ^{+0.08} _{-0.04}	24.65 ^{+1.35} _{-0.17}	Suzaku	No
MCG +10-14-025	24.18 ^{+0.15} _{-0.03}	24.13 ^{+0.09} _{-0.05}	24.35 ^{+0.10} _{-0.04}	XMM-Newton	Yes

Table 5 continued on next page

Table 5 (continued)

Galaxy Name (1)	This work		Ricci et al. (2015)		
	XClumpy (2)	Borus02 (3)	Torus (4)	Observatory (5)	Consistency (6)
NGC 3079	24.42 ^{+0.07} _{-0.02}	24.34 ^{+0.06} _{-0.03}	25.10 ^{+0.90} _{-0.59}	XMM–Newton	No
ESO 317–G041	23.93 ^{+0.08} _{-0.06}	24.04 ^{+0.05} _{-0.04}	24.30 ^{+0.43} _{-0.22}	Swift/XRT	No
SDSS J103315.71+525217.8	23.85 ^{+0.11} _{-0.09}	23.90 ^{+0.04} _{-0.11}	24.27 ^{+0.26} _{-0.21}	Swift/XRT	No
NGC 3393	24.31 ^{+0.06} _{-0.04}	24.23 ^{+0.05} _{-0.03}	24.50 ^{+0.32} _{-0.19}	XMM–Newton	Yes
NGC 4102	23.83 ^{+0.01} _{-0.09}	23.88 ^{+0.09} _{-0.06}	24.18 ^{+0.09} _{-0.12}	XMM–Newton	No
NGC 4180	24.26 ^{+0.45} _{-0.27}	24.13 ^{+0.10} _{-0.02}	24.15 ^{+0.27} _{-0.22}	Swift/XRT	Yes
ESO 323–G032	24.10 ^{+0.06} _{-0.15}	23.89 ^{+0.07} _{-0.14}	24.79 ^{+0.06} _{-0.15}	Suzaku	No
NGC 4945	24.53 ^{+0.01} _{-0.01}	24.43 ^{+0.01} _{-0.01}	24.80 ^{+0.13} _{-0.04}	XMM–Newton	No
IGR 14175–4641	23.89 ^{+0.05} _{-0.07}	23.88 ^{+0.01} _{-0.08}	24.35 ^{+0.19} _{-0.15}	Swift/XRT	No
NGC 5643	23.80 ^{+0.03} _{-0.07}	23.79 ^{+0.01} _{-0.04}	25.40 ^{+0.60} _{-0.34}	XMM–Newton	No
NGC 5728	24.13 ^{+0.03} _{-0.04}	24.06 ^{+0.02} _{-0.02}	24.13 ^{+0.03} _{-0.04}	Suzaku	Yes
CGCG 164–019	23.84 ^{+0.35} _{-0.04}	24.12 ^{+0.19} _{-0.33}	24.75 ^{+0.74} _{-0.15}	Swift/XRT	No
ESO 137–G034	24.46 ^{+0.03} _{-0.03}	24.16 ^{+0.05} _{-0.04}	24.30 ^{+0.07} _{-0.07}	XMM–Newton	No
NGC 6232	24.04 ^{+0.56} _{-0.23}	24.06 ^{+0.59} _{-0.22}	24.94 ^{+1.06} _{-0.41}	Swift/XRT	Yes
ESO 138–G001	23.65 ^{+0.05} _{-0.03}	23.66 ^{+0.05} _{-0.01}	25.25 ^{+0.75} _{-0.31}	XMM–Newton	No
NGC 6240	24.16 ^{+0.04} _{-0.02}	24.10 ^{+0.03} _{-0.03}	24.40 ^{+0.05} _{-0.08}	XMM–Newton	No
NGC 6552	23.98 ^{+0.10} _{-0.05}	23.71 ^{+0.05} _{-0.04}	24.05 ^{+0.35} _{-0.22}	XMM–Newton	Yes
2MASX J20145928+2523010	22.30 ^{+0.22} _{-0.22}	22.28 ^{+0.04} _{-0.04}	24.05 ^{+0.35} _{-0.22}	Swift/XRT	No
ESO 464–G016	23.91 ^{+0.10} _{-0.05}	23.84 ^{+0.02} _{-0.05}	24.19 ^{+0.40} _{-0.25}	Swift/XRT	Yes
NGC 7130	24.37 ^{+0.36} _{-0.04}	24.33 ^{+0.23} _{-0.10}	24.00 ^{+0.21} _{-0.10}	Chandra	No
NGC 7212	24.10 ^{+0.18} _{-0.24}	24.16 ^{+0.20} _{-0.30}	24.41 ^{+0.07} _{-0.07}	XMM–Newton	No
ESO 406–G004	23.72 ^{+2.28} _{-0.12}	24.13 ^{+0.78} _{-0.36}	24.74 ^{+1.26} _{-0.55}	Swift/XRT	Yes
NGC 7479	24.78 ^{+0.26} _{-0.06}	24.15 ^{+0.03} _{-0.06}	24.16 ^{+0.12} _{-0.13}	XMM–Newton	No
SWIFT J2307.9+2245	24.21 ^{+0.34} _{-0.20}	24.27 ^{+0.10} _{-0.36}	24.20 ^{+0.30} _{-0.20}	Swift/XRT	Yes
NGC 7582	23.51 ^{+0.01} _{-0.03}	23.50 ^{+0.01} _{-0.01}	24.33 ^{+0.01} _{-0.01}	XMM–Newton	No
NGC 7682	23.40 ^{+0.35} _{-0.03}	23.63 ^{+0.23} _{-0.18}	24.33 ^{+0.05} _{-0.15}	XMM–Newton	Yes

NOTE—Column (1): galaxy name. Column (2): logarithmic hydrogen column density along the line of sight ($\log N_{\text{H}}^{\text{LOS}}/\text{cm}^{-2}$) obtained from the XClumpy model in this work. Column (3): $\log N_{\text{H}}^{\text{LOS}}/\text{cm}^{-2}$ inferred from the Borus02 model in this work. Column (4): $\log N_{\text{H}}^{\text{LOS}}/\text{cm}^{-2}$ obtained from the Torus model in Ricci et al. (2015). Column (5): observatory in Ricci et al. (2015). Column (6): whether $\log N_{\text{H}}^{\text{LOS}}/\text{cm}^{-2}$ obtained from the XClumpy model is consistent with that inferred from the Torus model within the 90% confidence interval.

APPENDIX

A. COMPARISON OF HYDROGEN COLUMN DENSITY ALONG THE LINE OF SIGHT WITH THAT OF PARENT SAMPLE

To distinguish whether the differences in the logarithmic hydrogen column density along the line of sight ($\log N_{\text{H}}^{\text{LOS}}/\text{cm}^{-2}$), we applied the Borus02 model (Baloković et al. 2018) to the X-ray spectra of all objects. Appendix A.1 introduces the X-ray spectral model of Ricci et al. (2015) and that of our analysis. Appendix A.2 compares $\log N_{\text{H}}^{\text{LOS}}/\text{cm}^{-2}$ obtained from the XClumpy model with those inferred from the Borus02 model and those obtained from Ricci et al. (2015).

A.1. X-Ray Spectral Analysis

We introduce the X-ray spectral model of Ricci et al. (2015) and that of our analysis. First we present the X-ray spectral model of Ricci et al. (2015). The X-ray spectral model is the following:

$$\text{const1} \times \text{phabs} \times (\text{atable}\{\text{torus1006.fits}\} + \text{const2} \times \text{zpowerlaw} + (\text{zgauss}) + (\text{apec})) \quad (\text{A1})$$

This model consists of five components.

1. $\text{const1} \times \text{phabs}$. These components mean the cross calibration constant and the Galactic absorption. These are basically same as the XClumpy model. Ricci et al. (2015) considered the cross calibration constant if statistically required.
2. $\text{atable}\{\text{torus1006.fits}\}$. This component represents the transmitted continuum absorbed by the torus, the reflection continuum, and the fluorescent lines from the torus based on the Torus model (Brightman & Nandra 2011). They assumed that the reprocessing medium is a sphere with conical cutouts at both poles. This model have four free parameters. (1) the photon index (Γ), (2) the hydrogen column density along the equatorial direction ($N_{\text{H}}^{\text{Equ}}$), (3) the opening angle of the torus (θ_{open}), and (4) the inclination angle (θ_{incl}). (2) In the case of the Torus model, $N_{\text{H}}^{\text{Equ}}$ is equal to $N_{\text{H}}^{\text{LOS}}$. (4) They fixed $\theta_{\text{incl}} = 87^\circ$ to reduce the degree of complexity of the model.
3. $\text{const2} \times \text{zpowerlaw}$. This component means the scattered component. This component is the same as the XClumpy model.
4. zgauss . This component represents the fluorescent lines. This component is the same as the XClumpy model.
5. apec . This component means the emission from an optically thin thermal plasma in the host galaxy. This component is the same as the XClumpy model.

We note that the Torus model had some calculation errors (Liu & Li 2015, Figure 4). Liu & Li (2015) indicated that the Torus model overestimated the flux in the soft X-rays in the case of the high hydrogen column density in the torus and the edge-on view. Due to this effect, $\log N_{\text{H}}^{\text{LOS}}/\text{cm}^{-2}$ obtained from the XClumpy model are different from those inferred from the Torus model.

To compare $\log N_{\text{H}}^{\text{LOS}}/\text{cm}^{-2}$ obtained from the XClumpy model with those inferred from other torus models, we applied the Borus02 model (Baloković et al. 2018) to the X-ray spectra of 52 objects. Baloković et al. (2018) fixed the bug in the Torus model and released the Borus02 model whose geometric structure is the same as the Torus model. The X-ray spectral model is the following:

$$\begin{aligned} & \text{const1} \times \text{phabs} \\ & \times (\text{const2} \times \text{zphabs} \times \text{cabs} \times \text{zcutoffpl} \\ & + \text{const3} \times \text{zcutoffpl} + \text{atable}\{\text{borus02_v170323a.fits}\} + (\text{zgauss}) + (\text{apec})). \end{aligned} \quad (\text{A2})$$

This model consists of five components.

1. $\text{const1} \times \text{phabs}$. These components mean the cross calibration constant and the Galactic absorption. These components are the same as the XClumpy model.

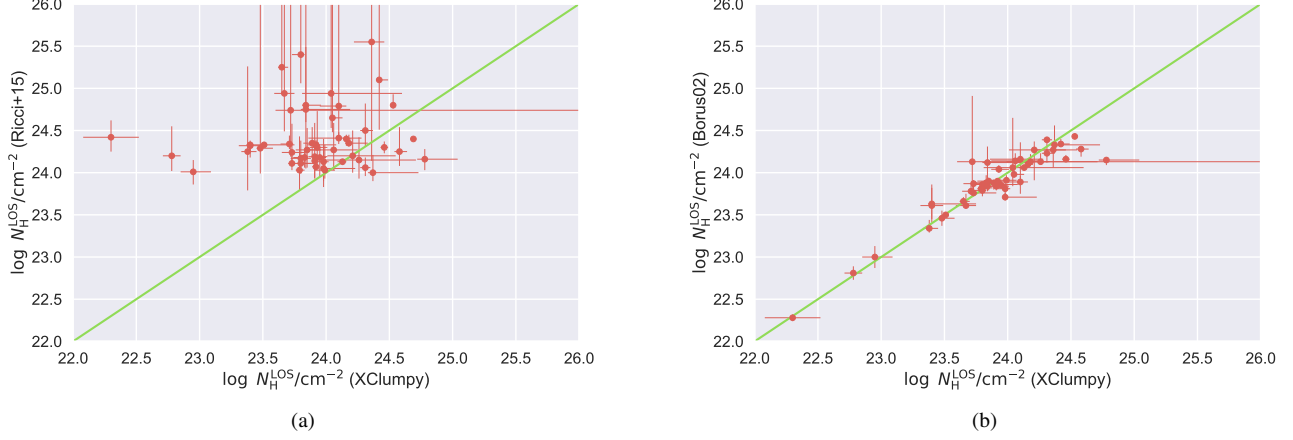


Figure 15. (a) The correlation between the logarithmic hydrogen column density along the line of sight ($\log N_{\text{H}}^{\text{LOS}}/\text{cm}^{-2}$) obtained from the XClumpy model and those inferred from the Torus model (Ricci et al. 2015). (b) The correlation between $\log N_{\text{H}}^{\text{LOS}}/\text{cm}^{-2}$ obtained from the XClumpy model and those inferred from the Borus02 model.

2. $\text{const2} \times \text{zphabs} \times \text{cabs} \times \text{zcutoffpl}$. This component represents the transmitted continuum absorbed by the torus. This component is the basically same as the XClumpy model.
3. $\text{const3} \times \text{zcutoffpl}$. This component means the scattered component. This component is the same as the XClumpy model.
4. `atable{borus02.v170323a.fits}`. This component represent the reflection continuum and the fluorescent lines from the torus based on the Borus02 model (Baloković et al. 2018). This model have six free parameters. (1) the photon index (Γ : 1.4–2.6), (2) the cutoff energy (E_{cut} : 20–2000 keV), (3) the logarithmic hydrogen column density ($\log N_{\text{H}}^{\text{Torus}}/\text{cm}^{-2}$: 22.0–25.5), (4) the torus covering factor (C_{Torus} : 0.1–1.0), (5) the cosine of the inclination angle ($\cos \theta_{\text{inc}}$: 0.05–0.95), and (6) the relative abundance of iron (A_{Fe} : 0.01–10.0). (2) We fixed $E_{\text{cut}} = 370$ keV. (3) In the case of the Borus02 model, $\log N_{\text{H}}^{\text{Torus}}/\text{cm}^{-2}$ is equal to $\log N_{\text{H}}^{\text{LOS}}/\text{cm}^{-2}$. (5) We limited $\cos \theta_{\text{inc}}$ value within a range of 0.05–0.50. Especially, we fix its value at 0.05 for the eight objects (Mrk 0003, NGC 3079, NGC 3393, NGC 4945, NGC 5643, NGC 5728, NGC 6240, and NGC 7479). (6) We fixed $A_{\text{Fe}} = 1.00$.
5. `zgauss`. This component means the fluorescent lines. This component is the same as the XClumpy model.
6. `apec`. This component represents the emission from an optically thin thermal plasma in the host galaxy. This component is the same as the XClumpy model.

A.2. Comparison of Hydrogen Column Density along the Line of Sight among the XClumpy, Borus02, and Torus models

We compare the logarithmic hydrogen column density along the line of sight ($\log N_{\text{H}}^{\text{LOS}}/\text{cm}^{-2}$) obtained from the XClumpy model with that inferred from the Borus02 model and that obtained from the Torus model (Ricci et al. 2015). Table 5 summarizes $\log N_{\text{H}}^{\text{LOS}}/\text{cm}^{-2}$ inferred from the XClumpy model, the Borus02 model, and the Torus model (Ricci et al. 2015). Table 5 shows that $\log N_{\text{H}}^{\text{LOS}}/\text{cm}^{-2}$ of 34 objects obtained from the XClumpy model are not consistent with those inferred from the Torus model (Ricci et al. 2015) within the 90% confidence interval. As mentioned in Appendix A.1, the main reason seems to be a calculation error in the Torus model (Liu & Li 2015). In fact, we applied the Torus model to the X-ray spectra of several objects and confirmed that it can reproduce $\log N_{\text{H}}^{\text{LOS}}/\text{cm}^{-2}$ of Ricci et al. (2015). We note that in the case of 14 objects that Ricci et al. (2015) have analyzed the Swift/XRT data for, the reason could also be the observational data.

To study how much $\log N_{\text{H}}^{\text{LOS}}/\text{cm}^{-2}$ varies with the applied torus model, we investigate the correlation between $\log N_{\text{H}}^{\text{LOS}}/\text{cm}^{-2}$ obtained from the XClumpy model and those inferred from the Borus02 model. Figure 15 plots (a) the correlation between $\log N_{\text{H}}^{\text{LOS}}/\text{cm}^{-2}$ obtained from the XClumpy model and those inferred from the Torus model (Ricci et al. 2015) and (b) the correlation between $\log N_{\text{H}}^{\text{LOS}}/\text{cm}^{-2}$ obtained from the XClumpy model and those inferred from the Borus02 model. Figure 15(a) shows that $\log N_{\text{H}}^{\text{LOS}}/\text{cm}^{-2}$ obtained from the XClumpy model are different from those inferred from the Torus model (Ricci et al. 2015), while Figure 15(b) indicates that $\log N_{\text{H}}^{\text{LOS}}/\text{cm}^{-2}$ obtained from the XClumpy model are consistent with those inferred from the Borus02 model. This result supports that the reason why $\log N_{\text{H}}^{\text{LOS}}/\text{cm}^{-2}$ obtained from the

XClumpy model are different from those inferred from the Torus model (Ricci et al. 2015) is due to a calculation error in the Torus model (Liu & Li 2015).

Table 6. Best Fitting Parameters of Previous Studies

Galaxy Name (1)	Model (2)	Satellite1 (3)	Satellite2 (4)	$N_{\text{H}}^{\text{LOS}}$ (5)	Γ (6)	Reference (7)
ESO 112–G006	Borus02	XMM–Newton	NuSTAR	$0.63^{+0.04}_{-0.06}$	$1.60^{+0.23}_{-0.13}$	(06)
MCG –07–03–007	Borus02	XMM–Newton	NuSTAR	$0.90^{+0.07}_{-0.08}$	$1.84^{+0.12}_{-0.15}$	(06)
NGC 0424	Borus02	XMM–Newton	NuSTAR	$2.65^{+0.44}_{-0.36}$	$1.81^{+0.07}_{-0.05}$	(05)
MCG +08–03–018	Borus02	Swift	NuSTAR	$1.07^{+0.24}_{-0.22}$	$2.17^{+0.26}_{-0.19}$	(05)
2MASX J01290761–6038423
ESO 244–IG030	Borus02	XMM–Newton	NuSTAR	$0.06^{+0.01}_{-0.01}$	$1.85^{+0.17}_{-0.17}$	(04)
NGC 1106
2MFGC 02280	MYTorus	Swift	NuSTAR	$3.16^{+0.35}_{-0.30}$	$2.10^{+0.10}_{-0.10}$	(02)
NGC 1125
NGC 1194	Borus02	XMM–Newton	NuSTAR	$2.47^{+0.41}_{-0.08}$	$1.86^{+0.09}_{-0.05}$	(05)
NGC 1229	Borus02	Swift	NuSTAR	$0.35^{+0.10}_{-0.07}$	$1.57^{+0.14}_{-0.16}$	(05)
ESO 201–IG004	Borus02	XMM–Newton	NuSTAR	$1.34^{+0.36}_{-0.32}$	$1.69^{+0.21}_{-0.21}$	(05)
2MASX J03561995–6251391	Borus02	Swift	NuSTAR	$0.84^{+0.11}_{-0.11}$	$1.99^{+0.20}_{-0.26}$	(05)
MCG –02–12–017
CGCG 420–015	Borus02	XMM–Newton	NuSTAR	$1.50^{+0.25}_{-0.22}$	$1.92^{+0.14}_{-0.13}$	(05)
ESO 005–G004	Borus02	Swift	NuSTAR	$2.48^{+0.86}_{-0.62}$	$1.47^{+0.12}_{-0.07}$	(05)
Mrk 0003	Borus02	XMM–Newton	NuSTAR	$0.80^{+0.03}_{-0.02}$	$1.68^{+0.03}_{-0.02}$	(05)
2MASX J06561197–4919499
MCG +06–16–028	Borus02	Swift	NuSTAR	$0.82^{+0.11}_{-0.11}$	$1.83^{+0.15}_{-0.15}$	(05)
Mrk 0078	Borus02	XMM–Newton	NuSTAR	$0.81^{+0.29}_{-0.03}$	$1.40^{+0.21}_{-0.03}$	(07)
Mrk 0622	Borus02	XMM–Newton	NuSTAR	$0.24^{+0.03}_{-0.04}$	$1.74^{+0.12}_{-0.13}$	(06)
NGC 2788A
SBS 0915+556
2MASX J09235371–3141305	Borus02	Swift	NuSTAR	$0.63^{+0.09}_{-0.06}$	$2.01^{+0.10}_{-0.13}$	(05)
ESO 565–G019
MCG +10–14–025	Ikeda model	XMM–Newton	NuSTAR	$1.31^{+0.31}_{-0.36}$	$1.63^{+0.27}_{-0.13}$	(03)

Table 6 continued on next page

Table 6 (continued)

Galaxy Name (1)	Model (2)	Satellite1 (3)	Satellite2 (4)	$N_{\text{H}}^{\text{LOS}}$ (5)	Γ (6)	Reference (7)
NGC 3079	Borus02	XMM–Newton	NuSTAR	$1.51^{+0.19}_{-0.09}$	$1.93^{+0.06}_{-0.10}$	(05)
ESO 317–G041	Borus02	XMM–Newton	NuSTAR	$0.71^{+0.14}_{-0.15}$	$1.56^{+0.20}_{-0.16}$	(04)
SDSS J103315.71+525217.8	Borus02	XMM–Newton	NuSTAR	$1.17^{+0.38}_{-0.32}$	1.40 (fixed)	(04)
NGC 3393	Borus02	XMM–Newton	NuSTAR	$2.58^{+1.32}_{-0.87}$	$1.72^{+0.22}_{-0.13}$	(05)
NGC 4102	Borus02	XMM–Newton	NuSTAR	$0.62^{+0.09}_{-0.08}$	$1.75^{+0.09}_{-0.11}$	(05)
NGC 4180
ESO 323–G032	Borus02	XMM–Newton	NuSTAR	$1.75^{+1.46}_{-0.49}$	$2.02^{+0.13}_{-0.30}$	(06)
NGC 4945	Borus02	XMM–Newton	NuSTAR	$3.97^{+0.15}_{-0.15}$	$1.95^{+0.05}_{-0.05}$	(05)
IGR 14175–4641	Borus02	Swift	NuSTAR	$0.86^{+0.25}_{-0.19}$	$1.70^{+0.21}_{-0.19}$	(05)
NGC 5643	Borus02	XMM–Newton	NuSTAR	$2.69^{+1.88}_{-0.65}$	$1.55^{+0.13}_{-0.15}$	(05)
NGC 5728	Borus02	Chandra	NuSTAR	$0.97^{+0.05}_{-0.03}$	$1.81^{+0.07}_{-0.04}$	(05)
CGCG 164–019	Borus02	Swift	NuSTAR	$1.37^{+0.57}_{-0.45}$	$1.79^{+0.36}_{-0.32}$	(05)
ESO 137–G034	MYTorus	...	NuSTAR	$2.90^{+0.86}_{-0.54}$...	(01)
NGC 6232	Borus02	Swift	NuSTAR	$0.63^{+0.13}_{-0.24}$	1.40 (fixed)	(05)
ESO 138–G001
NGC 6240	Borus02	XMM–Newton	NuSTAR	$1.10^{+0.10}_{-0.08}$	$1.75^{+0.04}_{-0.03}$	(05)
NGC 6552	Borus02	XMM–Newton	NuSTAR	$2.18^{+0.38}_{-0.35}$	$1.76^{+0.08}_{-0.12}$	(06)
2MASX J20145928+2523010
ESO 464–G016	Borus02	Swift	NuSTAR	$0.86^{+0.25}_{-0.17}$	$1.67^{+0.29}_{-0.27}$	(05)
NGC 7130	Borus02	Chandra	NuSTAR	$3.43^{+6.57}_{-1.26}$	1.40 (fixed)	(05)
NGC 7212	Borus02	XMM–Newton	NuSTAR	$1.94^{+0.49}_{-0.43}$	$1.99^{+0.30}_{-0.22}$	(05)
ESO 406–G004
NGC 7479	Borus02	Swift	NuSTAR	$3.64^{+0.58}_{-0.50}$	$1.83^{+0.09}_{-0.09}$	(05)
SWIFT J2307.9+2245
NGC 7582	Borus02	Swift	NuSTAR	10.0 (fixed)	$1.96^{+0.03}_{-0.05}$	(05)
NGC 7682

NOTE—Column (1): galaxy name. Column (2): applied torus models. For more information, please see the following papers (Ehime torus model: [Ikeda et al. 2009](#), MYTorus model : [Murphy & Yaqoob 2009](#), and Borus02 model: [Baloković et al. 2018](#)). Column (3): Satellite1. Column (4): Satellite2. Column (5): hydrogen column density along the line of sight in units of 10^{24} cm^{-2} . Column (6): photon index. Column (7): reference.

References—(01) [Georgantopoulos & Akylas \(2019\)](#). (02) [Koss et al. \(2016\)](#). (03) [Oda et al. \(2017\)](#). (04) [Marchesi et al. \(2019a\)](#). (05) [Marchesi et al. \(2019b\)](#). (06) [Torres-Albà et al. \(2021\)](#). (07) [Zhao et al. \(2020\)](#).

B. COMPARISON OF BEST-FITTING PARAMETERS WITH PREVIOUS WORKS

[Appendix B](#) compares our best-fitting parameters with those of previous works. To focus on differences in the spectral models, we only refer to previous works that used the NuSTAR observational data.

B.1. Comparison between XClumpy Model and Borus02 Model

[Table 6](#) summarizes the logarithmic hydrogen column density along the line of sight ($\log N_{\text{H}}^{\text{LOS}}/\text{cm}^{-2}$) and the photon index (Γ) of previous works. [Appendix B.1](#) mainly compares $\log N_{\text{H}}^{\text{LOS}}/\text{cm}^{-2}$ and Γ obtained from the XClumpy model with those inferred from the Borus02 model. [Figure 16](#) plots (a) the correlation between $\log N_{\text{H}}^{\text{LOS}}/\text{cm}^{-2}$ obtained from the XClumpy model and those inferred from the Borus02 model and (b) the correlation between Γ obtained from the XClumpy model and those inferred from the Borus02 model. Here we plot 35 objects. We note that in the cases of these studies, $\log N_{\text{H}}^{\text{Equ}}/\text{cm}^{-2}$ is

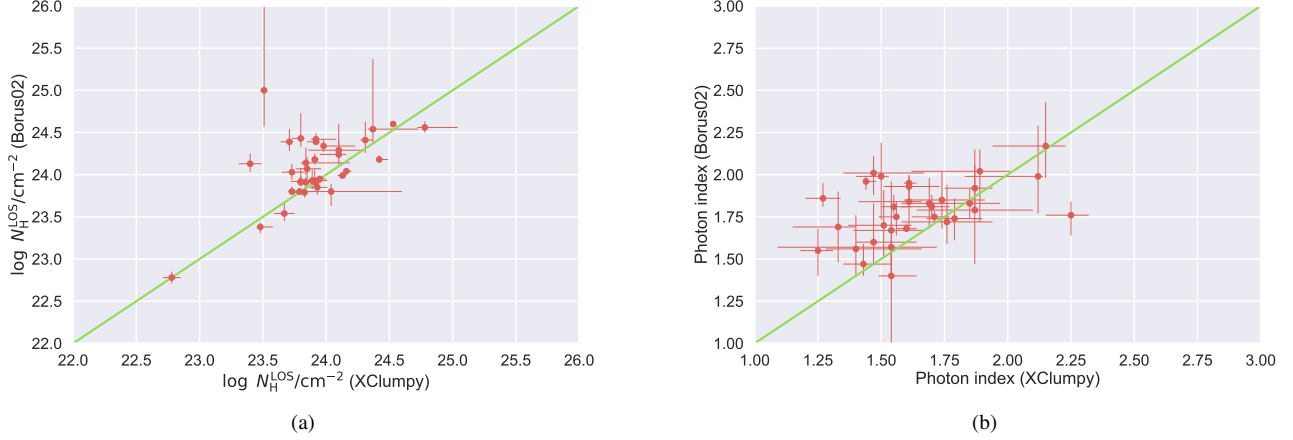


Figure 16. (a) The correlation between the logarithmic hydrogen column density along the line of sight ($\log N_{\text{H}}^{\text{LOS}}/\text{cm}^{-2}$) obtained from the XClumpy model and those inferred from the Borus02 model of previous works. (b) The correlation between the photon index (Γ) obtained from the XClumpy model and those inferred from the Borus02 model of previous works.

different from $\log N_{\text{H}}^{\text{LOS}}/\text{cm}^{-2}$. As a result, $\log N_{\text{H}}^{\text{LOS}}/\text{cm}^{-2}$ obtained from the Borus02 model in their work are different from those inferred from the Borus02 model in this study (Appendix A.2).

Figure 16(a) shows that $\log N_{\text{H}}^{\text{LOS}}/\text{cm}^{-2}$ obtained from the XClumpy model of eight objects are consistent with those inferred from their works within the 90% confidence interval and $\log N_{\text{H}}/\text{cm}^{-2}$ obtained from the XClumpy model of 15 objects are smaller than those inferred from their studies. This is because in the case of the XClumpy model, the flux of Fe K α emission lines and soft reflection continuum is larger than in the Borus02 model. As a result, the XClumpy model can explain the X-ray spectrum even if $\log N_{\text{H}}^{\text{LOS}}/\text{cm}^{-2}$ and $\log N_{\text{H}}^{\text{Equ}}/\text{cm}^{-2}$ are small. In this case, the XClumpy model is expected to have a smaller γ . As we expected, Figure 16(b) shows that Γ obtained from the XClumpy model of 14 objects agree with those inferred from their works within the 90% confidence interval and Γ obtained from the XClumpy model of 11 objects are smaller than those inferred from their studies.

B.2. Individual Object

- ESO 112–G006.** The model with one apec component gives an adequate fit to the X-ray spectra observed with the XMM–Newton and NuSTAR ($\chi_{\text{red}}^2 = 1.21$). We obtain $N_{\text{H}}^{\text{LOS}} = 0.62_{-0.04}^{+0.06} \times 10^{24} \text{ cm}^{-2}$ and $\Gamma = 1.47_{-0.07}^{+0.17}$ with the XClumpy model. The best-fitting parameters of this work are consistent with those of Torres-Albà et al. (2021). Torres-Albà et al. (2021) analyzed the XMM–Newton and NuSTAR observational data, and estimated $N_{\text{H}}^{\text{LOS}} = 0.63_{-0.06}^{+0.04} \times 10^{24} \text{ cm}^{-2}$ and $\Gamma = 1.60_{-0.13}^{+0.23}$ with the Borus02 model.
- MCG –07–03–007.** The model with one apec component provides an adequate fit to the X-ray spectra observed with the XMM–Newton and NuSTAR ($\chi_{\text{red}}^2 = 1.24$). We obtain $N_{\text{H}}^{\text{LOS}} = 0.90_{-0.09}^{+0.11} \times 10^{24} \text{ cm}^{-2}$ and $\Gamma = 1.61_{-0.20}^{+0.05}$ with the XClumpy model. $N_{\text{H}}^{\text{LOS}}$ of this work agrees with that of Torres-Albà et al. (2021), while Γ of this work is smaller than that of Torres-Albà et al. (2021). Torres-Albà et al. (2021) used the XMM–Newton and NuSTAR observational data, and estimated $N_{\text{H}}^{\text{LOS}} = 0.90_{-0.08}^{+0.07} \times 10^{24} \text{ cm}^{-2}$ and $\Gamma = 1.84_{-0.15}^{+0.12}$ with the Borus02 model.
- NGC 0424.** The model with one zgauss component gives an adequate fit to the X-ray spectra observed with the XMM–Newton and NuSTAR ($\chi_{\text{red}}^2 = 1.40$). We obtain $N_{\text{H}}^{\text{LOS}} = 0.84_{-0.07}^{+0.31} \times 10^{24} \text{ cm}^{-2}$ and $\Gamma = 1.70_{-0.12}^{+0.07}$ with the XClumpy model. Γ of this work is consistent with that of Marchesi et al. (2019b), whereas $N_{\text{H}}^{\text{LOS}}$ is smaller than that of Marchesi et al. (2019b). Marchesi et al. (2019b) analyzed the XMM–Newton and NuSTAR observational data, and estimated $N_{\text{H}}^{\text{LOS}} = 2.65_{-0.36}^{+0.44} \times 10^{24} \text{ cm}^{-2}$ and $\Gamma = 1.81_{-0.05}^{+0.07}$ with the Borus02 model. As mentioned in Appendix B.1, such a difference can be attributed to the difference in the reflection continuum between the XClumpy model and Borus02 model.
- MCG +08–03–018.** The model can reproduce the X-ray spectra observed with the Swift/XRT and NuSTAR ($\chi_{\text{red}}^2 = 1.04$). We obtain $N_{\text{H}}^{\text{LOS}} = 0.54_{-0.10}^{+0.13} \times 10^{24} \text{ cm}^{-2}$ and $\Gamma = 2.15_{-0.21}^{+0.08}$ with the XClumpy model. Γ of this work agrees with that of Marchesi et al. (2019b), while $N_{\text{H}}^{\text{LOS}}$ of this work is smaller than Marchesi et al. (2019b). Marchesi

- et al. (2019b) used the Swift/XRT and NuSTAR observational data, and estimated $N_{\text{H}}^{\text{LOS}} = 1.07_{-0.22}^{+0.24} \times 10^{24} \text{ cm}^{-2}$ and $\Gamma = 2.17_{-0.19}^{+0.26}$ with the Borus02 model.
5. **2MASX J01290761–6038423.** We report the XMM–Newton and NuSTAR observational data for the first time. The model with one apec component can replicate the X-ray spectra observed with the XMM–Newton and NuSTAR ($\chi_{\text{red}}^2 = 1.14$). We obtain $N_{\text{H}}^{\text{LOS}} = 0.95_{-0.17}^{+0.09} \times 10^{24} \text{ cm}^{-2}$ and $\Gamma = 1.86_{-0.10}^{+0.22}$ with the XClumpy model.
 6. **ESO 244–IG030.** The model with one apec component well reproduce the X-ray spectra observed with the XMM–Newton and NuSTAR ($\chi_{\text{red}}^2 = 0.94$). We obtain $N_{\text{H}}^{\text{LOS}} = 0.06_{-0.01}^{+0.01} \times 10^{24} \text{ cm}^{-2}$ and $\Gamma = 1.74_{-0.15}^{+0.17}$ with the XClumpy model. $N_{\text{H}}^{\text{LOS}}$ and Γ of this work are consistent with those of Marchesi et al. (2019b). Marchesi et al. (2019a) analyzed the XMM–Newton and NuSTAR observational data, and estimated $N_{\text{H}}^{\text{LOS}} = 0.06_{-0.01}^{+0.01} \times 10^{24} \text{ cm}^{-2}$ and $\Gamma = 1.85_{-0.17}^{+0.17}$ with the Borus02 model.
 7. **NGC 1106.** We report the XMM–Newton and NuSTAR observational data for the first time. The model with one apec component can reproduce the X-ray spectra observed with the XMM–Newton and NuSTAR ($\chi_{\text{red}}^2 = 1.15$). We obtain $N_{\text{H}}^{\text{LOS}} = 3.77_{-0.32}^{+0.52} \times 10^{24} \text{ cm}^{-2}$ and $\Gamma = 1.67_{-0.30}^{+0.16}$ with the XClumpy model.
 8. **2MFGC 02280.** The model well replicate the X-ray spectra observed with the Swift/XRT and NuSTAR ($\chi_{\text{red}}^2 = 0.96$). We obtain $N_{\text{H}}^{\text{LOS}} = 2.03_{-0.20}^{+2.17} \times 10^{24} \text{ cm}^{-2}$ and $\Gamma = 1.71_{-0.39}^{+0.18}$ with the XClumpy model. $N_{\text{H}}^{\text{LOS}}$ of this work agrees with that of Koss et al. (2016), whereas Γ of this work is smaller than that of Koss et al. (2016). Koss et al. (2016) used the Swift/XRT and NuSTAR observational data, and estimated $N_{\text{H}}^{\text{LOS}} = 3.16_{-0.30}^{+0.35} \times 10^{24} \text{ cm}^{-2}$ and $\Gamma = 2.10_{-0.10}^{+0.10}$ with the MYTorus model.
 9. **NGC 1125.** We report the NuSTAR observational data for the first time. The model can reproduce the X-ray spectra observed with the Chandra and NuSTAR ($\chi_{\text{red}}^2 = 1.16$). We obtain $N_{\text{H}}^{\text{LOS}} = 1.16_{-0.50}^{+0.92} \times 10^{24} \text{ cm}^{-2}$ and $\Gamma = 1.82_{-0.24}^{+0.11}$ with the XClumpy model.
 10. **NGC 1194.** The model can replicate the X-ray spectra observed with the Suzaku and NuSTAR ($\chi_{\text{red}}^2 = 1.20$). We obtain $N_{\text{H}}^{\text{LOS}} = 0.83_{-0.13}^{+0.06} \times 10^{24} \text{ cm}^{-2}$ and $\Gamma = 1.27_{-0.07}^{+0.07}$. $N_{\text{H}}^{\text{LOS}}$ and Γ of this work are smaller than those of Marchesi et al. (2019b). Marchesi et al. (2019b) analyzed the XMM–Newton and NuSTAR observational data, and estimated $N_{\text{H}}^{\text{LOS}} = 2.47_{-0.08}^{+0.41} \times 10^{24} \text{ cm}^{-2}$ and $\Gamma = 1.86_{-0.05}^{+0.09}$ with the Borus02 model.
 11. **NGC 1229.** The model provides an adequate fit to the X-ray spectra observed with the Swift/XRT and NuSTAR ($\chi_{\text{red}}^2 = 1.23$). We obtain $N_{\text{H}}^{\text{LOS}} = 0.47_{-0.09}^{+0.26} \times 10^{24} \text{ cm}^{-2}$ and $\Gamma = 1.54_{-0.45}^{+0.18}$ with the XClumpy model. $N_{\text{H}}^{\text{LOS}}$ and Γ of this work agree with those of Marchesi et al. (2019b). Marchesi et al. (2019b) used the Swift/XRT and NuSTAR observational data, and estimated $N_{\text{H}}^{\text{LOS}} = 0.35_{-0.07}^{+0.10} \times 10^{24} \text{ cm}^{-2}$ and $\Gamma = 1.57_{-0.16}^{+0.14}$ with the Borus02 model.
 12. **ESO 201–IG004.** The model gives an adequate fit to the X-ray spectra observed with the Suzaku and NuSTAR ($\chi_{\text{red}}^2 = 1.31$). We obtain $N_{\text{H}}^{\text{LOS}} = 0.25_{-0.05}^{+0.31} \times 10^{24} \text{ cm}^{-2}$ and $\Gamma = 1.33_{-0.18}^{+0.07}$ with the XClumpy model. $N_{\text{H}}^{\text{LOS}}$ and Γ are smaller than those of Marchesi et al. (2019b). Marchesi et al. (2019b) analyzed the XMM–Newton and NuSTAR observational data, and estimated $N_{\text{H}}^{\text{LOS}} = 1.34_{-0.32}^{+0.36} \times 10^{24} \text{ cm}^{-2}$ and $\Gamma = 1.69_{-0.21}^{+0.21}$ with the Borus02 model.
 13. **2MASX J03561995–6251391.** The model with one apec component can reproduce the X-ray spectra observed with the XMM–Newton and NuSTAR ($\chi_{\text{red}}^2 = 1.12$). We obtain $N_{\text{H}}^{\text{LOS}} = 0.63_{-0.12}^{+0.08} \times 10^{24} \text{ cm}^{-2}$ and $\Gamma = 1.50_{-0.10}^{+0.03}$ with the XClumpy model. $N_{\text{H}}^{\text{LOS}}$ and Γ of this work are smaller those of Marchesi et al. (2019b). Marchesi et al. (2019b) used the Swift/XRT and NuSTAR observational data, and estimated $N_{\text{H}}^{\text{LOS}} = 0.84_{-0.11}^{+0.11} \times 10^{24} \text{ cm}^{-2}$ and $\Gamma = 1.99_{-0.26}^{+0.20}$ with the Borus02 model.
 14. **MCG –02–12–017.** We report the XMM–Newton and NuSTAR data for the first time. The model with one apec component can replicate the X-ray spectra observed with the XMM–Newton and NuSTAR ($\chi_{\text{red}}^2 = 1.07$). We obtain $N_{\text{H}}^{\text{LOS}} = 0.24_{-0.03}^{+0.04} \times 10^{24} \text{ cm}^{-2}$ and $\Gamma = 1.79_{-0.26}^{+0.09}$ with the XClumpy model.
 15. **CGCG 420–015.** The model with one apec component gives an adequate fit to the X-ray spectra observed with the XMM–Newton and NuSTAR ($\chi_{\text{red}}^2 = 1.22$). We obtain $N_{\text{H}}^{\text{LOS}} = 0.81_{-0.04}^{+0.06} \times 10^{24} \text{ cm}^{-2}$ and $\Gamma = 1.87_{-0.12}^{+0.07}$ with the XClumpy model. Γ of this work are consistent with that of Marchesi et al. (2019b), while $N_{\text{H}}^{\text{LOS}}$ of this work is smaller than that of Marchesi et al. (2019b). Marchesi et al. (2019b) analyzed the XMM–Newton and NuSTAR observational data, and estimated $N_{\text{H}}^{\text{LOS}} = 1.50_{-0.22}^{+0.25} \times 10^{24} \text{ cm}^{-2}$ and $\Gamma = 1.92_{-0.13}^{+0.14}$.

16. **ESO 005–G004.** The model with one zgauss component provides an adequate fit to the X-ray spectra observed with the Suzaku and NuSTAR ($\chi_{\text{red}}^2 = 1.25$). We $N_{\text{H}}^{\text{LOS}} = 0.51_{-0.08}^{+0.04} \times 10^{24} \text{ cm}^{-2}$ and $\Gamma = 1.43_{-0.08}^{+0.11}$ with the XClumpy model. Γ of this work agrees with that of [Marchesi et al. \(2019b\)](#), whereas $N_{\text{H}}^{\text{LOS}}$ is smaller than that of [Marchesi et al. \(2019b\)](#). [Marchesi et al. \(2019b\)](#) used the Swift/XRT and NuSTAR observational data, and estimated $N_{\text{H}}^{\text{LOS}} = 2.48_{-0.62}^{+0.86} \times 10^{24} \text{ cm}^{-2}$ and $\Gamma = 1.47_{-0.07}^{+0.12}$ with the Borus02 model. This is because of the difference in the quality of the data in the soft X-ray band. The Suzaku/XIS has a larger effective area than that of the Swift/XRT. The scattered fraction we obtain, $f_{\text{scat}} = 1.93_{-0.59}^{+1.16}$, is larger than those found in the previous studies based on the Suzaku and Swift/BAT first 9–month data ([Ueda et al. 2007](#); [Eguchi et al. 2009](#)). The main reason for the difference is that the photon index, which is constrained mainly with the NuSTAR data in our analysis, is much smaller than the previous estimates ($\Gamma \simeq 2.0$). This may be related to the large flux variability between the Suzaku and NuSTAR observations ([Table 3](#)).
17. **Mrk 0003.** The model can replicate the X-ray spectra observed with the XMM–Newton and NuSTAR ($\chi_{\text{red}}^2 = 1.18$). We fixed i at 87° because the maser has been detected in this object. We obtain $N_{\text{H}}^{\text{LOS}} = 0.84_{-0.06}^{+0.02} \times 10^{24} \text{ cm}^{-2}$ and $\Gamma = 1.60_{-0.04}^{+0.04}$ with the XClumpy model. $N_{\text{H}}^{\text{LOS}}$ of this work is consistent with that of [Marchesi et al. \(2019b\)](#), while Γ of this work is smaller than that of [Marchesi et al. \(2019b\)](#). [Marchesi et al. \(2019b\)](#) analyzed the XMM–Newton and NuSTAR observational data, and estimated $N_{\text{H}}^{\text{LOS}} = 0.80_{-0.02}^{+0.03} \times 10^{24} \text{ cm}^{-2}$ and $\Gamma = 1.68_{-0.02}^{+0.03}$ with the Borus02 model.
18. **2MASX J06561197–4919499.** We report the XMM–Newton and NuSTAR observational data for the first time. The model with one apec component can reproduce the X-ray spectra observed with the XMM–Newton and NuSTAR ($\chi_{\text{red}}^2 = 1.06$). We obtain $N_{\text{H}}^{\text{LOS}} = 0.97_{-0.17}^{+0.17} \times 10^{24} \text{ cm}^{-2}$ and $\Gamma = 1.58_{-0.22}^{+0.04}$ with the XClumpy model.
19. **MCG +06–16–028.** The model with one apec component gives an adequate fit to the X-ray spectra observed with the Suzaku and NuSTAR ($\chi_{\text{red}}^2 = 1.30$). We obtain $N_{\text{H}}^{\text{LOS}} = 0.69_{-0.04}^{+0.19} \times 10^{24} \text{ cm}^{-2}$ and $\Gamma = 1.69_{-0.11}^{+0.07}$ with the XClumpy model. $N_{\text{H}}^{\text{LOS}}$ and Γ of this work agree with those of [Marchesi et al. \(2019b\)](#). [Marchesi et al. \(2019b\)](#) used the Swift/XRT and NuSTAR observational data, and estimated $N_{\text{H}}^{\text{LOS}} = 0.82_{-0.11}^{+0.11} \times 10^{24} \text{ cm}^{-2}$ and $\Gamma = 1.83_{-0.15}^{+0.15}$ with the Borus02 model.
20. **Mrk 0078.** The model with one apec component well replicates the X-ray spectra observed with the XMM–Newton and NuSTAR ($\chi_{\text{red}}^2 = 0.97$). We obtain $N_{\text{H}}^{\text{LOS}} = 0.63_{-0.04}^{+0.11} \times 10^{24} \text{ cm}^{-2}$ and $\Gamma = 1.54_{-0.05}^{+0.10}$ with the XClumpy model. Γ of this work is consistent with that of [Zhao et al. \(2020\)](#), whereas $N_{\text{H}}^{\text{LOS}}$ of this work is smaller than that of [Zhao et al. \(2020\)](#). [Zhao et al. \(2020\)](#) analyzed the XMM–Newton and NuSTAR observational data, and estimated $N_{\text{H}}^{\text{LOS}} = 0.81_{-0.04}^{+0.19} \times 10^{24} \text{ cm}^{-2}$ and $\Gamma = 1.40_{-0.21}^{+0.21}$ with the Borus02 model.
21. **Mrk 0622.** The model with one apec component well reproduces the X-ray spectra observed with the XMM–Newton and NuSTAR ($\chi_{\text{red}}^2 = 0.84$). We obtain $N_{\text{H}}^{\text{LOS}} = 0.30_{-0.02}^{+0.07} \times 10^{24} \text{ cm}^{-2}$ and $\Gamma = 1.79_{-0.11}^{+0.11}$ with the XClumpy model. $N_{\text{H}}^{\text{LOS}}$ and Γ of this work agree with those of [Torres-Albà et al. \(2021\)](#). [Torres-Albà et al. \(2021\)](#) used the XMM–Newton and NuSTAR observational data, and estimated $N_{\text{H}}^{\text{LOS}} = 0.24_{-0.04}^{+0.03} \times 10^{24} \text{ cm}^{-2}$ and $\Gamma = 1.74_{-0.13}^{+0.12}$ with the Borus02 model.
22. **NGC 2788A.** We report the NuSTAR observational data for the first time. The model can replicate the X-ray spectra observed with the Suzaku and NuSTAR ($\chi_{\text{red}}^2 = 1.03$). We obtain $N_{\text{H}}^{\text{LOS}} = 2.31_{-0.76}^{+0.52} \times 10^{24} \text{ cm}^{-2}$ and $\Gamma = 1.67_{-0.08}^{+0.11}$ with the XClumpy model.
23. **SBS 0915+556.** We report the NuSTAR observational data for the first time. The model provides an adequate fit to the X-ray spectra observed with the Swift/XRT and NuSTAR ($\chi_{\text{red}}^2 = 1.33$). We obtain $N_{\text{H}}^{\text{LOS}} = 0.09_{-0.02}^{+0.03} \times 10^{24} \text{ cm}^{-2}$ and $\Gamma = 2.02_{-0.02}^{+0.02}$ with the XClumpy model.
24. **2MASX J09235371–3141305.** The model reproduces the X-ray spectra observed with the Swift/XRT and NuSTAR ($\chi_{\text{red}}^2 = 1.05$). We obtain $N_{\text{H}}^{\text{LOS}} = 0.54_{-0.04}^{+0.22} \times 10^{24} \text{ cm}^{-2}$ and $\Gamma = 1.47_{-0.12}^{+0.20}$ with the XClumpy model. $N_{\text{H}}^{\text{LOS}}$ of this work is consistent with that of [Marchesi et al. \(2019b\)](#), while Γ is smaller than that of [Marchesi et al. \(2019b\)](#). [Marchesi et al. \(2019b\)](#) analyzed the Swift/XRT and NuSTAR observational data, and estimated $N_{\text{H}}^{\text{LOS}} = 0.63_{-0.06}^{+0.09} \times 10^{24} \text{ cm}^{-2}$ and $\Gamma = 2.01_{-0.13}^{+0.10}$ with the Borus02 model.
25. **ESO 565–G019.** We report the XMM–Newton and NuSTAR observational data for the first time. The model with one zgauss component can replicate the X-ray spectra observed with the XMM–Newton and NuSTAR ($\chi_{\text{red}}^2 = 1.20$). We obtain $N_{\text{H}}^{\text{LOS}} = 1.12_{-0.05}^{+0.20} \times 10^{24} \text{ cm}^{-2}$ and $\Gamma = 1.09_{-0.08}^{+0.03}$ with the XClumpy model.

26. **MCG +10-14-025.** The model can reproduce the X-ray spectra observed with the Suzaku and NuSTAR ($\chi_{\text{red}}^2 = 1.07$). We obtain $N_{\text{H}}^{\text{LOS}} = 1.53_{-0.09}^{+0.53} \times 10^{24} \text{ cm}^{-2}$ and $\Gamma = 1.58_{-0.32}^{+0.27}$ with the XClumpy model. $N_{\text{H}}^{\text{LOS}}$ and Γ of this work agree those of [Oda et al. \(2017\)](#). [Oda et al. \(2017\)](#) used the XMM-Newton, Suzaku, and NuSTAR observational data, and estimated $N_{\text{H}}^{\text{LOS}} = 1.31_{-0.36}^{+0.31} \times 10^{24} \text{ cm}^{-2}$ and $\Gamma = 1.63_{-0.13}^{+0.27}$ with the Ikeda model.
27. **NGC 3079.** The model can replicate the X-ray spectra observed with the XMM-Newton and NuSTAR ($\chi_{\text{red}}^2 = 1.16$). We fixed i at 87° since the maser has been detected in this object. We obtain $N_{\text{H}}^{\text{LOS}} = 2.65_{-0.13}^{+0.40} \times 10^{24} \text{ cm}^{-2}$ and $\Gamma = 1.61_{-0.10}^{+0.12}$ with the XClumpy model. $N_{\text{H}}^{\text{LOS}}$ of this work is larger than that of [Marchesi et al. \(2019b\)](#) and Γ of this work is smaller than that of [Marchesi et al. \(2019b\)](#). [Marchesi et al. \(2019b\)](#) analyzed the XMM-Newton and NuSTAR observational data, and estimated $N_{\text{H}}^{\text{LOS}} = 1.51_{-0.09}^{+0.19} \times 10^{24} \text{ cm}^{-2}$ and $\Gamma = 1.93_{-0.10}^{+0.06}$ with the Borus02 model. The reason is that $N_{\text{H}}^{\text{LOS}}$ and Γ are degenerated.
28. **ESO 317-G041.** The model with one apec component gives an adequate fit to the X-ray spectra observed with the XMM-Newton and NuSTAR ($\chi_{\text{red}}^2 = 1.32$). We obtain $N_{\text{H}}^{\text{LOS}} = 0.85_{-0.12}^{+0.16} \times 10^{24} \text{ cm}^{-2}$ and $\Gamma = 1.40_{-0.12}^{+0.26}$ with the XClumpy model. $N_{\text{H}}^{\text{LOS}}$ and Γ of this work is consistent with those of [Marchesi et al. \(2019a\)](#). [Marchesi et al. \(2019a\)](#) used the XMM-Newton and NuSTAR observational data, and estimated $N_{\text{H}}^{\text{LOS}} = 0.71_{-0.15}^{+0.14} \times 10^{24} \text{ cm}^{-2}$ and $\Gamma = 1.56_{-0.16}^{+0.20}$ with the Borus02 model.
29. **SDSS J103315.71+525217.8.** The model can reproduce the X-ray spectra observed with the XMM-Newton and NuSTAR ($\chi_{\text{red}}^2 = 1.15$). We obtain $N_{\text{H}}^{\text{LOS}} = 0.71_{-0.12}^{+0.16} \times 10^{24} \text{ cm}^{-2}$ and $\Gamma = 1.55_{-0.18}^{+0.25}$ with the XClumpy model. $N_{\text{H}}^{\text{LOS}}$ and Γ of this work agree with those of [Marchesi et al. \(2019a\)](#). [Marchesi et al. \(2019a\)](#) analyzed the XMM-Newton and NuSTAR observational data, and estimated $N_{\text{H}}^{\text{LOS}} = 1.17_{-0.32}^{+0.38} \times 10^{24} \text{ cm}^{-2}$ and $\Gamma = 1.40$ (fixed) with the Borus02 model.
30. **NGC 3393.** The model can replicate the X-ray spectra observed with the XMM-Newton and NuSTAR ($\chi_{\text{red}}^2 = 1.14$). We fixed i at 87° because the maser has been detected in this object. We obtain $N_{\text{H}}^{\text{LOS}} = 2.05_{-0.21}^{+0.30} \times 10^{24} \text{ cm}^{-2}$ and $\Gamma = 1.76_{-0.18}^{+0.18}$ with the XClumpy model. $N_{\text{H}}^{\text{LOS}}$ and Γ of this work agree with those of [Marchesi et al. \(2019b\)](#). [Marchesi et al. \(2019b\)](#) used the XMM-Newton and NuSTAR observational data, and estimated $N_{\text{H}}^{\text{LOS}} = 2.58_{-0.87}^{+1.32} \times 10^{24} \text{ cm}^{-2}$ and $\Gamma = 1.72_{-0.13}^{+0.22}$ with the Borus02 model.
31. **NGC 4102.** The model with one apec component can reproduce the X-ray spectra observed with the XMM-Newton and NuSTAR ($\chi_{\text{red}}^2 = 1.12$). We obtain $N_{\text{H}}^{\text{LOS}} = 0.67_{-0.14}^{+0.02} \times 10^{24} \text{ cm}^{-2}$ and $\Gamma = 1.56_{-0.07}^{+0.01}$ with the XClumpy. $N_{\text{H}}^{\text{LOS}}$ of this work is consistent with that of [Marchesi et al. \(2019b\)](#), whereas Γ of this work is smaller than that of [Marchesi et al. \(2019b\)](#). [Marchesi et al. \(2019b\)](#) analyzed the XMM-Newton and NuSTAR observational data, and estimated $N_{\text{H}}^{\text{LOS}} = 0.62_{-0.08}^{+0.09} \times 10^{24} \text{ cm}^{-2}$ and $\Gamma = 1.75_{-0.11}^{+0.09}$ with the Borus02 model.
32. **NGC 4180.** We report the NuSTAR observational data for the first time. The model well replicates the X-ray spectra observed with the Chandra and NuSTAR ($\chi_{\text{red}}^2 = 0.80$). We obtain $N_{\text{H}}^{\text{LOS}} = 1.84_{-1.16}^{+1.91} \times 10^{24} \text{ cm}^{-2}$ and $\Gamma = 1.61_{-0.17}^{+0.05}$ with the XClumpy model.
33. **ESO 323-G032.** The model with one apec component well reproduces the X-ray spectra observed with the XMM-Newton and NuSTAR ($\chi_{\text{red}}^2 = 0.77$). We obtain $N_{\text{H}}^{\text{LOS}} = 1.27_{-0.45}^{+0.17} \times 10^{24} \text{ cm}^{-2}$ and $\Gamma = 1.89_{-0.27}^{+0.12}$ with the XClumpy model. $N_{\text{H}}^{\text{LOS}}$ and Γ of this work agree with those of [Torres-Albà et al. \(2021\)](#). [Torres-Albà et al. \(2021\)](#) used the XMM-Newton and NuSTAR observational data, and estimated $N_{\text{H}}^{\text{LOS}} = 1.75_{-0.49}^{+1.46} \times 10^{24} \text{ cm}^{-2}$ and $\Gamma = 2.02_{-0.30}^{+0.13}$ with the Borus02 model.
34. **NGC 4945.** The model with one zgauss component provides an adequate fit to the X-ray spectra observed with the Suzaku and NuSTAR ($\chi_{\text{red}}^2 = 1.21$). We fixed i at 87° since the maser has been detected in this object. We obtain $N_{\text{H}}^{\text{LOS}} = 3.40_{-0.08}^{+0.11} \times 10^{24} \text{ cm}^{-2}$ and $\Gamma = 1.61_{-0.02}^{+0.03}$ with the XClumpy model. $N_{\text{H}}^{\text{LOS}}$ and Γ of this work are smaller than those of [Marchesi et al. \(2019a\)](#). [Marchesi et al. \(2019b\)](#) analyzed the XMM-Newton and NuSTAR observational data, and estimated $N_{\text{H}}^{\text{LOS}} = 3.97_{-0.15}^{+0.15} \times 10^{24} \text{ cm}^{-2}$ and $\Gamma = 1.95_{-0.05}^{+0.05}$ with the Borus02 model.
35. **IGR J14175-4641.** The model gives an adequate fit to the X-ray spectra observed with the XMM-Newton and NuSTAR ($\chi_{\text{red}}^2 = 1.22$). We obtain $N_{\text{H}}^{\text{LOS}} = 0.77_{-0.13}^{+0.08} \times 10^{24} \text{ cm}^{-2}$ and $\Gamma = 1.51_{-0.14}^{+0.11}$ with the XClumpy model. $N_{\text{H}}^{\text{LOS}}$ and Γ of this work agree with those of [Marchesi et al. \(2019b\)](#). [Marchesi et al. \(2019b\)](#) used the Swift/XRT and NuSTAR observational data, and obtained $N_{\text{H}}^{\text{LOS}} = 0.86_{-0.19}^{+0.25} \times 10^{24} \text{ cm}^{-2}$ and $\Gamma = 1.70_{-0.19}^{+0.20}$ with the Borus02 model.

36. **NGC 5643.** The model with two zgauss components provides an adequate fit to the X-ray spectra observed with the XMM–Newton and NuSTAR ($\chi_{\text{red}}^2 = 1.35$). We fixed i at 87° because the maser has been detected in this object. We obtain $N_{\text{H}}^{\text{LOS}} = 0.63_{-0.10}^{+0.05} \times 10^{24} \text{ cm}^{-2}$ and $\Gamma = 1.25_{-0.07}^{+0.06}$ with the XClumpy model. $N_{\text{H}}^{\text{LOS}}$ and Γ of this work are smaller than those of [Marchesi et al. \(2019b\)](#). [Marchesi et al. \(2019b\)](#) analyzed the XMM–Newton and NuSTAR observational data, and estimated $N_{\text{H}}^{\text{LOS}} = 2.69_{-0.65}^{+1.88} \times 10^{24} \text{ cm}^{-2}$ and $\Gamma = 1.55_{-0.15}^{+0.13}$ with the Borus02 model.
37. **NGC 5728.** The model with one apec component well replicates the X-ray spectra observed with the XMM–Newton and NuSTAR ($\chi_{\text{red}}^2 = 0.99$). We fixed i at 87° since the maser has been detected in this object. We obtain $N_{\text{H}}^{\text{LOS}} = 1.36_{-0.11}^{+0.08} \times 10^{24} \text{ cm}^{-2}$ and $\Gamma = 1.55_{-0.05}^{+0.07}$ with the XClumpy model. $N_{\text{H}}^{\text{LOS}}$ of this work is larger than that of [Marchesi et al. \(2019b\)](#) and Γ of this work is smaller than that of [Marchesi et al. \(2019b\)](#). [Marchesi et al. \(2019b\)](#) used the Chandra and NuSTAR observational data, and obtained $N_{\text{H}}^{\text{LOS}} = 0.97_{-0.03}^{+0.05} \times 10^{24} \text{ cm}^{-2}$ and $\Gamma = 1.81_{-0.04}^{+0.07}$ with the Borus02 model.
38. **CGCG 164–019.** The model provides an adequate fit to the X-ray spectra observed with the Swift/XRT and NuSTAR ($\chi_{\text{red}}^2 = 1.29$). We obtain $N_{\text{H}}^{\text{LOS}} = 0.69_{-0.06}^{+0.55} \times 10^{24} \text{ cm}^{-2}$ and $\Gamma = 1.87_{-0.23}^{+0.23}$ with the XClumpy model. $N_{\text{H}}^{\text{LOS}}$ and Γ of this work are consistent with those of [Marchesi et al. \(2019b\)](#). [Marchesi et al. \(2019b\)](#) analyzed the Swift/XRT and NuSTAR observational data, and estimated $N_{\text{H}}^{\text{LOS}} = 1.37_{-0.45}^{+0.57} \times 10^{24} \text{ cm}^{-2}$ and $\Gamma = 1.79_{-0.32}^{+0.36}$ with the Borus02 model.
39. **ESO 137–G034.** The model with one apec component can reproduce the X-ray spectra observed with the XMM–Newton and NuSTAR ($\chi_{\text{red}}^2 = 1.13$). We obtain $N_{\text{H}}^{\text{LOS}} = 2.87_{-0.20}^{+0.20} \times 10^{24} \text{ cm}^{-2}$ and $\Gamma = 1.85_{-0.11}^{+0.09}$ with the XClumpy model. $N_{\text{H}}^{\text{LOS}}$ of this work agrees with that of [Georgantopoulos & Akylas \(2019\)](#). [Georgantopoulos & Akylas \(2019\)](#) used the NuSTAR data, and estimated $N_{\text{H}}^{\text{LOS}} = 2.90_{-0.54}^{+0.86} \times 10^{24} \text{ cm}^{-2}$ with the MYTorus model.
40. **NGC 6232.** The model can replicate the X-ray spectra observed with the Swift and NuSTAR ($\chi_{\text{red}}^2 = 1.13$). We obtain $N_{\text{H}}^{\text{LOS}} = 1.10_{-0.59}^{+1.43} \times 10^{24} \text{ cm}^{-2}$ and $\Gamma = 1.31_{-0.14}^{+0.57}$ with the XClumpy model. $N_{\text{H}}^{\text{LOS}}$ and Γ of this work are consistent with those of [Marchesi et al. \(2019b\)](#). [Marchesi et al. \(2019b\)](#) analyzed the Swift/XRT and NuSTAR observational data, and estimated $N_{\text{H}}^{\text{LOS}} = 0.63_{-0.24}^{+0.13} \times 10^{24} \text{ cm}^{-2}$ and $\Gamma = 1.40$ (fixed) with the Borus02 model.
41. **ESO 138–G001.** We report the NuSTAR observational data for the first time. The model with one zgauss component provides an adequate fit to the X-ray spectra observed with the XMM–Newton and NuSTAR ($\chi_{\text{red}}^2 = 1.39$). We obtain $N_{\text{H}}^{\text{LOS}} = 0.45_{-0.03}^{+0.05} \times 10^{24} \text{ cm}^{-2}$ and $\Gamma = 1.45_{-0.03}^{+0.06}$ with the XClumpy model.
42. **NGC 6240.** The model with one zgauss component can reproduce the X-ray spectra observed with the XMM–Newton and NuSTAR ($\chi_{\text{red}}^2 = 1.07$). We fixed i at $^\circ$ because the maser has been detected in this object. We obtain $N_{\text{H}}^{\text{LOS}} = 1.45_{-0.05}^{+0.15} \times 10^{24} \text{ cm}^{-2}$ and $\Gamma = 1.71_{-0.09}^{+0.06}$ with the XClumpy model. Γ of this work agrees with that of [Marchesi et al. \(2019b\)](#), while $N_{\text{H}}^{\text{LOS}}$ of this work is larger than that of [Marchesi et al. \(2019b\)](#). [Marchesi et al. \(2019b\)](#) used the XMM–Newton and NuSTAR observational data, and estimated $N_{\text{H}}^{\text{LOS}} = 1.10_{-0.08}^{+0.10} \times 10^{24} \text{ cm}^{-2}$ and $\Gamma = 1.75_{-0.04}^{+0.03}$ with the Borus02 model.
43. **NGC 6552.** The model with one apec component gives an adequate fit to the X-ray spectra observed with the XMM–Newton and NuSTAR ($\chi_{\text{red}}^2 = 1.29$). We obtain $N_{\text{H}}^{\text{LOS}} = 0.96_{-0.05}^{+0.55} \times 10^{24} \text{ cm}^{-2}$ and $\Gamma = 2.25_{-0.10}^{+0.07}$ with the XClumpy model. $N_{\text{H}}^{\text{LOS}}$ of this work is smaller than that of [Torres-Albà et al. \(2021\)](#) and Γ of this work is larger than that of [Torres-Albà et al. \(2021\)](#). [Torres-Albà et al. \(2021\)](#) analyzed the XMM–Newton and NuSTAR observational data, and estimated $N_{\text{H}}^{\text{LOS}} = 2.18_{-0.35}^{+0.38} \times 10^{24} \text{ cm}^{-2}$ and $\Gamma = 1.76_{-0.12}^{+0.08}$ with the Borus02 model.
44. **2MASX J20145928+2523010.** We report the NuSTAR data for the first time. The model can replicate the X-ray spectra observed with the XMM–Newton and NuSTAR ($\chi_{\text{red}}^2 = 1.18$). We obtain $N_{\text{H}}^{\text{LOS}} = 0.02_{-0.01}^{+0.01} \times 10^{24} \text{ cm}^{-2}$ and $\Gamma = 1.42_{-0.09}^{+0.03}$ with the XClumpy model.
45. **ESO 464–G016.** The model with one apec component well reproduces the X-ray spectra observed with the XMM–Newton and NuSTAR ($\chi_{\text{red}}^2 = 0.97$). We obtain $N_{\text{H}}^{\text{LOS}} = 0.82_{-0.10}^{+0.19} \times 10^{24} \text{ cm}^{-2}$ and $\Gamma = 1.54_{-0.15}^{+0.13}$. $N_{\text{H}}^{\text{LOS}}$ and Γ of this work are consistent with those of [Marchesi et al. \(2019b\)](#). [Marchesi et al. \(2019b\)](#) used the XMM–Newton and NuSTAR observational data, and estimated $N_{\text{H}}^{\text{LOS}} = 0.86_{-0.17}^{+0.25} \times 10^{24} \text{ cm}^{-2}$ and $\Gamma = 1.67_{-0.27}^{+0.29}$ with the Borus02 model.
46. **NGC 7130.** The model with one apec component can replicate the X-ray spectra observed with the Suzaku and NuSTAR ($\chi_{\text{red}}^2 = 1.03$). We obtain $N_{\text{H}}^{\text{LOS}} = 2.32_{-0.24}^{+1.95} \times 10^{24} \text{ cm}^{-2}$ and $\Gamma = 1.59_{-0.24}^{+0.09}$ with the XClumpy model. $N_{\text{H}}^{\text{LOS}}$ and

Γ of this work agree with those of [Marchesi et al. \(2019b\)](#). [Marchesi et al. \(2019b\)](#) analyzed the Chandra and NuSTAR observational data, and obtained $N_{\text{H}}^{\text{LOS}} = 3.43_{-1.26}^{+6.57} \times 10^{24} \text{ cm}^{-2}$ and $\Gamma = 1.40$ (fixed) with the Borus02 model.

47. **NGC 7212.** The model provides an adequate fit to the X-ray spectra observed with the XMM–Newton and NuSTAR ($\chi_{\text{red}}^2 = 1.38$). We obtain $N_{\text{H}}^{\text{LOS}} = 1.27_{-0.69}^{+0.54} \times 10^{24} \text{ cm}^{-2}$ and $\Gamma = 2.12_{-0.29}^{+0.02}$. $N_{\text{H}}^{\text{LOS}}$ and Γ of this work are consistent with those of [Marchesi et al. \(2019b\)](#). [Marchesi et al. \(2019b\)](#) used the XMM–Newton and NuSTAR observational data, and estimated $N_{\text{H}}^{\text{LOS}} = 1.94_{-0.43}^{+0.49} \times 10^{24} \text{ cm}^{-2}$ and $\Gamma = 1.99_{-0.22}^{+0.30}$ with the Borus02 model.
48. **ESO 406–G004.** We report the NuSTAR data for the first time. The model gives an adequate fit to the X-ray spectra observed with the Swift/XRT and NuSTAR ($\chi_{\text{red}}^2 = 1.33$). We obtain $N_{\text{H}}^{\text{LOS}} = 0.52_{-0.14}^{+5.82} \times 10^{24} \text{ cm}^{-2}$ and $\Gamma = 1.10^{+0.28}$ with the XClumpy model.
49. **NGC 7479.** The model provides an adequate fit to the X-ray spectra observed with the XMM–Newton and NuSTAR ($\chi_{\text{red}}^2 = 1.21$). We fixed i at 87° since the maser has been detected in this object. We obtain $N_{\text{H}}^{\text{LOS}} = 6.07_{-0.80}^{+3.61} \times 10^{24} \text{ cm}^{-2}$ and $\Gamma = 1.85_{-0.16}^{+0.12}$ with the XClumpy model. Γ of this work agrees with that of [Marchesi et al. \(2019a\)](#), whereas $N_{\text{H}}^{\text{LOS}}$ is larger than that of [Marchesi et al. \(2019a\)](#). [Marchesi et al. \(2019a\)](#) analyzed the Swift/XRT and NuSTAR observational data, and estimated $N_{\text{H}}^{\text{LOS}} = 1.32_{-0.28}^{+0.24} \times 10^{24} \text{ cm}^{-2}$ and $\Gamma = 1.64_{-0.19}^{+0.14}$ with the Borus02 model.
50. **SWIFT J2307.9+2245.** We report the XMM–Newton and NuSTAR simultaneous observational data for the first time. The model well reproduces the X-ray spectra observed with the XMM–Newton and NuSTAR ($\chi_{\text{red}}^2 = 0.98$). We obtain $N_{\text{H}}^{\text{LOS}} = 1.62_{-0.74}^{+1.26} \times 10^{24} \text{ cm}^{-2}$ and $\Gamma = 1.86_{-0.35}^{+0.03}$ with the XClumpy model.
51. **NGC 7582.** The model with one zgauss component provides an adequate fit to the X-ray spectra observed with the XMM–Newton and NuSTAR ($\chi_{\text{red}}^2 = 1.33$). We obtain $N_{\text{H}}^{\text{LOS}} = 0.32_{-0.02}^{+0.01} \times 10^{24} \text{ cm}^{-2}$ and $\Gamma = 1.44_{-0.01}^{+0.04}$ with the XClumpy model. Γ of this work is smaller than that of [Marchesi et al. \(2019b\)](#). [Marchesi et al. \(2019b\)](#) used the Swift/XRT and NuSTAR observational data, and estimated $N_{\text{H}}^{\text{LOS}} = 10.0 \times 10^{24} \text{ cm}^{-2}$ (fixed) and $\Gamma = 1.96_{-0.05}^{+0.03}$. This is because of the time variability of the object. In fact, [Picconcelli et al. \(2007\)](#) analyzed the multi period XMM–Newton observational data and found that $N_{\text{H}}^{\text{LOS}}$ and Γ are variable.
52. **NGC 7682.** We report the NuSTAR data for the first time. The model with one apec component well reproduces the X-ray spectra observed with the XMM–Newton and NuSTAR ($\chi_{\text{red}}^2 = 0.98$). We obtain $N_{\text{H}}^{\text{LOS}} = 0.25_{-0.02}^{+0.20} \times 10^{24} \text{ cm}^{-2}$ and $\Gamma = 1.27_{-0.07}^{+0.25}$ with the XClumpy model.

REFERENCES

- Ananna, T. T., Treister, E., Urry, C. M., et al. 2020, *ApJ*, 889, 17, doi: [10.3847/1538-4357/ab5aef](https://doi.org/10.3847/1538-4357/ab5aef)
- . 2019, *ApJ*, 871, 240, doi: [10.3847/1538-4357/aafb77](https://doi.org/10.3847/1538-4357/aafb77)
- Ananna, T. T., Weigel, A. K., Trakhtenbrot, B., et al. 2022, arXiv e-prints, arXiv:2201.05603. <https://arxiv.org/abs/2201.05603>
- Anders, E., & Grevesse, N. 1989, *Geochimica et Cosmochimica Acta*, 53, 197, doi: [10.1016/0016-7037\(89\)90286-X](https://doi.org/10.1016/0016-7037(89)90286-X)
- Arévalo, P., Bauer, F. E., Puccetti, S., et al. 2014, *ApJ*, 791, 81, doi: [10.1088/0004-637X/791/2/81](https://doi.org/10.1088/0004-637X/791/2/81)
- Arnaud, K. A. 1996, in *Astronomical Data Analysis Software and Systems V*, Vol. 101, 17
- Baloković, M., Comastri, A., Harrison, F. A., et al. 2014, *ApJ*, 794, 111, doi: [10.1088/0004-637X/794/2/111](https://doi.org/10.1088/0004-637X/794/2/111)
- Baloković, M., Brightman, M., Harrison, F. A., et al. 2018, *ApJ*, 854, 42, doi: [10.3847/1538-4357/aaa7eb](https://doi.org/10.3847/1538-4357/aaa7eb)
- Barthelmy, S. D., Barbier, L. M., Cummings, J. R., et al. 2005, *SSRv*, 120, 143, doi: [10.1007/s11214-005-5096-3](https://doi.org/10.1007/s11214-005-5096-3)
- Bauer, F. E., Arévalo, P., Walton, D. J., et al. 2015, *ApJ*, 812, 116, doi: [10.1088/0004-637X/812/2/116](https://doi.org/10.1088/0004-637X/812/2/116)
- Baumgartner, W. H., Tueller, J., Markwardt, C. B., et al. 2013, *The Astrophysical Journal Supplement Series*, 207, 19, doi: [10.1088/0067-0049/207/2/19](https://doi.org/10.1088/0067-0049/207/2/19)
- Bian, W., & Gu, Q. 2007, *ApJ*, 657, 159, doi: [10.1086/510708](https://doi.org/10.1086/510708)
- Boorman, P. G., Gandhi, P., Baloković, M., et al. 2018, *MNRAS*, 477, 3775, doi: [10.1093/mnras/sty861](https://doi.org/10.1093/mnras/sty861)
- Boorman, P. G., Gandhi, P., Alexander, D. M., et al. 2016, *ApJ*, 833, 245, doi: [10.3847/1538-4357/833/2/245](https://doi.org/10.3847/1538-4357/833/2/245)
- Brightman, M., & Nandra, K. 2011, *MNRAS*, 413, 1206, doi: [10.1111/j.1365-2966.2011.18207.x](https://doi.org/10.1111/j.1365-2966.2011.18207.x)
- Buchner, J., Brightman, M., Nandra, K., Nikutta, R., & Bauer, F. E. 2019, *A&A*, 629, A16, doi: [10.1051/0004-6361/201834771](https://doi.org/10.1051/0004-6361/201834771)
- Burrows, D. N., Hill, J. E., Nousek, J. A., et al. 2005, *SSRv*, 120, 165, doi: [10.1007/s11214-005-5097-2](https://doi.org/10.1007/s11214-005-5097-2)
- Eguchi, S., Ueda, Y., Terashima, Y., Mushotzky, R., & Tueller, J. 2009, *ApJ*, 696, 1657, doi: [10.1088/0004-637X/696/2/1657](https://doi.org/10.1088/0004-637X/696/2/1657)
- Fabbiano, G., Elvis, M., Paggi, A., et al. 2017, *ApJL*, 842, L4, doi: [10.3847/2041-8213/aa7551](https://doi.org/10.3847/2041-8213/aa7551)
- Fabian, A. C., Vasudevan, R. V., Mushotzky, R. F., Winter, L. M., & Reynolds, C. S. 2009, *MNRAS*, 394, L89, doi: [10.1111/j.1745-3933.2009.00617.x](https://doi.org/10.1111/j.1745-3933.2009.00617.x)
- Furui, S., Fukazawa, Y., Odaka, H., et al. 2016, *ApJ*, 818, 164, doi: [10.3847/0004-637X/818/2/164](https://doi.org/10.3847/0004-637X/818/2/164)
- Garmire, G. P., Bautz, M. W., Ford, P. G., Nousek, J. A., & Ricker, George R., J. 2003, in *Society of Photo-Optical Instrumentation Engineers (SPIE) Conference Series*, Vol. 4851, X-Ray and Gamma-Ray Telescopes and Instruments for Astronomy., ed. J. E. Truemper & H. D. Tananbaum, 28–44, doi: [10.1117/12.461599](https://doi.org/10.1117/12.461599)
- Gehrels, N., Chincarini, G., Giommi, P., et al. 2004, *ApJ*, 611, 1005, doi: [10.1086/422091](https://doi.org/10.1086/422091)
- Georgantopoulos, I., & Akylas, A. 2019, *A&A*, 621, A28, doi: [10.1051/0004-6361/201833038](https://doi.org/10.1051/0004-6361/201833038)
- Gilli, R., Comastri, A., & Hasinger, G. 2007, *A&A*, 463, 79, doi: [10.1051/0004-6361:20066334](https://doi.org/10.1051/0004-6361:20066334)
- Guainazzi, M., Fabian, A. C., Iwasawa, K., Matt, G., & Fiore, F. 2005, *MNRAS*, 356, 295, doi: [10.1111/j.1365-2966.2004.08448.x](https://doi.org/10.1111/j.1365-2966.2004.08448.x)
- Guainazzi, M., Rodriguez-Pascual, P., Fabian, A. C., Iwasawa, K., & Matt, G. 2004, *MNRAS*, 355, 297, doi: [10.1111/j.1365-2966.2004.08317.x](https://doi.org/10.1111/j.1365-2966.2004.08317.x)
- Guainazzi, M., Risaliti, G., Awaki, H., et al. 2016, *MNRAS*, 460, 1954, doi: [10.1093/mnras/stw1033](https://doi.org/10.1093/mnras/stw1033)
- Harrison, F. A., Craig, W. W., Christensen, F. E., et al. 2013, *ApJ*, 770, 103, doi: [10.1088/0004-637X/770/2/103](https://doi.org/10.1088/0004-637X/770/2/103)
- Harrison, F. A., Aird, J., Civano, F., et al. 2016, *ApJ*, 831, 185, doi: [10.3847/0004-637X/831/2/185](https://doi.org/10.3847/0004-637X/831/2/185)
- Hönig, S. F., & Beckert, T. 2007, *MNRAS*, 380, 1172, doi: [10.1111/j.1365-2966.2007.12157.x](https://doi.org/10.1111/j.1365-2966.2007.12157.x)
- Hönig, S. F., Beckert, T., Ohnaka, K., & Weigelt, G. 2006, *A&A*, 452, 459, doi: [10.1051/0004-6361:20054622](https://doi.org/10.1051/0004-6361:20054622)
- Hopkins, P. F., Hernquist, L., Cox, T. J., et al. 2006, *The Astrophysical Journal Supplement Series*, 163, 1, doi: [10.1086/499298](https://doi.org/10.1086/499298)
- Ikeda, S., Awaki, H., & Terashima, Y. 2009, *ApJ*, 692, 608, doi: [10.1088/0004-637X/692/1/608](https://doi.org/10.1088/0004-637X/692/1/608)
- Ishisaki, Y., Maeda, Y., Fujimoto, R., et al. 2007, *Publications of the Astronomical Society of Japan*, 59, 113, doi: [10.1093/pasj/59.sp1.S113](https://doi.org/10.1093/pasj/59.sp1.S113)
- Jansen, F., Lumb, D., Altieri, B., et al. 2001, *A&A*, 365, L1, doi: [10.1051/0004-6361:20000036](https://doi.org/10.1051/0004-6361:20000036)
- Kawakatu, N., Wada, K., & Ichikawa, K. 2020, *ApJ*, 889, 84, doi: [10.3847/1538-4357/ab5f60](https://doi.org/10.3847/1538-4357/ab5f60)
- Kawamuro, T., Izumi, T., & Imanishi, M. 2019, *PASJ*, 71, 68, doi: [10.1093/pasj/psz045](https://doi.org/10.1093/pasj/psz045)
- Kawamuro, T., Izumi, T., Onishi, K., et al. 2020, *ApJ*, 895, 135, doi: [10.3847/1538-4357/ab8b62](https://doi.org/10.3847/1538-4357/ab8b62)
- Kawamuro, T., Ueda, Y., Tazaki, F., Terashima, Y., & Mushotzky, R. 2016, *ApJ*, 831, 37, doi: [10.3847/0004-637X/831/1/37](https://doi.org/10.3847/0004-637X/831/1/37)
- Konami, S., Matsushita, K., Gandhi, P., & Tamagawa, T. 2012, *PASJ*, 64, 117, doi: [10.1093/pasj/64.5.117](https://doi.org/10.1093/pasj/64.5.117)
- Kormendy, J., & Ho, L. C. 2013, *Annual Review of Astronomy and Astrophysics*, 51, 511, doi: [10.1146/annurev-astro-082708-101811](https://doi.org/10.1146/annurev-astro-082708-101811)
- Koss, M., Trakhtenbrot, B., Ricci, C., et al. 2017, *ApJ*, 850, 74, doi: [10.3847/1538-4357/aa8ec9](https://doi.org/10.3847/1538-4357/aa8ec9)
- Koss, M. J., Assef, R., Baloković, M., et al. 2016, *ApJ*, 825, 85, doi: [10.3847/0004-637X/825/2/85](https://doi.org/10.3847/0004-637X/825/2/85)

- Koyama, K., Tsunemi, H., Dotani, T., et al. 2007, *Publications of the Astronomical Society of Japan*, 59, 23, doi: [10.1093/pasj/59.sp1.S23](https://doi.org/10.1093/pasj/59.sp1.S23)
- Krolik, J. H., & Begelman, M. C. 1988, *ApJ*, 329, 702, doi: [10.1086/166414](https://doi.org/10.1086/166414)
- LaMassa, S. M., Yaqoob, T., Boorman, P. G., et al. 2019, *ApJ*, 887, 173, doi: [10.3847/1538-4357/ab552c](https://doi.org/10.3847/1538-4357/ab552c)
- Laor, A., & Draine, B. T. 1993, *ApJ*, 402, 441, doi: [10.1086/172149](https://doi.org/10.1086/172149)
- Liu, Y., & Li, X. 2014, *ApJ*, 787, 52, doi: [10.1088/0004-637X/787/1/52](https://doi.org/10.1088/0004-637X/787/1/52)
- . 2015, *MNRAS*, 448, L53, doi: [10.1093/mnras/lu198](https://doi.org/10.1093/mnras/lu198)
- Madsen, K. K., Beardmore, A. P., Forster, K., et al. 2017, *AJ*, 153, 2, doi: [10.3847/1538-3881/153/1/2](https://doi.org/10.3847/1538-3881/153/1/2)
- Marchesi, S., Ajello, M., Zhao, X., et al. 2019a, *ApJ*, 882, 162, doi: [10.3847/1538-4357/ab340a](https://doi.org/10.3847/1538-4357/ab340a)
- . 2019b, *ApJ*, 872, 8, doi: [10.3847/1538-4357/aafbeb](https://doi.org/10.3847/1538-4357/aafbeb)
- Markwardt, C. B., Tueller, J., Skinner, G. K., et al. 2005, *ApJL*, 633, L77, doi: [10.1086/498569](https://doi.org/10.1086/498569)
- Merloni, A., Heinz, S., & di Matteo, T. 2003, *MNRAS*, 345, 1057, doi: [10.1046/j.1365-2966.2003.07017.x](https://doi.org/10.1046/j.1365-2966.2003.07017.x)
- Mitsuda, K., Bautz, M., Inoue, H., et al. 2007, *Publications of the Astronomical Society of Japan*, 59, S1, doi: [10.1093/pasj/59.sp1.S1](https://doi.org/10.1093/pasj/59.sp1.S1)
- Miyaji, T., Herrera-Endoqui, M., Krumpel, M., et al. 2019, *ApJL*, 884, L10, doi: [10.3847/2041-8213/ab46bc](https://doi.org/10.3847/2041-8213/ab46bc)
- Murphy, K. D., & Yaqoob, T. 2009, *MNRAS*, 397, 1549, doi: [10.1111/j.1365-2966.2009.15025.x](https://doi.org/10.1111/j.1365-2966.2009.15025.x)
- Nenkova, M., Sirocky, M. M., Ivezić, Ž., & Elitzur, M. 2008a, *ApJ*, 685, 147, doi: [10.1086/590482](https://doi.org/10.1086/590482)
- Nenkova, M., Sirocky, M. M., Nikutta, R., Ivezić, Ž., & Elitzur, M. 2008b, *ApJ*, 685, 160, doi: [10.1086/590483](https://doi.org/10.1086/590483)
- Netzer, H., Lemze, D., Kaspi, S., et al. 2005, *ApJ*, 629, 739, doi: [10.1086/431474](https://doi.org/10.1086/431474)
- Oda, S., Tanimoto, A., Ueda, Y., et al. 2017, *ApJ*, 835, 179, doi: [10.3847/1538-4357/835/2/179](https://doi.org/10.3847/1538-4357/835/2/179)
- Odaka, H., Aharonian, F., Watanabe, S., et al. 2011, *ApJ*, 740, 103, doi: [10.1088/0004-637X/740/2/103](https://doi.org/10.1088/0004-637X/740/2/103)
- Odaka, H., Yoneda, H., Takahashi, T., & Fabian, A. 2016, *MNRAS*, 462, 2366, doi: [10.1093/mnras/stw1764](https://doi.org/10.1093/mnras/stw1764)
- Ogawa, S., Ueda, Y., Tanimoto, A., & Yamada, S. 2021, *ApJ*, 906, 84, doi: [10.3847/1538-4357/abccce](https://doi.org/10.3847/1538-4357/abccce)
- Ogawa, S., Ueda, Y., Yamada, S., Tanimoto, A., & Kawaguchi, T. 2019, *ApJ*, 875, 115, doi: [10.3847/1538-4357/ab0e08](https://doi.org/10.3847/1538-4357/ab0e08)
- Oh, K., Koss, M., Markwardt, C. B., et al. 2018, *ApJS*, 235, 4, doi: [10.3847/1538-4365/aaa7fd](https://doi.org/10.3847/1538-4365/aaa7fd)
- Panessa, F., Castangia, P., Malizia, A., et al. 2020, *A&A*, 641, A162, doi: [10.1051/0004-6361/201937407](https://doi.org/10.1051/0004-6361/201937407)
- Piconcelli, E., Bianchi, S., Guainazzi, M., Fiore, F., & Chiaberge, M. 2007, *A&A*, 466, 855, doi: [10.1051/0004-6361:20066439](https://doi.org/10.1051/0004-6361:20066439)
- Piconcelli, E., Bianchi, S., Vignali, C., Jiménez-Bailón, E., & Fiore, F. 2011, *A&A*, 534, A126, doi: [10.1051/0004-6361/201117462](https://doi.org/10.1051/0004-6361/201117462)
- Puccetti, S., Comastri, A., Fiore, F., et al. 2014, *ApJ*, 793, 26, doi: [10.1088/0004-637X/793/1/26](https://doi.org/10.1088/0004-637X/793/1/26)
- Puccetti, S., Comastri, A., Bauer, F. E., et al. 2016, *A&A*, 585, A157, doi: [10.1051/0004-6361/201527189](https://doi.org/10.1051/0004-6361/201527189)
- Ricci, C., Ueda, Y., Koss, M. J., et al. 2015, *ApJ*, 815, L13, doi: [10.1088/2041-8205/815/1/L13](https://doi.org/10.1088/2041-8205/815/1/L13)
- Ricci, C., Trakhtenbrot, B., Koss, M. J., et al. 2017a, *Nature*, 549, 488, doi: [10.1038/nature23906](https://doi.org/10.1038/nature23906)
- Ricci, C., Bauer, F. E., Treister, E., et al. 2017b, *MNRAS*, 468, 1273, doi: [10.1093/mnras/stx173](https://doi.org/10.1093/mnras/stx173)
- Ricci, C., Trakhtenbrot, B., Koss, M. J., et al. 2017c, *ApJS*, 233, 17, doi: [10.3847/1538-4365/aa96ad](https://doi.org/10.3847/1538-4365/aa96ad)
- Ricci, C., Ho, L. C., Fabian, A. C., et al. 2018, *MNRAS*, 480, 1819, doi: [10.1093/mnras/sty1879](https://doi.org/10.1093/mnras/sty1879)
- Ricci, C., Privon, G. C., Pfeifle, R. W., et al. 2021, *MNRAS*, doi: [10.1093/mnras/stab2052](https://doi.org/10.1093/mnras/stab2052)
- Rivers, E., Baloković, M., Arévalo, P., et al. 2015, *ApJ*, 815, 55, doi: [10.1088/0004-637X/815/1/55](https://doi.org/10.1088/0004-637X/815/1/55)
- Strüder, L., Briel, U., Dennerl, K., et al. 2001, *A&A*, 365, L18, doi: [10.1051/0004-6361:20000066](https://doi.org/10.1051/0004-6361:20000066)
- Tanimoto, A., Ueda, Y., Kawamuro, T., & Ricci, C. 2016, *Publications of the Astronomical Society of Japan*, 68, S26, doi: [10.1093/pasj/psw008](https://doi.org/10.1093/pasj/psw008)
- Tanimoto, A., Ueda, Y., Kawamuro, T., et al. 2018, *ApJ*, 853, 146, doi: [10.3847/1538-4357/aaa47c](https://doi.org/10.3847/1538-4357/aaa47c)
- Tanimoto, A., Ueda, Y., Odaka, H., et al. 2019, *ApJ*, 877, 95, doi: [10.3847/1538-4357/ab1b20](https://doi.org/10.3847/1538-4357/ab1b20)
- . 2020, *ApJ*, 897, 2, doi: [10.3847/1538-4357/ab96bc](https://doi.org/10.3847/1538-4357/ab96bc)
- Toba, Y., Yamada, S., Ueda, Y., et al. 2020, *ApJ*, 888, 8, doi: [10.3847/1538-4357/ab5718](https://doi.org/10.3847/1538-4357/ab5718)
- Torres-Albà, N., Marchesi, S., Zhao, X., et al. 2021, *ApJ*, 922, 252, doi: [10.3847/1538-4357/ac1c73](https://doi.org/10.3847/1538-4357/ac1c73)
- Tueller, J., Mushotzky, R. F., Barthelmy, S., et al. 2008, *ApJ*, 681, 113, doi: [10.1086/588458](https://doi.org/10.1086/588458)
- Tueller, J., Baumgartner, W. H., Markwardt, C. B., et al. 2010, *The Astrophysical Journal Supplement Series*, 186, 378, doi: [10.1088/0067-0049/186/2/378](https://doi.org/10.1088/0067-0049/186/2/378)
- Tully, R. B., Rizzi, L., Shaya, E. J., et al. 2009, *AJ*, 138, 323, doi: [10.1088/0004-6256/138/2/323](https://doi.org/10.1088/0004-6256/138/2/323)
- Turner, M. J. L., Abbey, A., Arnaud, M., et al. 2001, *A&A*, 365, L27, doi: [10.1051/0004-6361:20000087](https://doi.org/10.1051/0004-6361:20000087)
- Ueda, Y., Akiyama, M., Hasinger, G., Miyaji, T., & Watson, M. G. 2014, *ApJ*, 786, 104, doi: [10.1088/0004-637X/786/2/104](https://doi.org/10.1088/0004-637X/786/2/104)
- Ueda, Y., Akiyama, M., Ohta, K., & Miyaji, T. 2003, *ApJ*, 598, 886, doi: [10.1086/378940](https://doi.org/10.1086/378940)
- Ueda, Y., Takahashi, T., Inoue, H., et al. 1998, *Nature*, 391, 866, doi: [10.1038/36047](https://doi.org/10.1038/36047)

- . 1999, *ApJ*, 518, 656, doi: [10.1086/307291](https://doi.org/10.1086/307291)
- Ueda, Y., Eguchi, S., Terashima, Y., et al. 2007, *ApJ*, 664, L79, doi: [10.1086/520576](https://doi.org/10.1086/520576)
- Uematsu, R., Ueda, Y., Tanimoto, A., et al. 2021, arXiv e-prints, arXiv:2103.11224. <https://arxiv.org/abs/2103.11224>
- van den Bosch, R. C. E. 2016, *ApJ*, 831, 134, doi: [10.3847/0004-637X/831/2/134](https://doi.org/10.3847/0004-637X/831/2/134)
- Weisskopf, M. C., Brinkman, B., Canizares, C., et al. 2002, *PASP*, 114, 1, doi: [10.1086/338108](https://doi.org/10.1086/338108)
- Willingale, R., Starling, R. L. C., Beardmore, A. P., Tanvir, N. R., & O'Brien, P. T. 2013, *MNRAS*, 431, 394, doi: [10.1093/mnras/stt175](https://doi.org/10.1093/mnras/stt175)
- Yamada, S., Ueda, Y., Tanimoto, A., et al. 2021, *ApJS*, 257, 61, doi: [10.3847/1538-4365/ac17f5](https://doi.org/10.3847/1538-4365/ac17f5)
- . 2020, *ApJ*, 897, 107, doi: [10.3847/1538-4357/ab94b1](https://doi.org/10.3847/1538-4357/ab94b1)
- Zhao, X., Marchesi, S., & Ajello, M. 2019a, *ApJ*, 871, 182, doi: [10.3847/1538-4357/aaf80b](https://doi.org/10.3847/1538-4357/aaf80b)
- Zhao, X., Marchesi, S., Ajello, M., Baloković, M., & Fischer, T. 2020, *ApJ*, 894, 71, doi: [10.3847/1538-4357/ab879d](https://doi.org/10.3847/1538-4357/ab879d)
- Zhao, X., Marchesi, S., Ajello, M., et al. 2019b, *ApJ*, 870, 60, doi: [10.3847/1538-4357/aaf1a0](https://doi.org/10.3847/1538-4357/aaf1a0)